2013

Resonance surface plasmon spectroscopy by tunable enhanced light transmission through nanostructured gratings and thin films

Wei-Hsun Yeh
Iowa State University

Resonance surface plasmon spectroscopy by tunable enhanced light transmission through nanostructured gratings and thin films

by

Wei-Hsun Yeh

A dissertation submitted to the graduate faculty in partial

fulfillment of the requirements for the degree of

DOCTOR OF PHILOSOPHY

Major: Chemical Engineering

Program of Study Committee:
Andrew C. Hillier, Major Professor
Kurt Hebert
Ian C Schneider
Emily Smith
Nastaran Hashemi

Iowa State University

Ames, Iowa

2013

TABLE OF CONTENTS

ABSTRACT

Surface plasmon resonance (SPR) is a powerful tool in probing interfacial events in that any changes of effective refractive index in the interface directly impact the behavior of surface plasmons, an electromagnetic wave, travelling along the interface. Surface plasmons (SPs) are generated only if the momemtum of incident light matches that of SPs in the interface. Observation of SPR can be achieved by either monitoring reflection via Kretchsmann configuration or enhanced transmission through nano-structured patterned substrates (for example, diffraction gratings). For Kretchsmann configuration, SPs resonate with particular frequencies of incident light and results in a decreased intensity in the reflection spectrum at corresponding wavelengths. For diffraction grating, enhanced transmission peaks at particular wavelengths is observed in that the SPs resonate with particular energies (eV) of incident light and tunnel through the nanostructure of gratings. This thesis focuses on tuning the behavior of SPs by changing the topology of diffraction gratings, monitoring the thickness of thin films by diffraction gratings, and use of dispersion images to analyze complex optical responses of SPs through diffraction gratings.

Chapter 1 covers the background/principle of SPR, comprehensive literature review, sensor applications, control of SPR spectral responses, and sensitivity of SPR. In Chapter 2, we illustrate a chirped grating with varying surface topology along its spatial position. We demonstrated that the features of nanostructure such as pitch and amplitude significantly impact the behavior of enhanced transmission. In addition, we also illustrate the sensing application of chirped grating and the results indicate that the chirped grating is a sensitive and information rich SPR platform. In chapter 3, we used a commercial DVD diffraction grating as a SPR coupler. A camera-mounted microscope with Bertrend lens attachment is used to oberserve the enhanced

transmission. We demonstrate that this system can monitor the SPR responses and track the thickness of a silicon monoxide film without using a spectrophotometer.

Surface plasmons are a result of collective oscillation of free electrons in the metal/dielectric interface. Thus, the interaction of SPs with delocalized electrons from molecular resonance is complex. In chapter 4, we perform both experimental and simulation works to address this complex interaction. Detailed examination and analysis show nontypical SPR responses. For p-polarized light, a branch of dispersion curve and quenching of SPs in the Q band of zinc phthalocyanine are observed. For both p- and s-polarized light, additional waveguided modes are observed and the wavelength from different guided modes are dispersed.

Diffraction gratings can provide complicated optical information about SPs. Both front side (air/metal) and back side (metal/substrate) provide SPR signals simultaneously. In chapter 5, we use dispersion images to analyze the complicated optical responses of SPR from an asymmetrical diffraction grating consisting of three layers (air/gold/polycarbonate). We illustrate that clear identification of SPR responses from several diffraction orders at front side and back side can be achieved by the use of dispersion images. Theoretical prediction and experimental results show consistency. We also show that only the behavior of SPs from the front side is impacted by the deposition of Langmuir-Blodgett dielectric films.

In chapter 6, we construct a diffraction grating that has a fixed pitch and several amplitudes on its surface by using interference lithography. The purpose of this work is to examine how the amplitude impacts the behavior of transmission peaks. Different amplitudes are successfully fabricated by varying development time in the lithography process. We observed that largest (optimized) enhanced transmission peak shows as the amplitude approach a critical value. Transmission is not maximized below or beyond a critical amplitude. We also found that

transmission enhancements are strongly affected by the diffraction efficiencies. A maximum enhancement is observed as diffraction efficiency is largest where amplitude reaches the critical value. The experimental results are then compared to the simulation.

First, this work demonstrates that diffraction gratings have rich information of SPs. For example, rich optical responses of SPs can be acquired by the chirped grating. For another example, the information about the behavior of SPs can be acquired by tracking first order diffraction spots. All information can be utilized to monitor the thickness of ultra thin films formed on the gratings. Therefore, diffraction gratings represent a flexible and information-rich SPR platform. Second, the transmission peaks (or optical responses of SPs) can be tuned by the topology of the diffraction gratings. The resonant wavelengths of transmission peaks can be tuned by the pitches of gratings; the magnitude of peaks can be maximized by tuning the amplitudes of gratings. The control over transmission peaks allows ones to improve the performance of grating-based SPR sensors. Last, rich yet complex optical responses of SPs from diffraction gratings can be analyzed and indexed by the use of dispersion images. Complex optical responses originate from simultaneous excitations of SPs from metal/air and metal/polymer interfaces. By the use of dispersion images, enhanced transmission from the front side interface (metal/air) and reduced transmission from the back side interface (metal/polycarbonate) can be identified and different modes of SPs can be indexed.

CHAPTER 1. INTRODUCTION

The first published article reporting the observation of surface plasmon resonance was by R.W. Wood[1]. He observed a narrow dark band in the diffraction dispersion image when a metal grating was lit by polychromatic light. He reported this phenomenon as Wood's anomaly but failed to explain and recognize the existence and excitation of surface plasmons (SPs). In 1957, Ritchie[3] first proposed the existence of SPs and explained Wood's anomaly as an optical phenomenon termed surface plasmon resonance in his pioneering work. In the following decade, devices using attenuated total refection to optically excite SPs were developed by Otto[4] and Kretschmann[5]. Until 1983, the application of SPR was demonstrated by developing an optical gas sensor to detect the concentration of O_2 and CO_2[6]. Since then, the importance of this optical phenomenon was widely studied and applied to various field in recent years[2, 7-10].

1.1 Applications of SPR sensors

The applications exploiting SPR are diverse. In biosensing applications, SPR does not require a label and can detect direct binding events of biospecific molecules on a sensing surface. For example, carbohydrates (glycans) and their conjugates are important in many biological processes. The carbohydrate-recognized bindings in environments similar to living organisms with detection limits down to ~ nM has been reported[11]. Lectin-based immunoarrays have gained successful progress in diagnosing human chorionic gonadotropin glycosylation patterns[12]. Label free SPR sensors and immnoassays have been widely adopted to rapidly detect the presence of bacteria[13]. The immobilization methods for bacteria detection used in SPR sensing are mainly physical adsorption and covalent binding with different assay types[13]. Other examples include

protein detection[14-16], detection of DNA by peptide nucleic acids[17], hybridization of complementary strands of DNA and its kinetics[18].

Surface plasmon resonance is very sensitive to any refractive index change in the metal/dielectric interface, and this optical phenomenon has been used to detect the presence of ultra thin layer or change in thickness of layers. A recent work has demonstrated that the length of different alkane-thiolate on the gold coated grating can be distinguished by SPR[16]. SPR monitoring the degree of swelling of polymers in different solvents have been demonstrated[20]. Both the thickness of organic monolayer and its nanosctructed pattern have been measured and imaged[21].

SPR-based chemical sensors are widely used to detect different gas in environments. Chloro-fluoro-carbon (CFC) vapors deplete Ozone in the atmosphere. A gas sensor with a thin layer of polyfluorosiloxane, which specifically recognize CFC, was constructed to monitor the concentration of CFC[22]. In addition, detection of other gases such as NO_2[23], O_2[6, 24, 25],CO_2[6, 25], and H_2[26] has also been reported.

In the food industry, Mycotoxin, a toxin produced by fungi, can contaminate the food chain and threaten human health. Detecting the presence of Mycotoxin is crucial for food safety. SPR-based sensors have been developed for determining Mycotoxin[27]. For example, Aflatoxins can be found in cereal, peanut, and milk, and it can be 100 times more toxic than KCN. The detection limit for Aflatoxins has reached 0.2 ng/g by SPR sensors using cocktail of anti-mycotoxin antibodies[28].

In clinical diagnosis application, plasmonic optical-based sensors have been developed and reported. A low-cost, label-free, and sensitive screening of the microalbuminuria SPR sensor with dynamic range of 1 ng/ml to 1 micro-g/ml without sample purification has been

developed[29]. Fetal fibronectin is a biomarker to assess the risk of preterm birth, and early detection of fetal fibronectin can reduce perinatal morbidity and mortality. Chen et al.[30] have developed a SPR biosensor to quantitatively measure fetal fibronectin concentrations. In addition, a SPR-based biomarker sensor has been demonstrated to detect Alzheimer's disease[31].

Other important applications of SPR sensors are summarized in the following tables. The residue measurement of pesticide is crucial to the digestive human health. According to the regulation of the U.S. Environmental Protection Agency (EPA), atrazine and simazine concentration must be below 3 ng/ml and 4 ng/ml, respectively. Table1 shows the application of SPR to detect the concentration of pesticide residues. The detection of explosives is important to public transportation for the safety of air transportation. A reliable yet rapid detection of explosives is necessary (Table 2). A rapid and accurate pollutant monitoring ensures the minimal impact to environment and is shown in Table 3. Virus detection is critical to public hygiene and a preventive control of virus spread. Table 4 shows virus detection via SPR sensors. Detection of the existence and concentration of bacteria is important for public hygiene and food consumption (Table 5).

Table 1 Application in Pesticide Detection[103]

Pesticide	Assay format	Detection limit	Instrument	Recognition element
Atrazine[32]	Inhibition immunoassay	0.05 ng/ml	Biacore	Monoclonal antibodies
Atrazine[33]	Competition immunoassay using Atrazine-HRP-conjugate	5 ng/ml	Biacore 2000	Polyclonal antibodies
Simazine[34]	Inhibition immunoassay	1 ng/ml	Biacore 2000	Polyclonal antibodies

Table 2 Explosive Detection[103]

Explosive	Assay format	Detection limit	Instrument
TNT[32]	Indirect competition immunoassay by physical adsorption of TNP-ovalbumin-conjugate	0.09–1,000 ng/ml	SPR-760 (Nippon Laser and Electronics, Japan)
TNT[32]	Competition immunoassay using Atrazine- HRP-conjugate	0.09–1,000 ng/ml	SPR-760 (Nippon Laser and Electronics, Japan)
TNT[32]	Inhibition immunoassay	1μg/ml	Spreeta (Texas Instruments, USA) SPR-760 (Nippon Laser and Electronics, Japan)

Table 3 Pollutant monitoring[103]

Pollutant	Assay format	Detection limit	Instrument	Recognition element
2,3,7,8-TetraChloro Dibenzo-p-Dioxin[34]	Competition immunoassay using 2,3,7,8-TCDD- HRP-conjugate	0.1 ng/ml	Biacore 2000	Monoclonal antibodies
4-Nonylphenol[37]	Inhibition immunoassay in buffer	2 ng/ml	Biacore Q	Monoclonal antibodies
Phenol, hydroquinone, resorcinol, phloroglucinol, and catechol[38]	Direct detection in buffer	100 μg/ml	Intensity modulation SPR	Immobilized synthetic receptors in polymer and sol-gels
Phenol[39]	Direct detection in buffer	5μg /ml	Multiscope SPR (Optrel,Germany)	Immobilizing E. coli via synthetic cystein terminated oligopeptides
Bisphenol A (BPA) [40]	Inhibition immunoassay in buffer by immobilizing the BPA on the sensor surface followed with monoclonal	10 ppb	SPR-20 (DKK,Japan)	Monoclonal antibodies

Table 3 continued

3, 30, 4, 40,5-penta-chlorobiphenyl (PCB)[34]	Competition immunoassay in buffer using PCB- HRP-conjugate	2.5 ng/ml	Biacore 2000	Polyclonal antibody
2-Hydroxy-biphenyl (HBP)[41]	Inhibition immunoassay using HBP-BSA-conjugate and anti-HBP	0.1 ng/ml	Miniaturized SPR biosensor, 1-1, Nakashima 2-chome, Kokurakita-ku, Kitakyushu, Fukuoka, Japan (TOTO Ltd., Japan)	Monoclonal antibody
Cadmium, zinc, and nickel[42]	Direct detection	0.1 μg/ml	Biacore SPR	Immobilized metallothinein cellular proteins on dextran
Copper ions (CuCC)	Direct detection	0.063 pg/ml	Attenuated total reflection and angular SPR modulation	Entrapped squarylium dye in a thin polymer layer

Table 4 Virus Detection[103]

Virus	Assay	Dtection limit	Instrument
Epstein-Barr virus[43]	Direct immunoassay in buffer and in 1% human serum	0.2 ng/ml (1 pM)	Custom-made wavelength division multiplexing
Avian leucosis virus (ALV)[36]	Direct immunoassay in buffer	9.2 nM for direct assay, 4.39 nM for sandwich assay, 0.62 nM for PAP method	Wavelength-modulated waveguide SPR
Human immun-odeficiency virus type 1 (HIV-1)[36]	Using specific hybridization of immobilized biotinylated HIV-1 oligonucleotide probe on the sensor surface to single-stranded DNA amplified by polymerase chain reaction	Proof existence. DL: N/A	Biacore 1000

Table 5 Bacteria detection[103]

Bacteria	Matrix	Assay	Instrument	Detection limit
Escherichiacoli O157:H7 l[44]	In buffer	Sandwich immunoassay	Biacore	5-7×10^7 cfu/ml
Escherichiacoli O157:H7[44]	In buffer	Inhibition immunoassay	Biacore	0.1-1×10^7cfu/ml
Escherichiacoli O157:H7[45]	In buffer	Inhibition immunoassay	Spreeta, Texas Instruments, Sensata Technologies, Attleboro, MA	8.7×10^6 cfu/ml
Salmonella typhimurium[46]	In buffer	Direct immunoassay	MultiscopeSPR (Optrel, Germany)	10^2–10^9 cfu/ml
Salmonella paratyphi[40]	In buffer	Direct immunoassay	MultiscopeSPR (Optrel, Germany)	10^2–10^7 cfu/ml

1.2 Reviews of SPR

Since SPR sensors are low-cost, sensitive, label free, selective to analytes/adsorbates, and offering real time monitoring, over five hundred papers had been published in a single year in 2006, and the number of papers, plasmonic-specific textbooks[47-57], and topics related to SPR still increase. The topics of reviews and publications are diverse and they include the principles of SPR[8, 49, 56, 57], the design of SPR instruments[48, 58], biosensor applications[2, 59-61], optical phenomena originated from SPs[7, 62], chemical sensors[47, 50], and food science[62, 63], different plasmonic responses by modifying nanopatterns in SPR sensors[64], and medical diagnosis[65].

1.3 SPR and Other Spectroscopies

The plasmonic optical phenomenon of SPR can be combined with other spectroscopy methods to either improve the performance or extend the flexibility in applications. The sensitivity of surface-enhanced Raman scattering (SERS) can be optimized combined with SPR[66]. Surface-enhanced infrared absorption (SEIRA) spectroscopy is combined with SPR and used to detect specific fingerprints of biological analytes[67]. The combination of surface plasmon-enhanced fluorescence spectroscopy (SPFS) to surface plasmon resonance can increase the sensitivity to several orders of magnitude[68]. A modified dark-field microscope by combining Rayleigh scattering spectroscopy with surface-enhanced resonance Raman scattering (SERRS) spectroscopy has been reported to optimize excitation conditions and clarify the mechanisms of SERRS[69]. Electrochemical SPR (ESPR) was developed to study the switch of tethered nucleic acid (PNA) conformation[70]. SPR together with acoustic wave methods was used to obtain information on density and viscosity of matters[71].

1.4 Principles of SPR

The collective oscillation of electrons is surface plasmons (SPs)[3-5, 72], and the conceptual scheme is shown in Figure 1. SPs are induced by the photons of incident light at specific matching conditions. However, not all wavelengths of incident light satisfy this matching condition. At matching conditions, the momentum of incident photons must match the momentum of SPs, and the momentum matching results in resonance between SPs and incident photons[16]. Thus, the energy carried by photons transfers to SPs which oscillate near the metal/dielectric interface. This resonance phenomenon is termed surface plasmon resonance.

The physics and mathematical expressions describing SPR derive from Maxwell's equations. SP is an electromagnetic wave that propagates along the interface between metal and dielectric medium[2, 7, 8]. The propagating nature of SPs is a direct result of solving Maxwell's equation with defined boundary conditions[72]. The electromagnetic fields describe SPs travelling along the x direction in the metal/dielectric interface are shown in Figure 1 and described by

$$
\begin{aligned}
&z > 0 \\
&\mathbf{E}_2 = E_{x2}\left[\exp i\left(k_{x2}x + k_{z2}z - wt\right)\right]\mathbf{i} + E_{z2}\left[\exp i\left(k_{x2}x + k_{z2}z - wt\right)\right]\mathbf{k} \\
&\mathbf{B}_2 = B_{y2}\left[\exp i\left(k_{x2}x + k_{z2}z - wt\right)\right]\mathbf{j} \\
&z < 0 \\
&\mathbf{E}_1 = E_{x1}\left[\exp i\left(k_{x1}x - k_{z1}z - wt\right)\right]\mathbf{i} + E_{z1}\left[\exp i\left(k_{x1}x - k_{z1}z - wt\right)\right]\mathbf{k} \\
&\mathbf{B}_1 = B_{y1}\left[\exp i\left(k_{x1}x - k_{z1}z - wt\right)\right]\mathbf{j}
\end{aligned}
\qquad \text{(A)}
$$

, where the bold face means vector, **E** is electric field, E is the magnitude of electric field, **B** is magnetic field, B is the magnitude of magnetic field, k is component of wavevector, and ω is angular frequency. The SPs are continuous in the interface and must obey Maxwell's equation:

$$\nabla \times \mathbf{B}_i = \frac{\varepsilon_i}{c}\frac{\partial}{\partial t}\mathbf{E}_i \qquad \text{(B)}$$

$$\nabla \times \mathbf{E}_i = -\frac{1}{c}\frac{\partial}{\partial t}\mathbf{B}_i \qquad \text{(C)}$$

Boundary Conditions:

$$E_{x1} = E_{x2}$$

$$B_{y1} = B_{y2}$$

$$k_{x1} = k_{x2}$$

Substitute Eq. set (A) into Eq. (B), and the results have equation sets of component **i** and **k**:

$$
\begin{aligned}
&\left(B_{y1}k_{z1} + \frac{\varepsilon_1\omega}{c}E_{x1}\right)\mathbf{i} + \left(B_{y1}k_{x1} + \frac{\varepsilon_1\omega}{c}E_{z1}\right)\mathbf{k} = 0 \\
&\left(-B_{y2}k_{z2} + \frac{\varepsilon_2\omega}{c}E_{x2}\right)\mathbf{i} + \left(B_{y2}k_{x2} + \frac{\varepsilon_2\omega}{c}E_{z2}\right)\mathbf{k} = 0
\end{aligned}
\qquad \text{(D)}
$$

Substitute Eq. set (A) into Eq. (C) and the arranged Eq. set is

$$\begin{aligned} E_{x1}k_{z1} + E_{z1}k_{x1} &= -\frac{\omega}{c}B_{y1} \\ E_{x2}k_{z2} - E_{z2}k_{x2} &= \frac{\omega}{c}B_{y2} \end{aligned} \qquad \text{(E)}$$

From **i** component of Eq. set (D) and boundary conditions, the result has the form

$$\frac{k_{z1}}{\varepsilon_1} + \frac{k_{z2}}{\varepsilon_2} = 0 \qquad \text{(F)}$$

For each medium, use corresponding equations from Eq. set (D) and (E), and the final result has a form representing both media

$$k_x^2 + k_{zi}^2 = \left(\frac{\omega}{c}\right)^2 \varepsilon_i \qquad \text{(G)}$$

Solving Eq. (F) and (G) yields the dispersion relation

$$k_x = \frac{\omega}{c}\sqrt{\frac{\varepsilon_1\varepsilon_2}{\varepsilon_1 + \varepsilon_2}} \qquad \text{(H)}$$

For the metal/air interface, the dispersion relation describes the SPs evanesce along the interface with limited propagation length and the momentum of SPs is expressed by equation (H). Additional information from Eq. (G) depicts that the z-direction vector field decays into metal and dielectric medium with limited penetration depth.

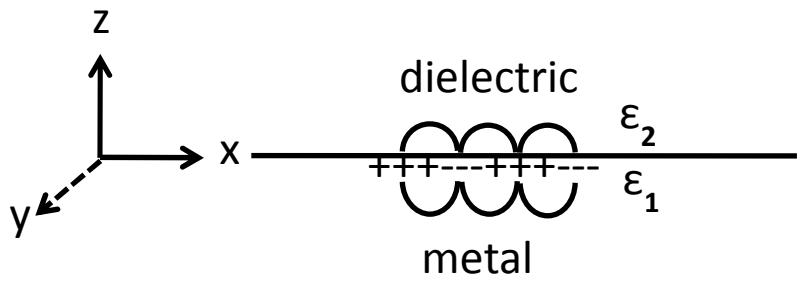

Figure 1 Illustration of SPs in the metal/dielectric interface.

1.5 The platforms to excite SPR

Several configurations or couplers can induce SPR. Figure 2 illustrates configurations which can support SPs. In Kretschmann configuration[5] (Figure 2A), a thin metal film is deposited on a prism surface. Incident light with incident angle that is larger than critical angle is illuminated on the metal film. Since the incident angle is greater than critical angle, total internal reflection occurs (TIR) in the interface. TIR in the interface supports SPs and the light in the

interface and the SPs are evanescently tunneling through the metal/dielectric boundary. As a result, part of the reflection intensity is attenuated into SPs, and this "hybrid" term is called attenuated total internal reflection (ATR). In Otto configuration[4], shown in Figure 2B, a vey thin layer of air gap is between the prism and a metal surface, and the photons tunnel through the air gap between the prism and the metal surface.

Momentum matching conditions can be achieved by diffraction gratings and be shown in Figure 2C and 2D. Incident light is directed toward the metal surface of the gratings, and the pitches of the gratings are comparable to the wavelength of incident light. When the vector component of diffracted light whose wavevector matches the SP's wavevector, SPR occurs. Both dielectric/metal interface and substrate/metal interface can support SPs if SPs can penetrate the metal layer. The grating-based SPR couplers have major advantages since the couplers can be mass-produced by injection molding, hot embossing, and lithography. Thus, grating-based SPR couplers open the door for low cost yet high-throughput platforms for SPR sensing.

The principle to induce SPR using a waveguide (Figure 2E) is similar to the mechanism in the Kretschmann configuration. The light is guided by either a single or multi-layer (slab or channel) waveguide via ATR to a region with a thin metal-coated layer. Optical waveguide SPR sensors have attractive features, such as the simple control of the optical path in the sensor system, small sizes, and ruggedness.

Last, metal nanoparticles (NPs) can serve as a platform to excite SPR by scattered light, which is termed localized surface plasmon resonance (LSPR)[73]. In principle, the conducting surface of NP interacts with incident light. This interaction induces SP along the surface of NP, and therefore SP is "localized" on the surface of each NP. From the basis of LSPR, a technique called nanolithography uses NPs as masks on a substrate and creates different nanopatterns[74].

The disadvantages of this technique include low reproducibility, and high cost. Other types of couples include single nano-aperture[75], periodic sub-wavelength nano-holes[76], and nanoslit array[77] on substrates.

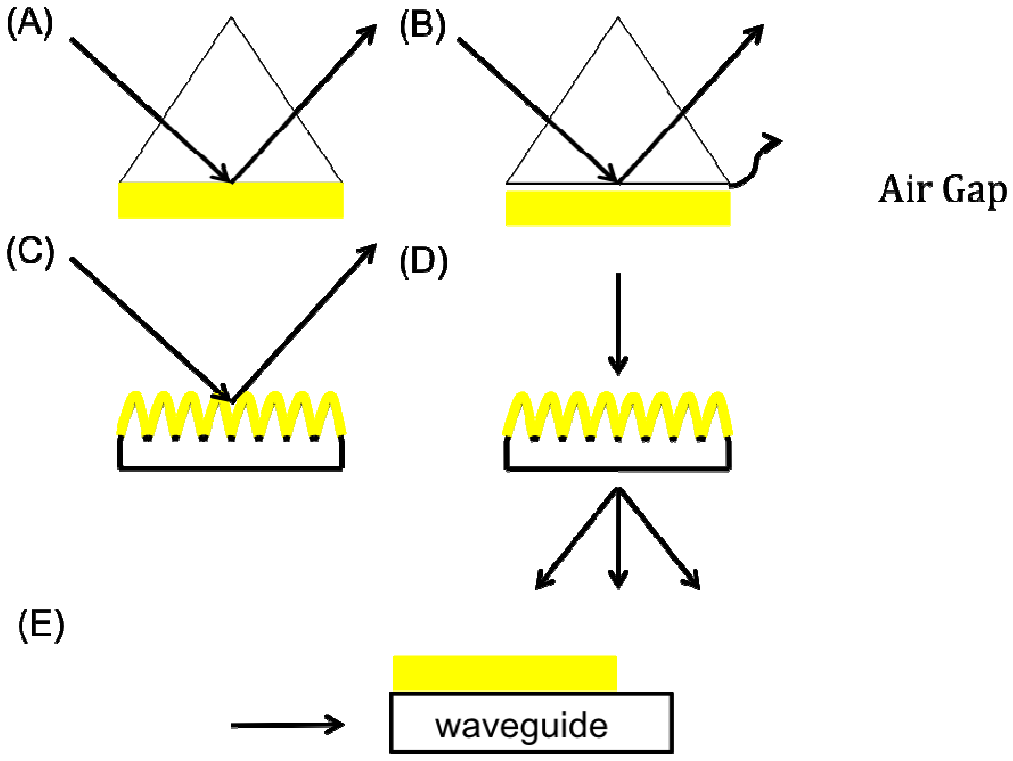

Figure 2 Illustration of SPR Configuration. (A) Kretschmann configuration, (B) Otto configuration, (C) reflection from gratings, (D) transmission from gratings, (E) and waveguied SPR.

1.6 The Tracking Parameters of SPR

Several parameters can be used to track the behavior of SPs propagating along the metal/dielectric interface. These properties include amplitude, spectral response, phase, and polarization. For clarity, we only discuss the responses of reflected light via Kretschmann configuration. For angular modulation, a light beam with single wavelength illuminates the sample; the strongest matching condition is found by varying the incident light angle (Figure 3A, upper). Conversely, in wavelength modulation method, the sample is positioned at a fixed incident angle, and the strongest coupling wavelength is found in reflection spectra as shown in Figure 3B. At fixed wavelength and incident angle, change in intensity is used to determine reflection changes in interface (Figure 3B). Additional analyte or layer in the interface causes a phase shift in reflected light. Thus, at fixed incident angle and wavelength, the strongest matching condition can be determined as illustrated in Figure 3A. For polarization modulation, the principle is similar to ellipsometer spectroscopy, strongest coupling condition is determined by finding reflection minimum by a polarizer.

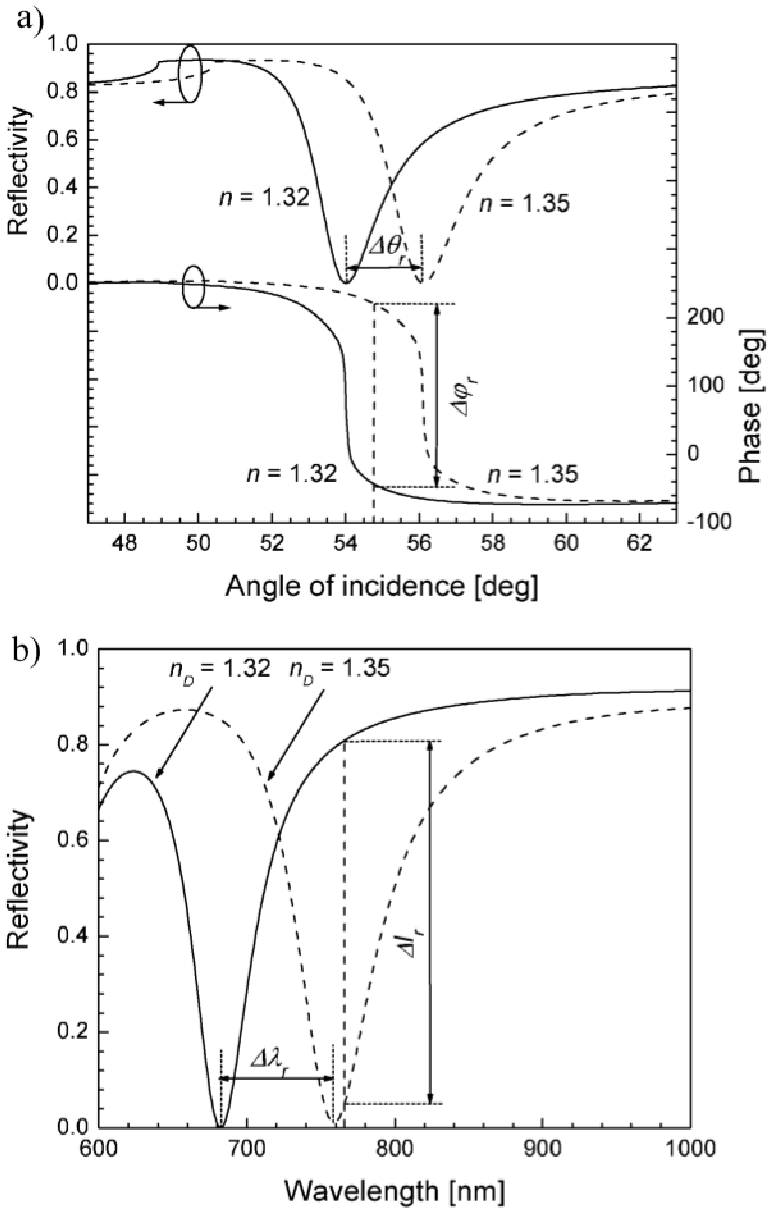

Figure 3 Reflectivity and phase for light wave exciting an SPW in the Kretschmann geometry (SF14 glass prism – 50 nm thick gold layer – dielectric) versus (a) the angle of incidence for two different refractive indices of the dielectric (wavelength 682 nm), and (b) wavelength for two different refractive indices of the dielectric (angle of incidence 54°)[2]

1.7 Sensitivity Evaluation

The sensitivity of SPR sensors is defined as follows: $\frac{\delta y}{\delta x}$

where y is the parameter to be monitored such as intensity, wavelength shift, and resonant angle from reflection or transmission peak wavelength. x can be effective refraction index, thickness of adsorbates, or time. For example, nm RIU^{-1} refers to the derivative of the change in wavelength (red shift) to refractive index unit (RIU). The sensitivity can be analytically determined by solving Fresnel equations for prism type couplers. Rigorous coupled-wave theory (RCWA) determines the sensitivity of diffraction gratings. Table 6 shows the summary of calculation of sensitivity of different SPR couplers[2]. The parameters used in the theoretical calculation are:

1. Prism is BK7.
2. The thickness of gold is 50 nm.
3. The refraction index of adsorbate is 1.32.
4. The pitch and depth of gratings are 800 nm and 70 nm, respectively.

The sensitivity of prism type SPR sensors by experiments has been studied[78]and reviewed[2]. The sensitivity of different parameters is studied and can be classified as following:

1. Monitoring the reflection angles[79, 80]
2. Tracking intensity of reflection light[81, 82]
3. Measuring of wavelength of reflected light[83].

For example, a commercial instrument BIAcore, based on prism type, has the refractive index resolution to 3×10^{-7}(1/RIU) via angular interrogation[84]. For grating-based SPR sensors, the sensitivity is also studied by experiments. The change in intensity has been verified[85, 86] and reviewed[2]. For silver-coated gratings, the sensitivity of wavelength reaches 1000 nm RIU^{-1}[87], and

the sensitivity of angular variation is ~ 100 degree RIU^{-1}[187]. For gold-coated gratings, experiments have been done in aqueous medium[85, 86]. The sensitivity of angular variation is 30 degree RIU^{-1}, and the sensitivity of intensity is 9 fold RIU^{-1}.[85, 86]

Table 6 Sensitivity Summary[2]

Parameter monitored	Angular	Wavelength	Intensity
Unit of Sensitivity	Degree/RIU	nm/RIU	% of light/RIU
Wavelength of incident light	630 nm	630 nm	630 nm
Prism type SPR couplers	191	970	3900
Diffraction grating coupler	43	309	1100

1.8 References

1. Wood, R. W., On a remarkable case of uneven distribution of light in a diffraction grating spectrum. *Phil. Magm.* **(1902),** *4*, 396–402.

2. Homola, J., Present and future of surface plasmon resonance biosensors. *Analytical and Bioanalytical Chemistry* **2003,** *377* (3), 528-539.

3. Ritchie, R. H., Plasma Losses by Fast Electrons in Thin Films. *Physical Review* **1957,** *106* (5), 874.

4. Otto, A., Excitation of surface plasma waves in silver by the method of frustrated total reflection. *Z. Physik* **1968,** *216*, 398-410.

5. Kretschmann, E., Raether, H., Radiative decay of non-radiative surface plasmons excited by light. *Z. Naturforsch* **1968,** *23A*, 2135 – 2136.

6. C. Nylander, B. L., T. Lind, Gas detection by means of surface plasmons resonance. *Sensors and Actuators* **1982,** *3*, 79-88.

7. Barnes, W. L.; Dereux, A.; Ebbesen, T. W., Surface plasmon subwavelength optics. *Nature* **2003,** *424* (6950), 824-830.

8. Homola, J.; Yee, S. S.; Gauglitz, G., Surface plasmon resonance sensors: review. *Sensors and Actuators B: Chemical* **1999,** *54* (1–2), 3-15.

9. Silin, V.; Plant, A., Biotechnological applications of surface plasmon resonance. *Trends in Biotechnology* **1997,** *15* (9), 353-359.

10. Haes, A. J.; Van Duyne, R. P., A unified view of propagating and localized surface plasmon resonance biosensors. *Analytical and Bioanalytical Chemistry* **2004,** *379* (7), 920-930.

11. K. Foley, E. F., L. Joshi, N. Tao, *Analyst* **2008,** *133*, 744-746.

12. L.S. Kelly, S. B., D. Puett, Molec., *Cell. Endocrinol.* **2007,** *260–262*, 33-39.

13. Dudak, F. C.; Boyacı, İ. H., Rapid and label-free bacteria detection by surface plasmon resonance (SPR) biosensors. *Biotechnology Journal* **2009,** *4* (7), 1003-1011.

14. Singh, B. K.; Hillier, A. C., Surface plasmon resonance imaging of biomolecular interactions on a grating-based sensor array. *Analytical Chemistry* **2006,** *78* (6), 2009-2018.

15. Singh, B. K.; Hillier, A. C., Multicolor surface plasmon resonance imaging of ink jet-printed protein microarrays. *Analytical Chemistry* **2007,** *79* (14), 5124-5132.

16. Singh, B. K.; Hillier, A. C., Surface plasmon resonance enhanced transmission of light through gold-coated diffraction gratings. *Analytical Chemistry* **2008,** *80* (10), 3803-3810.

17. Zanoli, L.; D'Agata, R.; Spoto, G., Surface plasmon-based optical detection of DNA by peptide nucleic acids. *Minerva Biotechnol.* **2008,** *20* (4), 165-174.

18. Peterson, A. W.; Heaton, R. J.; Georgiadis, R. M., The effect of surface probe density on DNA hybridization. *Nucleic Acids Res.* **2001,** *29* (24), 5163-5168.

19. Cooper, M., Label-free screening of bio-molecular interactions. *Analytical and Bioanalytical Chemistry* **2003,** *377* (5), 834-842.

20. Meier, F.; Schiewe, B.; Esker, A.; Wegner, G., Sorption and swelling in ultra-thin polymer films. *Macromol. Symp.* **1999,** *145*, 161-168.

21. Steiner, G.; Sablinskas, V.; Hubner, A.; Kuhne, C.; Salzer, R., Surface plasmon resonance imaging of microstructured monolayers. *J. Mol. Struct.* **1999,** *509* (1-3), 265-273.

22. Abdelghani, A.; Veillas, C.; Chovelon, J. M.; Jaffrezic-Renault, N.; Gagnaire, H., Stabilization of a surface plasmon resonance (SPR) optical fibre sensor with an ultra-thin organic film: application to the detection of chloro-fluoro-carbon (CFC). *Synthetic Metals* **1997,** *90* (3), 193-198.

23. El-Basaty, A. S.; El-Brolossy, T. A.; Abdalla, S.; Negm, S.; Abdella, R. A.; Talaat, H., Surface plasmon sensor for NO2 gas. *Surface and Interface Analysis* **2008,** *40* (13), 1623-1626.

24. Liedberg, B.; Nylander, C.; Lundstrom, I., Surface-plasmon resonance for gas-detection and biosensing. *Sensors and Actuators* **1983,** *4* (2), 299-304.

25. D.W. Lubbers, N. O., Eine neue pCO2-bzw: pO2-Messonde zur Messung des pCO2 oder pO2 von Gasen und Flu □ssigkeiten. *Zeitschrift Fu □r Naturforschung C* **1983,** *30* (1975), 532-533.

26. Bevenot, X.; Trouillet, A.; Veillas, C.; Gagnaire, H.; Clement, M., Surface plasmon resonance hydrogen sensor using an optical fibre. *Meas. Sci. Technol.* **2002,** *13* (1), 118-124.

27. Li, Y.; Liu, X.; Lin, Z., Recent developments and applications of surface plasmon resonance biosensors for the detection of mycotoxins in foodstuffs. *Food Chemistry 132* (3), 1549-1554.

28. Van der Gaag, B., Spath, S., Dietrich, H., Stigter, E., Boonzaaijer, G., Van Osenbruggen, T., & Koopal, K., Biosensors and multiple mycotoxin analysis. . *Food Control* **2003,** *14*, 251-254.

29. Lai, T.; Hou, Q. N.; Yang, H. A.; Luo, X. G.; Xi, M. R., Clinical application of a novel sliver nanoparticles biosensor based on localized surface plasmon resonance for detecting the microalbuminuria. *Acta Biochim. Biophys. Sin. 42* (11), 787-792.

30. Chen, C. Y.; Chang, C. C.; Yu, C.; Lin, C. W., Clinical Application of Surface Plasmon Resonance-Based Biosensors for Fetal Fibronectin Detection. *Sensors 12* (4), 3879-3890.

31. Haes, A. J.; Chang, L.; Klein, W. L.; Van Duyne, R. P., Detection of a Biomarker for Alzheimer's Disease from Synthetic and Clinical Samples Using a Nanoscale Optical Biosensor. *Journal of the American Chemical Society* **2005,** *127* (7), 2264-2271.

32. Minunni, M.; Mascini, M., Detection of Pesticide in Drinking Water Using Real-Time Biospecific Interaction Analysis (BIA). *Analytical Letters* **1993,** *26* (7), 1441-1460.

33. Lim, T.-k.; Oyama, M.; Ikebukuro, K.; Karube, I., Detection of Atrazine Based on the SPR Determination of P450 mRNA Levels in Saccharomyces cerevisiae. *Analytical Chemistry* **2000,** *72* (13), 2856-2860.

34. Shimomura, M.; Nomura, Y.; Zhang, W.; Sakino, M.; Lee, K.-H.; Ikebukuro, K.; Karube, I., Simple and rapid detection method using surface plasmon resonance for dioxins, polychlorinated biphenylx and atrazine. *Analytica Chimica Acta* **2001,** *434* (2), 223-230.

35. Shankaran, D. R.; Gobi, K. V.; Matsumoto, K.; Imato, T.; Toko, K.; Miura, N., Highly sensitive surface plasmon resonance immunosensor for parts-per-trillion level detection of 2,4,6-trinitrophenol. *Sensors and Actuators B: Chemical* **2004,** *100* (3), 450-454.

36. Strong, A., D. I. Stimpson, D. U. Bartholomew, T. F. Jenkins, & J. L. Elkind., Detection of trinitrotoluene (TNT) extracted from soil using a surface plasmon resonance (SPR)-based

sensor platform. . *Proc. SPIE* **1999,** *3710*, 362-372.

37. Samsonova, J. V.; Uskova, N. A.; Andresyuk, A. N.; Franek, M.; Elliott, C. T., Biacore biosensor immunoassay for 4-nonylphenols: assay optimization and applicability for shellfish analysis. *Chemosphere* **2004,** *57* (8), 975-985.

38. Wright, J. D.; Oliver, J. V.; Nolte, R. J. M.; Holder, S. J.; Sommerdijk, N. A. J. M.; Nikitin, P. I., The detection of phenols in water using a surface plasmon resonance system with specific receptors. *Sensors and Actuators B: Chemical* **1998,** *51* (1,Äì3), 305-310.

39. Choi, J.-W.; Park, K.-W.; Lee, D.-B.; Lee, W.; Lee, W. H., Cell immobilization using self-assembled synthetic oligopeptide and its application to biological toxicity detection using surface plasmon resonance. *Biosensors and Bioelectronics* **2005,** *20* (11), 2300-2305.

40. Soh, N., Indirect competitive immunoassay for Bisphe-

nol A, based on a surface plasmon resonance sensor. *Sens. Mater* **2003,** *15*, 423-438.

41. Kim, S. J.; Gobi, K. V.; Harada, R.; Shankaran, D. R.; Miura, N., Miniaturized portable surface plasmon resonance immunosensor applicable for on-site detection of low-molecular-weight analytes. *Sensors and Actuators B: Chemical* **2006,** *115* (1), 349-356.

42. Wu, C., Immobilization of metallothionein as a sensitive biosensor chip for the detection of metal ions by surface plasmon resonance. *Biosens. Bioelectron* **2004,** *20*, 864-871.

43. Vaisocherov, H.; Mrkvov, K. ô. Piliarik, M.; Jinoch, Pteinbachov, M.; Homola, J. ô., Surface plasmon resonance biosensor for direct detection of antibody against Epstein-Barr virus. *Biosensors and Bioelectronics* **2007,** *22* (6), 1020-1026.

44. Fratamico, P. M.; Strobaugh, T. P.; Medina, M. B.; Gehring, A. G., Detection of Escherichia coli 0157:H7 using a surface plasmon resonance biosensor. *Biotechnology Techniques* **1998,** *12* (7), 571-576.

45. Meeusen, C. A., E. C., Detection of E. coli O157: H7 using a miniaturized surface plasmon resonance biosensor. *Trans. Amer. Soc. Agr. Eng.* **2005,** *6*, 2409–2416.

46. Oh, B., Immunosensor for detection of Legionella pneumophila using surface plasmon resonance. *Biosens. Bioelectron* **2003.,** *18*, 605-611.

47. F, B., *Optical chemical sensors.* Springer, New York: 2006; Vol. 224.

48. Fischer, N. J. d. M. a. M. J. E., *Surface Plasmon Resonance: Methods and Protocols (Methods in Molecular Biology)*.

49. Frazier, R. A., *Handbook of Surface Plasmon Resonance*. Royal Society of Chemistry: 2008.

50. G, O., *Frontiers in chemical sensors: novel principles and techniques.* Springer, New York: 2005.

51. Hass, G., *Physics of thin films*. New York: Academic.: 1977; Vol. 9.

52. J, H., *Surface plasmon resonance based sensors*. Springer, Berlin: 2006.

53. L, G., *Biosensors and modern biospecific analytical techniques*. 1 ed.; Elsevier, Amsterdam: 2005.

54. L, Z., *Controlled growth of nanomaterials.* World Scientific, Singapore: 2007.

55. Mol, N. J. d., *Surface Plasmon Resonance: Methods and Protocols (Methods in Molecular Biology)*. Humana Press: 2010.

56. Raether, H., *Surface plasmons on smooth and rough surfaces and on gratings.* Berlin: Springer.: 1988.

57. Sarid, D., *Modern Introduction to Surface Plasmons: Theory, Mathematica Modeling, and Applications*. 1 ed.; Cambridge University Press: 2010.

58. Panigrahi, S.; Das, N. B.; Hassan, A. K.; Ray, A. K., Optical surface plasmon resonance sensor designs. In *Advanced Photonic Sensors and Applications*, Lieberman, R. A.; Asundi, A. K.; Asanuma, H., Eds. Spie-Int Soc Optical Engineering: Bellingham, 1999; Vol. 3897, pp 534-542.

59. Abdulhalim, I.; Zourob, M.; Lakhtakia, A., Surface Plasmon Resonance for Biosensing: A Mini-Review. *Electromagnetics* **2008,** *28* (3), 214-242.

60. Anker, J. N.; Hall, W. P.; Lyandres, O.; Shah, N. C.; Zhao, J.; Van Duyne, R. P., Biosensing with plasmonic nanosensors. *Nat Mater* **2008,** *7* (6), 442-453.

61. Phillips, K.; Cheng, Q., Recent advances in surface plasmon resonance based techniques for bioanalysis. *Analytical and Bioanalytical Chemistry* **2007,** *387* (5), 1831-1840.

62. Pattnaik, P.; Srivastav, A., Surface plasmon resonance - applications in food science research: A review. *J. Food Sci. Technol.-Mysore* **2006,** *43* (4), 329-336.

63. Homola, J., *Surface plasmon resonance (SPR) biosensors and their applications in food safety and security*. Springer: Dordrecht, 2006; Vol. 216, p 101-118.

64. Roh, S.; Chung, T.; Lee, B., Overview of the Characteristics of Micro- and Nano-Structured Surface Plasmon Resonance Sensors. *Sensors 11* (2), 1565-1588.

65. Haes, A. J.; Van Duyne, R. P., Preliminary studies and potential applications of localized surface plasmon resonance spectroscopy in medical diagnostics. *Expert Rev. Mol. Diagn.* **2004,** *4* (4), 527-537.

66. Zhang, X.; Yonzon, C. R.; Young, M. A.; Stuart, D. A.; Van Duyne, R. P., Surface-enhanced Raman spectroscopy biosensors: excitation spectroscopy for optimisation of substrates fabricated by nanosphere lithography. *IEE Proceedings Nanobiotechnology* **2005,** *152* (6), 195-206.

67. Brown, C. W.; Li, Y.; Seelenbinder, J. A.; Pivarnik, P.; Rand, A. G.; Letcher, S. V.; Gregory, O. J.; Platek, M. J., Immunoassays based on surface enhanced infrared absorption spectroscopy. *Analytical Chemistry* **1998,** *70* (14), 2991-2996.

68. Dostalek, J.; Knoll, W., Biosensors based on surface plasmon-enhanced fluorescence spectroscopy. *Biointerphases* **2008,** *3* (3), FD12-FD22.

69. Itoh, T.; Kikkawa, Y.; Yoshida, K.; Hashimoto, K.; Biju, V.; Ishikawa, M.; Ozaki, Y., Correlated measurements of plasmon resonance Rayleigh scattering and surface-enhanced resonance Raman scattering using a dark-field microspectroscopic system. *J. Photochem. Photobiol. A-Chem.* **2006,** *183* (3), 322-328.

70. Yang, X.; Wang, Q.; Wang, K.; Tan, W.; Yao, J.; Li, H., Electrical Switching of DNA Monolayers Investigated by Surface Plasmon Resonance. *Langmuir* **2006,** *22* (13), 5654-5659.

71. Profumo, A.; Fagnoni, M.; Merli, D.; Quartarone, E.; Protti, S.; Dondi, D.; Albini, A., Multiwalled Carbon Nanotube Chemically Modified Gold Electrode for Inorganic As Speciation and Bi(III) Determination. *Analytical Chemistry* **2006,** *78* (12), 4194-4199.

72. Raether, H., *Surface plasmons on smooth and rough surfaces and on gratings*. Springer-Verlag, Berlin: 1988.

73. Willets, K. A.; Van Duyne, R. P., Localized surface plasmon resonance spectroscopy and sensing. In *Annual Review of Physical Chemistry*, Annual Reviews: Palo Alto, 2007; Vol. 58, pp 267-297.

74. Jensen, T. R.; Malinsky, M. D.; Haynes, C. L.; Van Duyne, R. P., Nanosphere lithography: Tunable localized surface plasmon resonance spectra of silver nanoparticles. *J. Phys. Chem. B* **2000,** *104* (45), 10549-10556.

75. Rindzevicius, T.; Alaverdyan, Y.; Dahlin, A.; Höök, F.; Sutherland, D. S.; Käll, M., Plasmonic Sensing Characteristics of Single Nanometric Holes. *Nano Letters* **2005,** *5* (11), 2335-2339.

76. Brolo, A. G.; Gordon, R.; Leathem, B.; Kavanagh, K. L., Surface Plasmon Sensor Based on the Enhanced Light Transmission through Arrays of Nanoholes in Gold Films. *Langmuir* **2004,** *20* (12), 4813-4815.

77. Jung, Y. S., Sun, Z., Wuenschell, J., Kim, H. K., Kaur, P., Wang, L., and Waldeck, D., High-sensitivity surface plasmon resonance spectroscopy based on a metal nanoslit array, *App. Phys. Lett.* **2006,** *88, 243105*.

78. De Bruijn, H. E.; Kooyman, R. P. H.; Greve, J., Choice of metal and wavelength for surface-plasmon resonance sensors: some considerations. *Appl. Opt.* **1992,** *31* (4), 440-442.

79. B. Liedberg, C. N., I. Lundstro □m, Surface plasmons

resonance for gas detection and biosensing. *Sensors and Actuators* **1983,** *4*, 299-304.

80. Matsubara, K.; Kawata, S.; Minami, S., Optical chemical sensor based on surface plasmon measurement. *Appl. Opt.* **1988,** *27* (6), 1160-1163.

81. C. Nylander, B. L., T. Lind, as detection by means of surface plasmons resonance. *Sensors and Actuators* **1982,** *3*, 79-88.

82. Liedberg, B.; Nylander, C.; Lunström, I., Surface plasmon resonance for gas detection and biosensing. *Sensors and Actuators* **1983,** *4* (0), 299-304.

83. L.M. Zhang, D. U., Optical chemical sensing em- ploying surface plasmon resonance. *Electron. Lett.* **1988,** *23*.

84. Karlsson, R.; Stahlberg, R., Surface Plasmon Resonance Detection and Multispot Sensing for Direct Monitoring of Interactions Involving Low-Molecular-Weight Analytes and for Determination of Low Affinities. *Analytical Biochemistry* **1995,** *228* (2), 274-280.

85. Cullen, D. C.; Lowe, C. R., A direct surface plasmon‚Äîpolariton immunosensor: Preliminary investigation of the non-specific adsorption of serum components to the sensor interface. *Sensors and Actuators B: Chemical* **1990,** *1* (1‚Äì6), 576-579.

86. D.C. Cullen, R. G. B., C.R. Lowe, Detection of immuno- complex formation via surface plasmon resonance on gold- coated diffraction gratings. *Biosensors and Bioelectronics* **1987,** *3*, 211-225.

87. M.J. Jory, P. S. V., J.R. Sambles, Development of a prototype gas sensor using surface plasmon resonance on gratings. *Sensors and Actuators B: Chemical* **1994,** *17*, 1203-1209.

88. Berger, C. E. H.; Beumer, T. A. M.; Kooyman, R. P. H.; Greve, J., Surface Plasmon Resonance Multisensing. *Analytical Chemistry* **1998,** *70* (4), 703-706.

89. Homola, J.; Yee, S. S.; Gauglitz, G. n., Surface plasmon resonance sensors: review. *Sensors and Actuators B: Chemical* **1999,** *54* (1-2), 3-15.

90. Ebbesen, T. W.; Lezec, H. J.; Ghaemi, H. F.; Thio, T.; Wolff, P. A., Extraordinary optical transmission through sub-wavelength hole arrays. *Nature* **1998,** *391* (6668), 667-669.

91. Ghaemi, H. F.; Thio, T.; Grupp, D. E.; Ebbesen, T. W.; Lezec, H. J., Surface plasmons enhance optical transmission through subwavelength holes. *Physical Review B* **1998,** *58* (11), 6779.

92. Krishnan, A.; Thio, T.; Kim, T. J.; Lezec, H. J.; Ebbesen, T. W.; Wolff, P. A.; Pendry, J.; Martin-Moreno, L.; Garcia-Vidal, F. J., Evanescently coupled resonance in surface plasmon enhanced transmission. *Optics Communications* **2001,** *200* (1-6), 1-7.

93. Degiron, A.; Lezec, H. J.; Barnes, W. L.; Ebbesen, T. W., Effects of hole depth on enhanced light transmission through subwavelength hole arrays. *Applied Physics Letters* **2002,** *81* (23), 4327-4329.

94. Bethe, H. A., Theory of Diffraction by Small Holes. *Physical Review* **1944,** *66* (7-8), 163.

95. Born, M.; Wolf, E., *Principles of Optics*. Pergamon, Oxford: 1980.

96. Bonod, N.; Enoch, S.; Li, L.; Evgeny, P.; Neviere, M., Resonant optical transmission through thin metallic films with and without holes. *Opt. Express* **2003,** *11* (5), 482-490.

97. Darmanyan, S. A.; Zayats, A. V., Light tunneling via resonant surface plasmon polariton states and the enhanced transmission of periodically nanostructured metal films: An analytical study. *Physical Review B* **2003,** *67* (3), 035424.

98. MartÌn-Moreno, L.; GarcÌa-Vidal, F. J.; Lezec, H. J.; Pellerin, K. M.; Thio, T.; Pendry, J. B.; Ebbesen, T. W., Theory of Extraordinary Optical Transmission through Subwavelength Hole Arrays. *Physical Review Letters* **2001,** *86* (6), 1114.

99. Salomon, L.; Grillot, F.; Zayats, A. V.; de Fornel, F., Near-Field Distribution of Optical Transmission of Periodic Subwavelength Holes in a Metal Film. *Physical Review Letters* **2001,** *86* (6), 1110.

100. Vigoureux, J. M., Analysis of the Ebbesen experiment in the light of evanescent short range diffraction. *Optics Communications* **2001,** *198* (4-6), 257-263.

101. Ozaki, M.; Kato, J.-i.; Kawata, S., Surface-Plasmon Holography with White-Light Illumination. *Science 332* (6026), 218-220.

102. Willets, K. A.; Van Duyne, R. P., Localized Surface Plasmon Resonance Spectroscopy and Sensing. *Annual Review of Physical Chemistry* **2007,** *58* (1), 267-297.

103. Hur, Y.; Ock, K.; Kim, K.; Jin, S.; Gal, Y.; Kim, J.; Kim, S.; Koh, K., Surface plasmon resonance study on enhanced refractive index change of an Ag+ ion-sensing membrane containing dithiosquarylium dye, *Anal. Chim. Acta* **2002,** *460*, 133.

104. Nakkach, M.; Lecaruyer, P.; Bardin, F.; Sakly, J.; Ben Lakhdar, Z.; Canva, M., Absorption and related optical dispersion effects on the spectral response of a surface plasmon resonance sensor, *Appl. Opt.* **2008,** *47*, 6177.

105. Wang, S.; Boussaad, S.; Tao, N. J., *Rev. Sci. Instrum.* **2001,** *72*, 3055.

106. Haes, A. J.; Zou, S.; Zhao, J.; Schatz, G. C.; Van Duyne, R. P., Localized Surface Plasmon Resonance Spectroscopy near Molecular Resonances. *Journal of the American Chemical Society* **2006,** *128* (33), 10905-10914.

107. Ni, W.; Yang, Z.; Chen, H.; Li, L.; Wang, J., Coupling between Molecular and Plasmonic Resonances in Freestanding Dye,àíGold Nanorod Hybrid Nanostructures. *Journal of the American Chemical Society* **2008,** *130* (21), 6692-6693.

108. Zhao, J.; Das, A.; Zhang, X.; Schatz, G. C.; Sligar, S. G.; Van Duyne, R. P., Resonance Surface Plasmon Spectroscopy:,Äâ Low Molecular Weight Substrate Binding to Cytochrome P450. *Journal of the American Chemical Society* **2006,** *128* (34), 11004-11005.

109. Zhao, J.; Jensen, L.; Sung, J.; Zou, S.; Schatz, G. C.; Van Duyne, R. P., Interaction of Plasmon and Molecular Resonances for Rhodamine 6G Adsorbed on Silver Nanoparticles. *Journal of the American Chemical Society* **2007,** *129* (24), 7647-7656.

110. Yeh, W.-H.; Kleingartner, J.; Hillier, A. C., Wavelength Tunable Surface Plasmon Resonance-Enhanced Optical Transmission Through a Chirped Diffraction Grating. *Analytical Chemistry* **2010,** *82* (12), 4988-4993.

111. Taniguchi, J.; Ide, S.; Unno, N.; Sakaguchi, H., Nanoprint lithography of gold nanopatterns on polyethylene terephthalate. *Microelectronic Engineering* **2009,** *86* (4–6), 590-595.

112. Guo, L. J., Nanoimprint lithography: Methods and material requirements. *Advanced Materials* **2007,** *19* (4), 495-513.

113. Abdulhalim, I., Zourob, M., Lakhtakia, A. Surface Plasmon Resonance for Biosensing: A Mini-Review. *Electromagnetics* **2008**, *28* 214-242

CHAPTER 2. WAVELENGTH TUNABLE SURFACE PLASMON RESONANCE-ENHANCED OPTICAL TRANSMISSION THROUGH A CHIRPED DIFFRACTION GTATING

Analytical Chemistry, **82** 4988-4993 (2010)

Wei-Hsun Yeh, Justin Kleingartner, Andrew C. Hillier

2.1 Abstract

We report the construction and testing of a chirped diffraction grating, which serves as a substrate for surface plasmon-enhanced optical transmission. This grating possesses a spatial variation in both pitch and amplitude along its surface. It was created by plasma oxidation of a curved poly(dimethoxysilane) sheet, which resulted in non-uniform buckling along the polymer surface. A gold-coated replica of this surface elicited an optical response that consisted of a series of narrow, enhanced transmission peaks spread over the visible spectrum. The location and magnitude of these transmission peaks varied along the surface of the grating and coincided with conditions where surface plasmons were excited in the gold film via coupling to one or more of the grating's diffracted orders. A series of measurements were carried out using optical diffraction, atomic force microscopy, and normal incidence optical transmission to compare the grating topology to the corresponding optical response. In addition, the impact of a thin dielectric coating on the transmission response was determined by depositing a thin silicon oxide film over the grating surface. After coating, wavelength shifts were observed in the transmission peaks, with the magnitude of the shifts being a function of the film thickness, the local grating structure, and the diffracted order associated with each peak. These results illustrate the ability of this

surface to serve as an information-rich optical sensor whose properties can be tuned by control of the local grating topology.

2.2 Results and Discussion

The interaction of light with nanostructured objects, particularly those containing metals, can produce a variety of unique and useful optical phenomena.[1,2] Examples include enhanced optical transmission,[3] super focusing through nanoapertures,[4,5] optical waveguides via nanoparticle chains,[6] and enhanced light generation in light emitting diodes via nanoscale optical coupling.[7] The origins of many of these optical phenomena can be traced to the excitation and propogation of surface plasmons in the nanostructured metal objects.[2] Notably, surface plasmon effects have been exploited in a variety of sensing applications.[8-11] Nanostructure-based plasmonic sensing has been achieved with nano-hole arrays,[12,13] single nanometric holes,[14] nanoslit arrays,[15] and various grating-type and diffractive nanostructures.[16-20]

The construction of nanostructured optical elements for plasmonic sensing can be achieved with a variety of processing techniques.[8] In addition to traditional top-down lithography methods, electron beam lithography and focused ion beam machining have been used to construct ordered and complex nanostructures.[4,12,21] Solution phase self-assembly techniques, including nanosphere[22,23] and colloidal[24] lithography are well-suited for creating ordered nanostructure arrays. Soft lithography using elastomeric stamps has also been used to construct nanostructures.[25] Another source of nanostructured surfaces capable of supporting surface plasmon excitation are diffraction gratings. Gratings are advantageous in that they are commercially available in a variety of forms, either as optical elements used for spectroscopy or

as CDs, DVD and blue-ray discs. In addition, gratings can be readily created via laser-based interferometry techniques.[19,26,27]

Grating-based SPR sensing has become increasingly popular due to several key advantages.[9,28] Gratings represent an inherently information-rich substrate due to surface plasmons appearing in not only the directly reflected or transmitted peaks, but also in the various diffracted orders.[27] In addition, the plasmon response is highly tunable based upon the size and shape of the grating topology. Indeed, changing the amplitude, shape or pitch of the grating profile has a dramatic effect on the wavelength and shape of the plasmon resonance.[19,29,30] Thus, this substrate represents a highly flexible and tunable platform for sensor development.

We previously demonstrated that a diffraction grating constructed from a commercial DVD supported surface plasmon enhanced light transmission when coated with a thin gold film.[20] This enhancement consisted of narrow peaks in the visible spectrum, whose central wavelength could be tuned by simple rotation of the grating. This surface plasmon-enhanced transmission resulted in a surface that was highly sensitive to the local refractive index near the gold interface and, thus, could be used in optical sensing applications. Measurement of the thickness of several alkane-thiolate monomolecular thin films and detection of the formation of an antigen-antibody complex of BSA-antiBSA was demonstrated using this sensing method.[20]

In the work described here, enhanced optical transmission is demonstrated using a grating with chirped surface profile. We constructed chirped gratings using a technique based upon the surface buckling that occurs following oxidation of elastomeric films such as poly(dimethylsiloxane) PDMS (experimental details are provided in Supplementary Information).[31,32] Briefly, ~2 mm thick PDMS sheets were cast and cut into 25 x 75 mm pieces. These were then bent along their long axis, clamped in an elongated circular fixture, and exposed

to a oxygen plasma for a period of ~4 min. Following plasma treatment, the fixture was removed and the PDMS pieces were allowed to relax back to a planar shape. This resulted in spontaneous buckling of the PDMS surface to produce a sinusoidal relief pattern, whose amplitude and pitch varied along the sample surface.[31] Control of the pitch and amplitude of the surface buckling was achieved by control of the curvature and the sample oxidation time. The largest surface buckling (greatest pitch and amplitude) occurred where the PDMS surface had the largest curvature (i.e., at the center of the bend). The buckling decreased in magnitude to leave a smooth topography at the far edges of the sample, where the surface had remained flat during oxidation. Limiting the oxidation time to ~4 min produced an oxide thickness that created surface undulations with pitch values between 500 and 1500 nm. Longer oxidation times result in larger pitch values.[31,33]

An optical image of a PDMS film shows a color pattern illustrating the diffractive nature of the nanoscale surface buckling (Fig.1A). In the center of the sample (denoted by the white line), a gradual color change is observed along the x-axis (buckling direction) that varies gradually from clear to green to red and then back again. The reflected colors are due to optical diffraction and reflect the changing surface buckling along the surface. The central 50% of the sample shows this consistent pattern, while the outer 25% (top and bottom) show a more non-uniform color pattern. The outer edges of the sample buckled in a more non-uniform manner than the center. We suspect that this “edge effect” was the result of changes in the stress distribution near the edge of the sample and also from

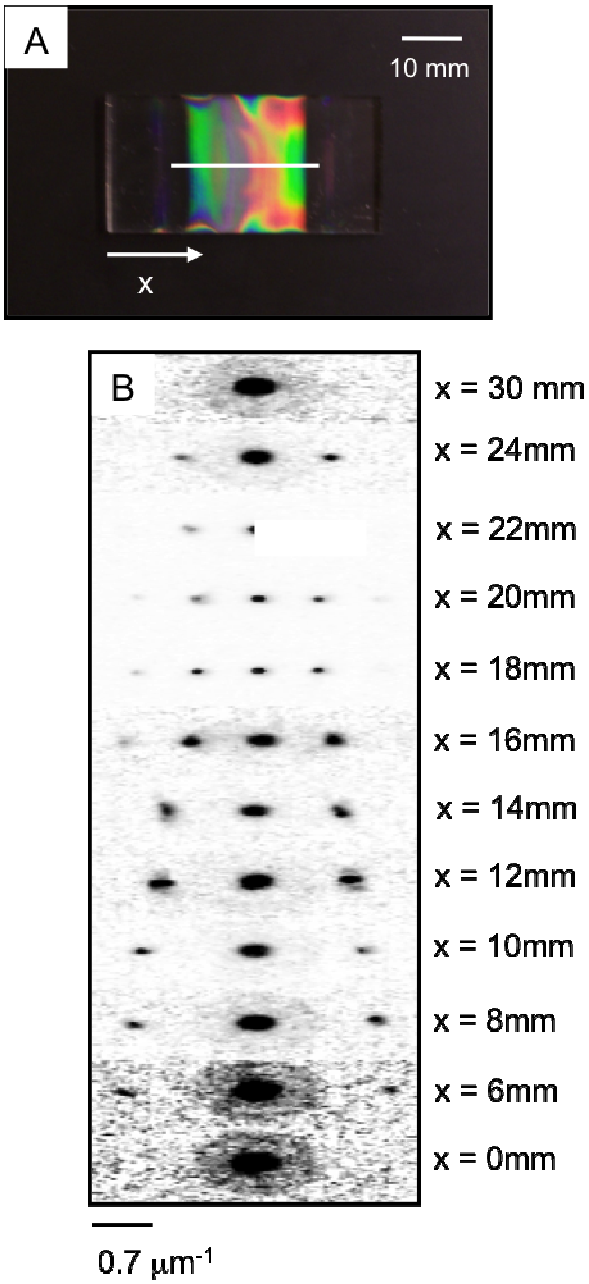

Figure 1 (A) Optical image showing reflection from a chirped diffraction grating made from oxidized PDMS elastomer. White line over image indicates central path along sample used in subsequent measurements. The x-direction indicates the bend axis and, thus, the direction of surface buckling. In subsequent figures, the x-axis is used to denote this direction. (B) Optical diffraction images (inverted contrast) acquired from transmission of 630 nm light at various x-positions along the center of the diffraction grating.

oxidation of both the top and the sides of the PDMS in this region. Consequently, all subsequent measurements were performed only along the center line of the sample (denoted by the white line in Fig.1A).

A clearer indication of the periodic nature of the surface can be seen using optical diffraction. Fig.1B depicts a series of optical diffraction images acquired at several x-positions along the central region of the PDMS sample (experimental details are provided in Supplementary Information). These images were acquired using an optical microscope having a Bertrand lens attachment, which focuses a Fourier spectrum of the sample image on the microscope's imaging plane.[34,35] The far left side of the sample, indicated by the bottom diffraction panel in Fig.1B (x = 0 mm), displays a diffuse diffraction pattern with a single, central spot corresponding to directly transmitted light. This diffraction image reflects the lack of periodic order on the surface. The next panel (x = 6 mm) shows two clear spots at the left and right sides of the central spot corresponding to first order diffraction. The spacing of these spots is ~1.7 μm^{-1}, which reflects an average period of surface buckling at ~600 nm. Additional diffraction images acquired along the length of the buckled region show first order diffraction spots with an initially large spacing, indicating a small pitch value for the surface bulking. As the center of the PDMS sample is approached (x = 18 mm), the spacing of the first order diffraction peaks decreases and achieves a minimum value of ~0.75 μm^{-1}, corresponding to a maximum pitch of ~1450 nm. Additional diffraction images acquired along the sample to the right of center show the spacing for the first order diffraction spots increasing again, indicating a decrease in the surface pitch. The diffraction spots disappear at the far right side of the sample (x = 30 mm) where the surface once again becomes flat.

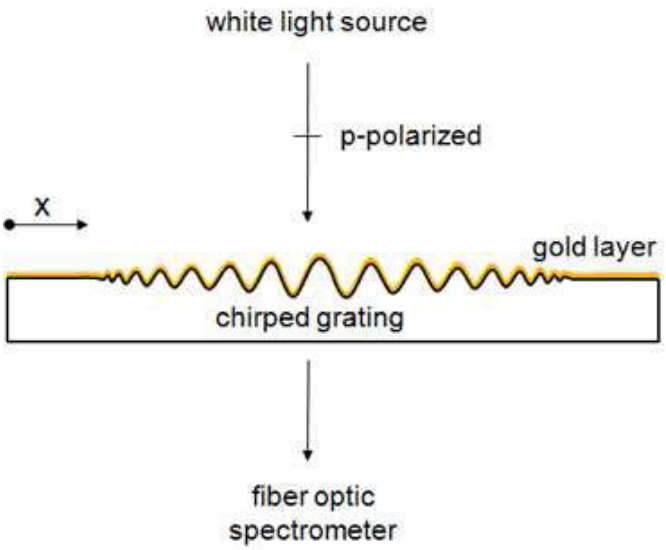

Scheme 1 Schematic of chirped diffraction grating and optical configuration. The grating pitch and amplitude (buckling) increase towards the center of the sample. The buckling direction (x-axis) is noted and p-polarized light is oriented along that direction.

These optical diffraction images illustrate a variable surface profile due to the nonuniform surface buckling of the PDMS.

In order to use this sample for surface plasmon experiments, a rigid, gold-coated replica of this grating was created (see details in Supplementary Information). Scheme 1 shows a schematic of the replica of the chirped diffraction grating with a ~40 nm gold coating. In this schematic, both the pitch and amplitude of the grating vary as a function of distance along the sample surface. Details of this surface topology, including both the pitch and amplitude of the gold-coated replica, were further verified with atomic force microscopy (Fig.2A). An image from the far left side of the sample at x = 0 mm shows a nominally flat surface. The surface buckling associated with the chirped grating surface is evident at x = 16 mm. The image shows a series of ridges and valleys and indicates that the shape of the surface buckling follows a sinusoidal pattern.

A summary of the AFM measurements is given in Fig.2B, where the pitch of the grating and the amplitude of the surface buckling are plotted as a function of position along the sample surface. At the far left (x < 5 mm) and right (x > 25 mm), no noticeable surface undulations were observed. At x = 5 mm, surface buckling is first observed, with a small amplitude of < 15 nm and a pitch of ~600 nm. Gradual increases in both the pitch and amplitude of the surface buckling occur when moving along the sample to the right. Maxima in both parameters are observed at x = 19 mm, where the pitch is 1475 nm and the amplitude is 245 nm. Additional measurements to the right of this position exhibit decreases in the magnitude of both the pitch and amplitude until the surface becomes smooth again at all positions of x > 25 mm.

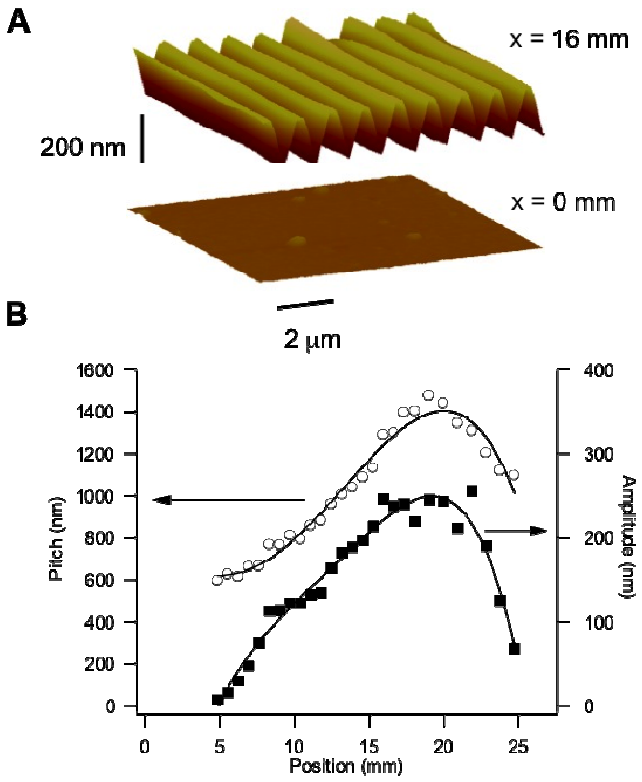

Figure 2 (A) Atomic force microscope (AFM) images of gold-coated chirped diffraction grating at positions of x = 0 and x = 16 mm along the sample surface. (B) Summary of pitch (open circles) and amplitude (filled squares) as measured by AFM along the sample x direction.

Previous studies have shown that diffraction gratings can excite surface plasmon resonance, and the details of this coupling are highly sensitive to the pitch[19,29] and the amplitude[30] of the grating. The orientation of the grating can also be used to modify the resonance condition and tune the wavelength in which coupling to surface plasmons occurs.[20] Since the chirped diffraction grating developed here possesses a variation in both pitch and amplitude as a function of position, it is anticipated that this will result in a variable surface plasmon coupling along the surface of the sample. Fig.3 depicts a series of measurements from optical transmission experiments that show this very behavior. The optical transmission data is given as the ratio of transmitted p-polarized to s-polarized light (T_p/T_s), and regions where surface plasmon excitation occurs is observed as an enhancement of this ratio over the nominal value of 1. Similar results were also obtained by using a flat region of the gold-coated sample as a reference for the p-polarized transmission spectra. All measurements were performed at normal incidence (Scheme 1), where p-polarization is defined as light polarized parallel to the buckling direction (x-axis), or perpendicular to the ridges on the buckled surface.

Transmission spectra through the grating at several different surface locations are shown in Fig.3A. At the far left of the sample where the surface is flat, a uniform transmission of $T_p/T_s = 1$ is seen. The transmission changes markedly at locations further along the sample. At x = 10 mm, where the pitch and amplitude of the grating are 810 nm and 120 nm, respectively, two transmission peaks are seen. A small peak is observed at ~ 550 nm and a larger peak is seen with a maximum near 850 nm. The origin of these peaks can be deduced by considering the momentum matching condition between the wavevector of the surface plasmons (k_{sp}) with that of the incident p-polarized light interacting with the diffraction grating (k_{gr}) as given in Eqn.1.

$$k_{sp} = \frac{2\pi}{\lambda}\sqrt{\frac{\varepsilon_M^{'}\varepsilon_D}{\varepsilon_M^{'}+\varepsilon_D}} = \frac{2\pi}{\lambda}\sqrt{\varepsilon_D}sin(\theta) + m\frac{2\pi}{\Lambda} = k_{gr} \qquad (1)$$

At an incident angle of $\theta = 0°$, this equality may be satisfied by several different diffracted orders (m) for a given value of the grating pitch (Λ) and dielectric constants for metal ($\varepsilon_M = \varepsilon_M' + \varepsilon_M''$) and dielectric ($\varepsilon_D$) layers. At a grating pitch of $\Lambda = 810$ nm, for example, the first diffracted order (m = 1) will satisfy this momentum matching condition for a gold coating in air at $\lambda \sim 820$ nm, while the second diffracted order (m = 2) will satisfy this condition at $\lambda \sim 500$ nm. Thus, the two peaks seen in the transmission spectrum at x = 10 mm are due to excitation of surface plasmons via the first and second diffracted orders at the corresponding surface pitch.

Transmission spectra from additional locations along the surface illustrate the impact of the surface profile on the plasmon coupling. With increasing grating pitch, the excitation peaks for a given diffracted order shift to longer wavelengths, which is consistent with Eqn.(1). At x = 12 mm, for example, the first order peak has shifted ~100 nm to the right and the maximum has moved to edge of the spectrometer's data window (~ 950 nm). The second order peak has also shifted to the right, with its maximum now located near ~600 nm. In addition to the red-shifting of the peak positions, the magnitude of the enhanced transmission has also increased due, in part, to the increase in grating amplitude. Additional measurements at x = 14, 16 and 18 mm show the shifting of the m = 2 peak from its original location at ~ 550 nm to > 900 nm. The magnitude of this peak has also grown to give an enhancement in the p-polarized transmission response of over 8 times (> 800%). At x = 16,

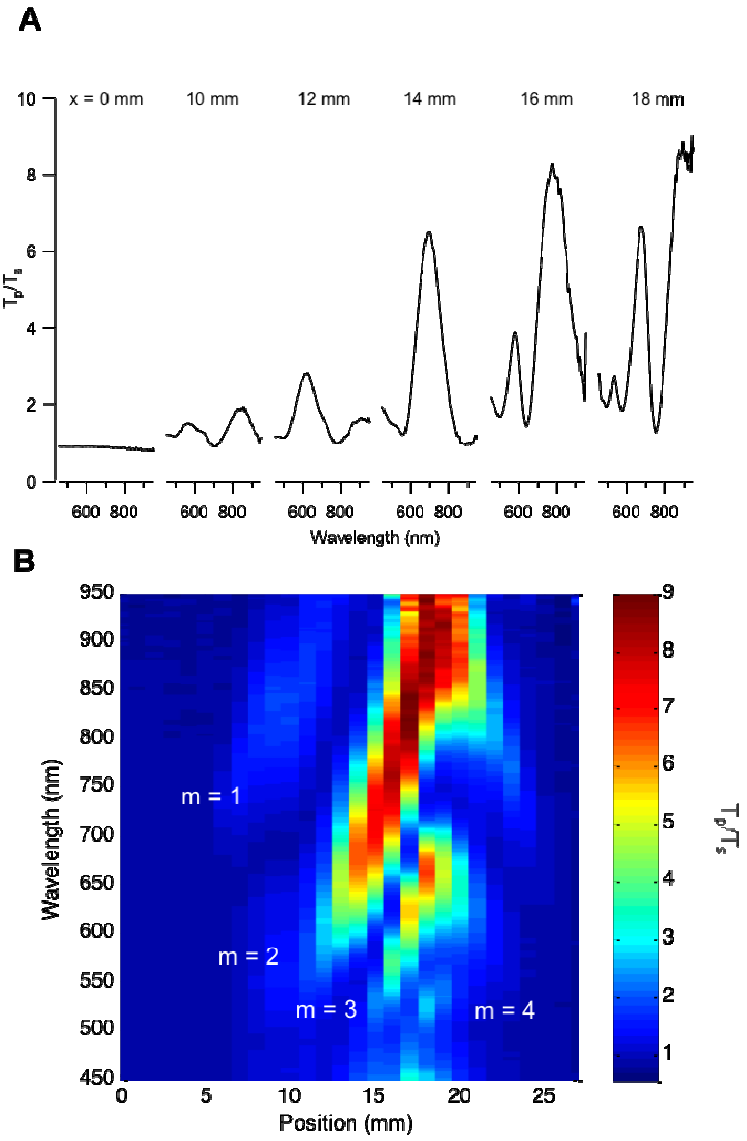

Figure 3 (A) Selection of transmission spectra (T_p/T_s) as a function of x-position along the center of the gold-coated diffraction grating. (B) Compilation image of transmission spectra (T_p/T_s) acquired every 1 mm between x = 0 and x = 19 mm along the center of the gold-coated diffraction grating. The diffraction order (m) associated with each transmission peak is noted on the figures.

an additional peak is observed at ~550 nm, which is due to surface plasmon excitation via the third (m = 3) diffracted order. At x = 18 mm, three peaks appear at ~900, 670 and 530 nm, corresponding to the m = 2, 3 and 4 diffracted orders.

A summary of these measurements is shown as a two-dimensional image in Fig.3B depicting T_p/T_s versus wavelength as a function position along the sample surface. At the far left side of the sample, the transmission response is uniform with T_p/T_s= 1, indicating the lack of enhanced transmission, as would be expected for this flat surface. A number of transmission peaks are observed when approaching the central region of the sample. The series of peaks corresponding to the m = 1, 2, 3 and 4 diffracted orders are identified on the plot. In this sample, the transmission peaks due to the m = 2 diffracted order are the most pronounced and exist over a large region of the sample. It is expected that coupling to the m = 1 order would also be quite large, but those peaks quickly move into the near-infrared region and, thus, are not observed by our detector.

In a typical surface plasmon resonance-based sensor system, a sample is interrogated at a single orientation, sample geometry, and wavelength. In contrast, the chirped sample construction described here allows the design of very information rich measurements, where one can acquire numerous signals of sample perturbation in a single experiment. In particular, this chirped grating construction, where a multitude of grating pitch values are presented, provides simultaneous information about changes in the plasmon resonance condition over a large portion of the visible spectrum and simultaneously at several different diffracted orders, each of which are expected to provide a different sensitivity to changes in refractive index.

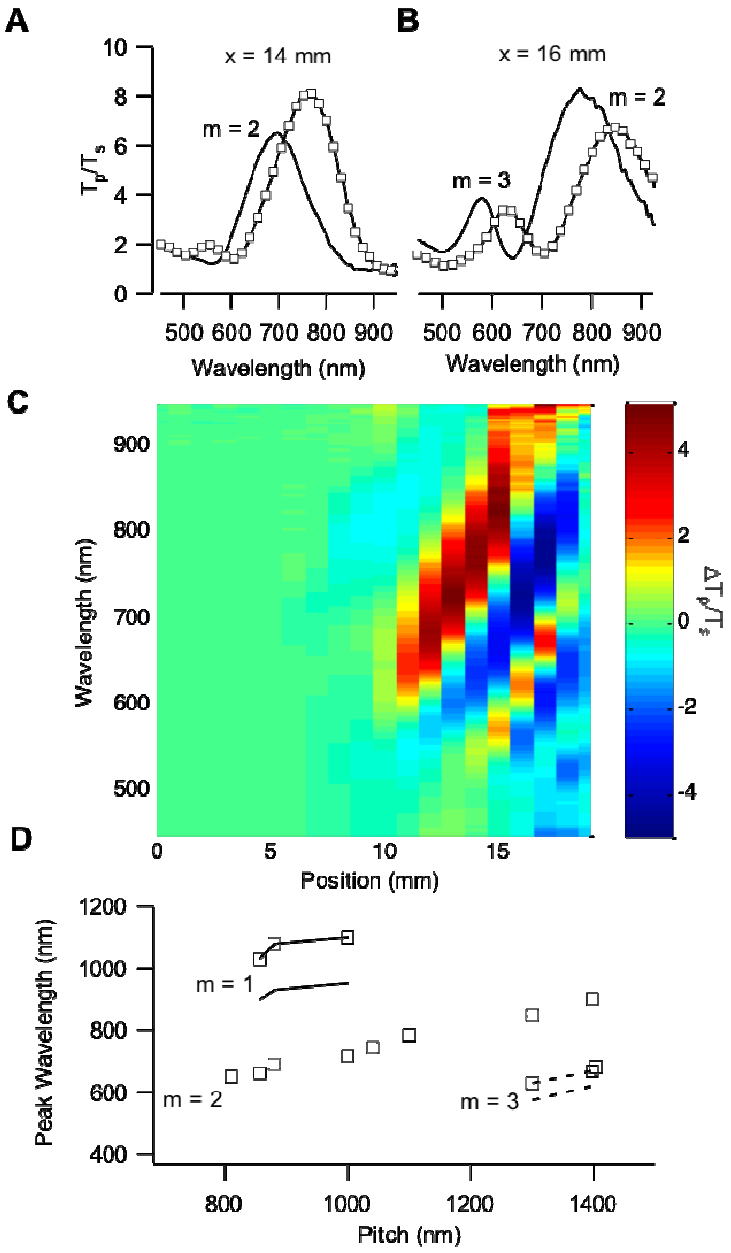

Figure 4 (A) Transmission spectra at x = 14 mm with (open squares) and without (solid line) 26 nm SiO film. (B) Transmission spectra at x = 16 mm with (open squares) and without (solid line) SiO film. (C) Subtraction image showing difference in transmission ($\Delta T_p/T_s$) for chirped grating with and without SiO film as a function of x-position along the grating. (D) Plot of shift in peak wavelength for grating orders m = 1, 2 and 3 with (open squares) and without (lines) SiO film as a function of measured grating pitch.

As a test of the ability of this chirped grating to serve as a thin film sensor, a coating of silicon oxide (SiO) was evaporated over the grating surface to a thickness of ~26 nm, as verified with atomic force microscopy. Shifts in the transmission peaks at various locations along the grating were then recorded. Fig.4A and B illustrate transmission measurements at two locations (x = 14 and 16 mm) before and after coating of the SiO film. At x = 14 mm, a single peak corresponding to surface plasmon excitation from the m = 2 order is seen. Following film coating, the peak shifts to longer wavelengths by ~58 nm. At x = 16 mm, two peaks appear due to the m = 2 (780 nm) and m = 3 (570 nm) diffracted orders. Both peaks shift to longer wavelengths by 70 nm (m = 2) and 55 nm (m = 3), respectively. These results clearly show that the transmission peaks are sensitive to the presence of a thin film or, more generally, to a change in the refractive index of a dielectric layer near the gold surface.

A more complete view of the response of this chirped grating to the SiO film coating can be seen in the image in Fig.4C. This figure depicts the difference in transmission ($\Delta T_p/T_s$), as determined by subtracting the optical response of the bare gold grating from that of the grating with the SiO film, as a function of position on the left side of the sample ($0 < x < 20$ mm). In this image, the transmission peaks from Fig.3B are replaced with a pair of peaks reflecting the shift in wavelength due to the SiO film. The intensity of the peaks in Fig.4C reflect the magnitude of the transmission, while the difference between the positive (red) and negative (blue) peaks reflects the magnitude of the peak shift. Notably, the amount of the shift for a given peak is related to the sensitivity of a given transmission peak to the change in refractive index resulting from the SiO film.

In Fig.4C, it is clear that the peaks due to all four of observed diffracted orders (m = 1,2,3 and 4) red-shift in response to the SiO film. In addition, the magnitude of the shifts varies over

the sample. This behavior is summarized in Fig.4D, which plots the peak positions with and without the SiO film as a function of the substrate pitch. These points were determined by fitting the transmission peaks to a Gaussian function in order to accurately determine the peak wavelength, and then mapping those values to the measured pitch values corresponding to that sample location. The most notable feature in these data is that the sensitivity, or the magnitude of the shift in peak wavelength, differs for each of the diffracted orders. Indeed, comparing the average wavelength shift for this 26 nm SiO film gives values of 143, 68, and 43 nm for the diffracted orders m = 1, 2 and 3. This suggests that for a given pitch value, the peak corresponding to the lowest diffracted order gives the highest sensitivity. This can be explained by considering the coupling condition described in Eqn.(1). The wavelength sensitivity can be deduced by solving this relationship at the wavelength where grating coupling occurs ($\lambda_{G\text{-}spr}$) and taking the derivative with respect to changes in refractive index of the dielectric layer (n_D). A complete analysis of this sensitivity has been considered previously,[28] so only a simplified view will be given here. The sensitivity of the transmission peaks for the grating ($S_{G\lambda}$) can be shown as in Eqn.(2).

$$S_{G\lambda} = \frac{d}{dn_D}\left[\lambda_{G-spr}\right] = \frac{\Lambda}{m}\frac{d}{dn_D}\left[\sqrt{\frac{\varepsilon_M' n_D^2}{\varepsilon_M' + n_D^2}}\right] \qquad (2)$$

Where the dielectric constant of the dielectric layer is written in terms of the refractive index ($\varepsilon_D = n_D^2$). The right hand term within the square brackets in this expression approaches a constant value equal to n_D at longer wavelengths, where the real part of the metal's dielectric constant (ε'_M) becomes large and negative.[36] This condition is reached as the coupling wavelength exceeds the plasma wavelength ($\lambda > \lambda_p$) of the metal. In this limit, the sensitivity can be written in a simplified form (Eqn.3).

$$S_{G\lambda} \cong \frac{\Lambda}{m} \quad (3)$$

Thus, the wavelength sensitivity for the grating to changes in the refractive index in the dielectric layer is a function of both the pitch and order of the grating. Increasing the grating pitch increases the sensitivity, while increasing the diffracted order decreases the sensitivity. For the purposes of the work described here, this means that for a given grating pitch value, the peaks corresponding to the lowest diffraction orders have the highest sensitivity, and this sensitivity decreases inversely with increasing diffracted orders. This response is consistent with the average values of 143, 68, and 43 nm as noted earlier for the average peak shifts for the diffracted orders m = 1, 2 and 3. Another way to write Eqn.(3) is an equivalent expression in terms of coupling wavelength and refractive index (Eqn.(4)).

$$S_{G\lambda} \cong \frac{\lambda_{G-spr}}{n_D} \quad (4)$$

This expression reflects an increasing sensitivity at longer wavelengths, and a decreasing sensitivity with increasing refractive index of the dielectric layer. A comparison of Eqn.4 and Eqn.3 indicates that coupling at a given wavelength could be achieved with several different pitch/order combinations, such as Λ/m = 1500/2 = 750 nm or Λ/m = 750/1 = 750 nm, and each would have the same sensitivity for a given refractive index change.

2.3 Conclusion

The optical properties of nanostructured objects pose considerable promise for the development of simple, yet highly robust and sensitive analytical sensors. In this work, we have described a nanostructured chirped diffraction grating, which can serve as an information-rich surface plasmon-based optical sensor. The presence of numerous transmission peaks in a single sample, which are due to changing surface topology as well as originating from several

diffracted orders, provides a wealth of information about a surface film. In addition to providing redundancy to the measurement, this added information could be used to expand the capabilities of plasmon sensing. For example, with a single wavelength SPR measurement, one must assume a refractive index in order to determine a film thickness. With a two-wavelength measurement, both refractive index and thickness can be determined. However, with peaks appearing at a multitude of wavelengths as occurs with this chirped grating, a data set is provided that could be used to accurately determine the optical properties of a film, including thickness and wavelength-dependent refractive index, over a large region of the visible spectrum. Thus, this could also be used as a spectroscopic tool. We anticipate that these types of nanostructured sensors will have increasing utility in various sensing applications due to their sensitivity, flexibility, and ability to be readily adapted into array-type imaging systems. Grating-based strategies for optical sensing also have the advantage of being based upon a mature, inexpensive, yet highly flexible technology for grating fabrication that could be used in the development of a variety of sample formats.

2.4 Acknowledgment

This work was funded by the National Science Foundation (CHE 0809509), the National Institutes of Health (R44 RR023763- 02), and the W. M. Keck Foundation through the W. M. Keck Laboratory for High Throughput Atom-Scale Analysis at Iowa State University.

2.5 Supporting Information

2.5.1 Method: Chirped Grating Construction

We constructed gratings with a chirped profile using a technique based upon the surface

buckling that occurs following oxidation of elastomeric films such as poly(dimethylsiloxane) PDMS. Briefly, ~2 mm thick PDMS sheets were cast and cut into 25 x 75 mm pieces. These were then bent along the long axis and clamped in a fixture possessing a slightly elongated semi-circular shape. The PDMS film and fixture were placed in an oxygen plasma (Harrick Scientific) for a period of ~4 min. Following plasma treatment, the fixture was removed and the PDMS pieces were allowed to relax back to a planar shape. Upon relaxation, the surface of the PDMS spontaneously buckled to produce a sinusoidal relief pattern whose amplitude and pitch varied along the sample surface. This buckling has been shown to be the result of a stress-relief mechanism associated with the oxidized PDMS surface. The pitch and amplitude of the buckling are a function of the oxide thickness and the curvature of the sample during oxidation. These features can be controlled by manipulating the sample curvature and the oxidation time.

In the sample described in this work, the largest surface buckling occurred where the PDMS surface had the largest curvature and, thus, experienced the greatest strain (i.e., at the center of the bend). The buckling decreased in magnitude to leave a smooth topography at the far edges of the sample, which is where the surface had remained flat during oxidation. Limiting the oxidation time to ~4 min produced an oxide thickness that created surface undulations with pitch values between 500 and 1500 nm. Longer oxidation times result in larger pitch values.

2.5.2 Methods: Grating Replica

The “rainbow tinted” PDMS sheet was silanized by (tridecafluoro-1,1,2,2-tetrahydrooctyl)trichlorosilane (Gelest Inc.) vapor. A UV curable polyurethane (NOA68, NorlandProducts, Inc.) was carefully poured on the silanized surface to avoid bubbles. The sample was exposed to UV light for ~ 15 minutes. After UV curing, the solid polyurethane film was carefully peeled off. The PDMS sheet was stored in a desiccator for future replication. The

replicate solid PU film was deposited with a gold film with thickness of ~ 40 nm by thermal evaporation.

2.5.3 Methods: Optical Diffraction

Methods: Optical Diffraction

Optical diffraction images were acquired using an optical microscope (Olympus B41) in transmission mode, a white light source with a bandpass interference filter centered at 630 nm (Edmund Optics), and a Bertrand lens attachment on the microscope. The Bertrand lens focuses a Fourier spectrum of the sample image on the microscope's imaging plane to allow capture of optical diffraction data.

2.5 References

(1) Xia, Y.; Halas, N. J. *MRS Bull.* **2005**, *30*, 338.

(2) Barnes, W. L.; Dereux, A.; Ebbesen, T. W. *Nature* **2003**, *424*, 824.

(3) Ebbesen, T. W.; Lezec, H. J.; Ghaemi, H. F.; Thio, R.; Wolff, P. A. *Nature* **1998**, *391*, 667.

(4) Lezec, H. J.; Degiron, A.; Devaux, E.; Linke, R. A.; Martin-Moreno, L.; Garcia-Vidal, F. J.; Ebbesen, T. W. *Science* **2002**, *297*, 820.

(5) Garcia-Vidal, F. J.; Martin-Moreno, L.; Lezec, H. J.; Ebbesen, T. W. *Appl. Phys. Lett.* **2003**, *83*, 4500.

(6) Bozhevolnyi, S. I.; Volkov, V. S.; Leosson, K. *Phys. Rev. Lett.* **2002**, *89*, 186801.

(7) Hobson, P. A.; Wedge, S.; Wasey, J. A. E.; Sage, I.; Barnes, W. L. *Adv. Mat.* **2002**, *14*, 1393.

(8) Stewart, M. E.; Anderton, C. R.; Thompson, L. B.; Maria, J.; Gray, S. K.; Rogers, J. A.; Nuzzo, R. G. *Chem. Rev.* **2008**, *108*, 494.

(9) Homola, J. *Chem. Rev.* **2008**, *108*, 462.

(10) Haes, A. J.; Haynes, C. L.; McFarland, A. D.; Schatz, G. C.; Van Duyne, R. P.; Zou, S. *MRS Bull.* **2005**, *30*, 368.

(11) Homola, J. *Anal. and Bioanal. Chem.* **2003**, *377*, 528.

(12) Brolo, A. G.; Gordon, R.; Leathem, B.; Kavanagh, K. L. *Langmuir* **2004**, *20*, 4813.

(13) Williams, S. M.; Rodrigues, K. R.; Teeters-Kennedy, S.; Stafford, A. D.; Bishop, S. R.; Lincoln, U. K.; Coe, J. V. *J. Phys. Chem. B* **2004**, *108*, 11833.

(14) Rindzevicius, T.; Alaverdyan, Y.; Dahlin, A.; Hook, F.; Sutherland, D. S.; Kall, M. *Nano Lett.* **2005**, *5*, 2335.

(15) Jung, Y. S.; Sun, Z.; Wuenschell, J.; Kim, H. K.; Kaur, P.; Wang, L.; Waldeck, D. *App. Phys. Lett.* **2006**, *88*.

(16) Yu, F.; Tian, S. J.; Yao, D. F.; Knoll, W. *Anal. Chem.* **2004**, *76*, 3530.

(17) Tian, S. J.; Armstrong, N. R.; Knoll, W. *Langmuir* **2005**, *21*, 4656.

(18) Singh, B. K.; Hillier, A. C. *Anal. Chem.* **2006**, *78*, 2009.

(19) Adam, P.; Dostalek, J.; Homola, J. *Sens. and Act. B* **2006**, *113*, 774.

(20) Singh, B. K.; Hillier, A. C. *Anal. Chem.* **2008**, *80*, 3803.

(21) Stark, P. R. H.; Halleck, A. E.; Larson, D. N. *Methods* **2005**, *37*, 37.

(22) Haes, A. J.; Van Duyne, R. R. *J. Amer. Chem. Soc.* **2002**, *124*, 10596.

(23) Haynes, C. L.; Van Duyne, R. R. *J. Phys. Chem. B* **2001**, *105*, 5599.

(24) Prikulis, J.; Hanarp, P.; Olofsson, L.; Sutherland, D. S.; Kaell, M. *Nano. Lett.* **2004**, *4*, 1003.

(25) Xia, Y.; Whitesides, G. M. *Ann. Rev. Mater. Sci.* **1998**, *28*, 153.

(26) Hutley, M. C. *Diffraction Gratings*; Academic Press: London, 1982.

(27) Dostalek, J.; Homola, J.; Miler, M. *Sens. and Act. B* **2005**, *107*, 154.

(28) Homola, J.; Koudela, I.; Yee, S. S. *Sens. and Act. B* **1999**, *54*, 16.

(29) Zhang, N.; Schweiss, R.; Zong, Y.; Knoll, W. *Electrochim. Acta* **2006**, *52*, 2869.

(30) Kitson, S. C.; Barnes, W. L.; Bradberry, G. W.; Sambles, J. R. *J. Appl. Phys.* **1996**, *79*, 7383.

(31) Bowden, N.; Huck, W. T. S.; Paul, K. E.; Whitesides, G. M. *Appl. Phys. Lett.* **1999**, *75*, 2557.

(32) Jiang, X.; Takayama, S.; Qian, X.; Oxtuni, E.; Wu, H.; Bowden, N.; LeDuc, P.; Ingber, D. E.; Whitesides, G. M. *Langmuir* **2002**, *18*, 3273.

(33) Bowden, N.; Brittain, S.; Evans, A. G.; Hutchinson, J. W.; Whitesides, G. M. *Nature* **1998**, *393*, 146.

(34) Zhao, B.; Asundi, A. *Opt. Eng.* **1999**, *38*, 170.

(35) Kondrachova, L. V.; May, R. A.; Cone, C. W.; Bout, D. A. V.; Stevenson, K. J. *Langmuir* **2009**, *25*, 2508.

(36) Etchegoin, P. G.; Le Ru, E. C.; Meyer, M. *J. Chem. Phys.* **2006**, *125*, 164705.

CHAPTER 3 DIFFRACTION-BASED TRACKING OF SURFACE PLASMON RESONANCE ENHANCED TRANSMISSION THROUGH A GOLD-COATED GRATING

Analytical Chemistry, **83** 6047-6053 (2011)

Wei-Hsun Yeh, Joseph W. Petefish, Andrew C. Hillier

3.1 Abstract

Surface plasmon resonance enhanced transmission through metal-coated nanostructures represents a highly sensitive yet simple method for quantitative measurement of surface processes and is particularly useful in the development of thin film and adsorption sensors. Diffraction-induced surface plasmon excitation can produce enhanced transmission at select regions of the visible spectrum, and wavelength shifts associated with these transmission peaks can be used to track adsorption processes and film formation. In this report, we describe a simple optical microscope-based method for monitoring the first-order diffracted peaks associated with enhanced transmission through a gold-coated diffraction grating. A Bertrand lens is used to focus the grating's diffraction image onto a CCD camera, and the spatial position of the diffracted peaks can be readily transformed into a spectral signature of the transmitted light without the use of a spectrometer. The surface plasmon peaks appear as a region of enhanced transmission when the sample is illuminated with p-polarized light, and the peak position reflects the local dielectric properties of the metal interface, including the presence of thin films. The ability to track the position of the plasmon peak and, thus, measure film thickness is demonstrated using the diffracted peaks for samples possessing thin films of silicon oxide. The experimental results are

then compared with calculations of optical diffraction through a model, film-coated grating using the rigorously coupled wave analysis simulation method.

3.2 Introduction

Coupling of light with nanostructured objects leads to a variety of unique and potentially useful optical phenomena.[1] Some of the more interesting examples involve the coupling of light to nanostructured metal surfaces, which can lead to what is known as enhanced or extraordinary optical transmission.[2] The origins of enhanced transmission through metal films can be traced to the excitation of surface plasmons (SPs) in the nano- structured metal interface.[1b] The high sensitivity of these SPs to the local dielectric conditions at the metal interface can be exploited in sensor development.3 Examples of nanostructure-based plasmonic sensing include nanostructures consisting of nanohole arrays,[4] single nanometric holes,[5] nanoslit arrays,[6] and various grating-type and diffractive nanostructures.[7]

A variety of fabrication strategies can be used to create nano-structured optical elements ranging from electron beam lithography to colloidal nanosphere lithography.[4a,8] Beyond these specialized methods, one can exploit the features of commercially available diffraction gratings as nanostructured elements. Indeed, optical sensors and SP-based sensing platforms that exploit gratings have become increasingly popular.[9] Gratings represent an inherently information- rich substrate due to SPs appearing not only in the directly reflected and transmitted peaks, but also in the various diffracted orders.[10] In addition, the SP response is highly tunable on the basis of the size and shape of the grating surface. Indeed, changing the amplitude, shape, or pitch of the grating profile has a dramatic effect on the details of SPs.[7d,11] Thus, this substrate represents a highly flexible and tunable platform for sensor development.

We and others have previously demonstrated that a diffraction grating constructed from a commercial DVD supported SP-enhanced light transmission when coated with a thin metal film.[7e,12] The observed enhanced transmission consists of narrow peaks in the visible spectrum, whose central wavelength can be tuned by simple rotation of the grating. In the work presented here, we describe a simple optical microscope-based method for monitoring the first-order diffracted peaks associated with enhanced transmission through a gold-coated diffraction grating. We illustrate how peaks associated with SP excitation can be observed by tracking the light transmitted through the ± 1 diffracted orders. Diffracted light is monitored by using a Bertrand lens to focus the grating's diffraction image onto a CCD camera.[13] The spatial position of the diffracted peaks are then transformed through a simple calibration procedure into a spectral signature of the transmitted light without the use of a spectrometer. The ability to track the position of the plasmon peak and, thus, measure film thickness using the diffracted light is demonstrated for thin films of silicon oxide. The experimental results are then compared with calculations on the basis of an optical model of the grating interface as determined using the rigorously coupled wave analysis simulation method.

3.3 Experimental Section

3.3.1 Material and Reagents

Absolute ethanol and nitric acid were purchased from Sigma Aldrich (St. Louis, MO). All chemicals and reagents were used as received. Deionized water with electrical resistivity greater than 18 MΩ•cm was used during rinsing and cleaning procedures (NANOPure, Barnstead, Dubuque, IA). Recordable digital versatile discs (DVD-R, 4.7GB) were purchased from Inkjet Art Solutions (Salt Lake City, UT). Gold (99.999%) and tungsten wire baskets were purchased

from Ted Pella, Inc. (Redding, CA). Silicon monoxide (SiO) with purity of 99.9% was purchased from GERAC (Milwaukee, WI).

3.3.2 Grating Construction

Two different gratings were used in this work. The first was a commercial holographic transmission grating with a 1000 nm pitch (Edmund Optics). The second was prepared from a commercial DVD-R and coated with a thin (~ 40 nm) layer of gold. Preparation of the metal-coated grating has been described previously (details in the Supporting Information).[7e] SiO films were formed on the gold grating via vacuum evaporation under conditions similar to gold coating (Supporting Information). Film thicknesses and composition were confirmed using atomic force microscopy (AFM) imaging, ellipsometry, and infrared reflection absorption spectroscopy (IRRAS) (details of methods in the Supporting Information).

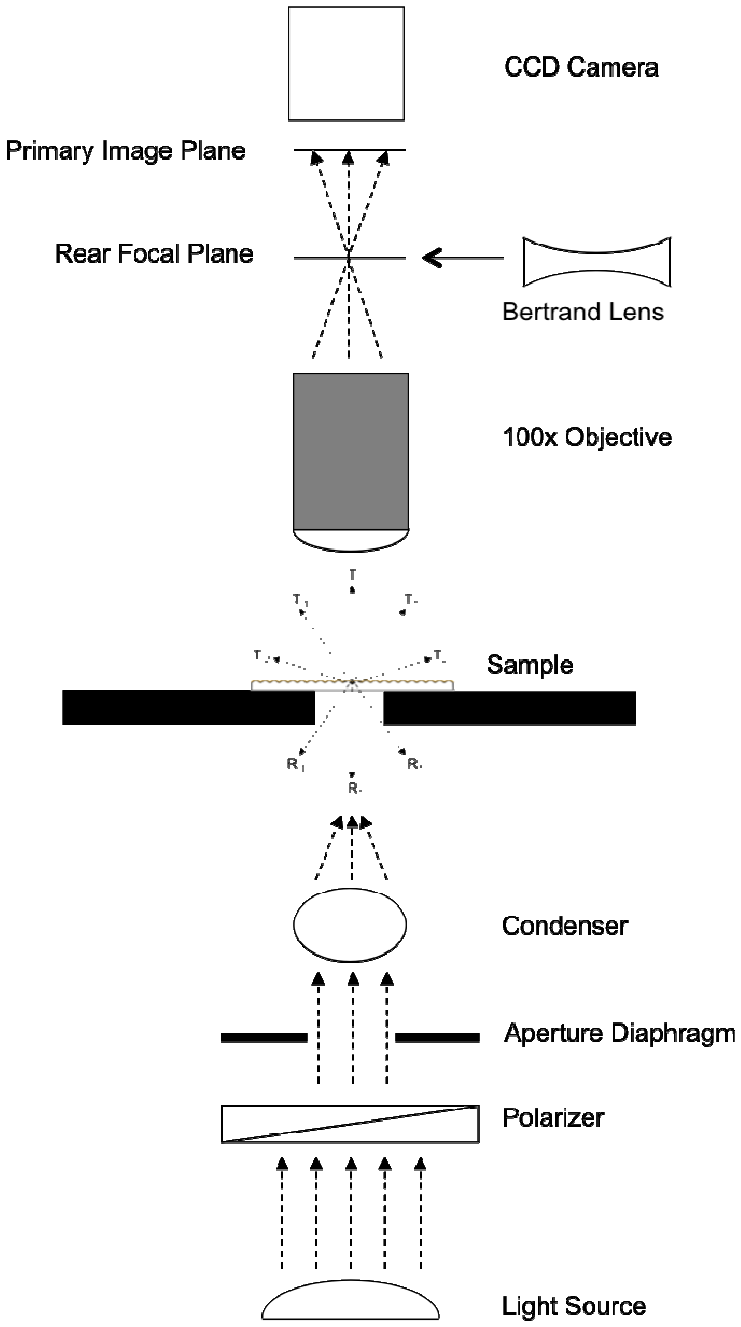

Scheme 1 Schematic of optical configuration used to measure surface plasmon resonance enhanced transmission through gold-coated grating associated with direct and diffracted light (reflected (R) and transmitted (T) orders) using an optical microscope. The Bertrand lens is inserted to focus the rear focal plane (diffraction image) onto a CCD camera.

3.3.3 Optical Characterization

Optical transmission measurements were performed using an optical microscope (Olympus model B41) in transmission mode with a broadband, white light source. A schematic of the optical train (Scheme 1) illustrates the major components. The light source consisted of a 150 W tungsten-halogen bulb with the standard infrared filter re- moved. Control of the incident light polarization (with respect to the grating direction) was achieved using a linear polarizer between the light source and the aperture diaphragm. Light was focused onto the sample using a condenser lens. The sample was mounted to a mechanical translation stage for xyz movement. A 100× microscope objective was used to focus the sample image into the observation tube. The microscope's detector consisted of either a CCD camera (Thorlabs) or a fiber-optic spectrometer (Ocean Optics). Collection of the sample's diffraction image was achieved by inserting a Bertrand lens into the observation tube. The Bertrand lens focuses the sample's Fourier image, which is located at the rear focal plane, onto the microscope's imaging plane to allow capture of optical diffraction data with the CCD detector. Subsequent data analysis was performed using ImageJ.

3.3.4 Optical Modeling

The optical response of the film-coated grating was modeled using the rigorously coupled wave analysis (RCWA) method. Details of the method and the form of its implementation used here can be found in several publications.15 Briefly, diffraction efficiencies were calculated for both transverse magnetic (TM) and transverse electric (TE) incident light as a function of wavelength. Calculations were performed using a custom-built code written in Matlab (further details in the Supporting Information). The grating geometry used in the model calculations was

based upon fitting experimental AFM measurements of the DVD-R profile (Supporting Information: Figure S.2). Upon the basis of these results, a sawtooth profile was used with a pitch of 670 nm and an amplitude of 120 nm. Refractive index values for the various materials included published values for gold[29] and SiO[30]. The polycarbonate substrate was modeled using the Sellmeier equation.[28]

3.4 Results and Discussion

An image of a holographic transmission grating, as observed through an optical microscope using a 100X objective, is shown in Figure 1A. The periodicity of the ridges in the image reflects the 1000 nm pitch of the grating. An image of the optical diffraction pattern from this grating can be observed by inserting a Bertrand lens into the microscope's observation tube.[13] A color version of the diffraction image (Figure 1B) exhibits three dominant features. A white, circular spot appears at the center of the image. This spot represents light that is directly transmitted through the sample, otherwise referred to as the zeroth-order spot. Two elliptical spots appear to the right and left of the central spot. These features are due to light that is diffracted by the grating and are associated with the +1 (right) and -1
(left) diffracted orders (Scheme 1). Although the zeroth-order peak appears white when
viewed by eye or as imaged with a color CCD camera, the plus/minus peaks disperse the light with blue light (shorter wavelengths) appearing nearest to the center and red light (longer wavelengths) appearing at the outer edges. The distances of the ± 1 diffracted spots from the zeroth-order spot are proportional to the reciprocal of the grating pitch. The 1000 nm pitch for this grating gives diffracted spots that are located at ± 1 μm^{-1}. Using the same magnification objective, a smaller grating pitch would produce ± 1 diffracted spots that are

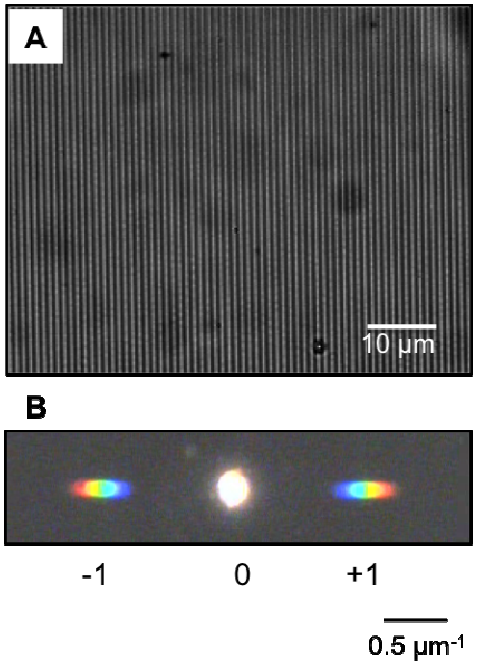

Figure 1 (A) Direct optical image and (B) diffraction image of uncoated transmission grating with 1000 µm pitch. Location of -1, 0 and +1 diffracted orders are identified in (B).

located further from the zeroth-order spot (due to a larger diffracted angle). The diffracted angle can be described by the grating equation,

$$\sin\theta_i + \sin\theta_m = m\lambda/\Lambda \qquad (1)$$

where θ_i is the angle of incidence, Λ is the grating pitch, λ is the wavelength, m is the diffracted order, and θm is the angle of the diffracted spot of order m. In a collinear mounting ($\theta_i = 0$), the position (L) of the diffracted spots on the diffraction image (Figure 1B) can be described by

$$L = D\left(m\lambda/\Lambda\right) \qquad (2)$$

where L is the measured distance from the zeroth-order spot, and D is a constant associated with the magnification level. Equation 2 shows that the location of the diffracted spots moves farther away from the zeroth-order spot with decreasing pitch and increasing diffracted orders. In addition, the location of the colors in the diffracted spot tracks with their wavelengths, with longer wavelengths appearing at larger distances from the origin. The dispersed light appearing in the ± 1-order spots in this diffraction image allows the spectral signature of a sample to be measured by simply determining the intensity as a function of position in the captured image. With proper calibration, the intensity versus pixel location in the image can be converted into intensity versus wavelength (vide infra).

To excite SPs at the gold/air interface, we chose to use a commercial DVD-R as the grating source. The DVD-R represents an inexpensive grating whose pitch (□670 nm) coincidentally has a value that is appropriate for exciting SPs in a thin metal film when using a collinear optical configuration ($\theta i = 0$).[7e] Thus, the DVD- R geometry is ideally suited for SP transmission (or reflection) measurements with an optical microscope.

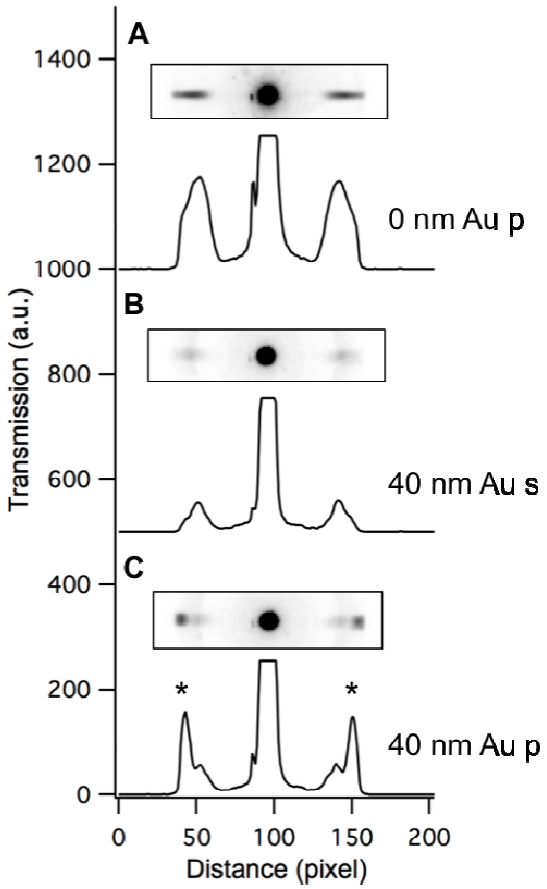

Figure 2 Optical diffraction images (insets) and transmitted intensity profiles for DVD grating: (A) uncoated grating p-polarized, (B) 40 nm Au-coated grating s-polarized, and (C) 40 nm Au-coated grating p-polarized. The SP peak is denoted by * in (C).

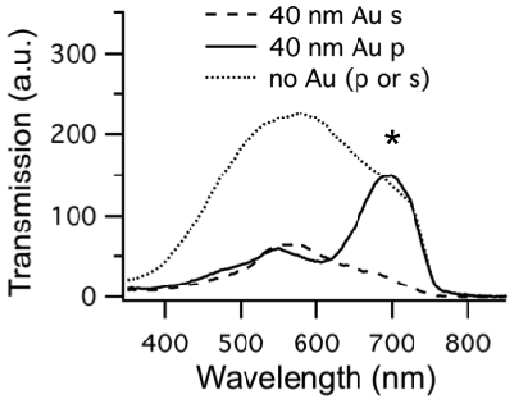

Figure 3 Transmission spectrum from +1 order diffracted peak for uncoated grating (dotted line), grating with 40 nm gold layer s polarized (dashed line) and grating with 40 nm gold layer p polarized (solid line). The SP peak is denoted by *.

The diffraction image of an uncoated DVD-R (Figure 2A) exhibits features similar to the transmission grating in Figure 1, with an intense zeroth-order peak at the image center and the ±1-order peaks to the left and right of the image center. A horizontal intensity profile along the center of the diffracted spots shows a large intensity for the zeroth-order peak and broad features for the ±1-order peaks. Notably, the diffraction image is independent of polarization (s or p) when exposed with direct ($\theta_i = 0$) illumination. Coating the grating with 40 nm of Au attenuates the transmitted light intensity and produces several new features as well as significant differences between s- and p-polarized light. The zeroth-order peak for s-polarized light is attenuated, and the ±1 diffracted peaks are substantially weaker, especially at longer wavelengths (Figure 2B). This is due to absorption from the thin, gold film. The response to p-polarized light shows a similar attenuation, but with an additional, strong transmission in the plus/minus first-order peaks at longer wavelengths (denoted by an asterisk in Figure 2C). This new transmission peak is due to excitation of a SP at the metal/air interface on the grating.[7e]

The data contained in the intensity profiles of the diffraction images can be readily converted into spectral data through the use of an appropriate calibration. We captured diffraction images using several interference filters possessing a narrow bandpass (10 nm) to convert pixel location into wavelength (Supporting Information Figure S3). Using the +1 diffracted peak, the resulting spectra for the three cases shown in Figure 2 are depicted in Figure 3. The uncoated DVD (dotted line) shows a broad intensity profile between □400 and 750 nm, which is consistent with the shape of light produced by the tungsten-halogen light source. The intensity of the light from the uncoated sample drops sharply at □780 nm, which is a result of the diffracted spot reaching the edge of the image window. This wavelength range can be extended to larger values by using a higher magnification objective (150 or 200 X). The spectra from the

Au-coated sample using s-polarized (dashed line) and p-polarized (solid line) light exhibit the expected features. The s-polarized spectrum is broad with a peak near 550 nm, consistent with a green transmitted color of a thin gold film. The p-polarized light tracks the s-polarized spectrum at small wavelengths, but then exhibits a very large transmission peak centered at □700 nm. This transmission peak is due to excitation of a SP at the gold/air interface.[7e] Notably, due to the asymmetric nature of this grating (air/gold/polycarbonate), a SP is also excited at the gold/ polycarbonate interface, but due to the higher refractive index of the polycarbonate substrate, this resonance is located in the near-infrared region (□1100 nm) and not observable in this data (vide infra).

A comparison of the experimental results with those derived from an optical simulation of the grating interface can be used to assist in data interpretation and to identify notable spectral features. The RCWA method was used to simulate the transmission and reflection of the various diffracted orders (Scheme 1) through a model grating (vide supra). Predicted transmission spectra were determined for TM and transverse electric TE light using the model grating profile with a 40 nm gold layer. Results for the zeroth- and first-order diffraction efficiencies are shown. For both TM_0 (p-polarized) and TE_0 (s-polarized) (Figure 4A), a peak is observed near 500 nm, as expected for a thin gold film. The TE_0 result shows no other notable features, whereas the TM_0 exhibits an intense enhancement near 700 nm, which is the result of SP excitation. Prior measurements of directly transmitted light through a gold-coated DVD-R showed spectra nearly identical in shape to what appears in Figure 4A (see Figure 3B in ref 7e). The predicted diffraction efficiencies for the +1-order

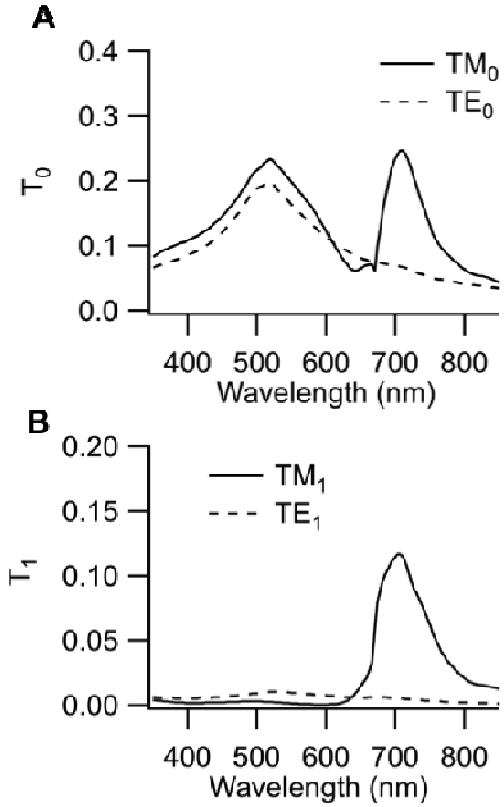

Figure 4 Calculated spectrum of transverse magnetic (TM, solid line) and transverse electric (TE, dashed line) light from 0^{th} order (A) and 1^{st} order (B) peaks for model grating having triangular profile with pitch of 670 nm, height of 120 nm, and gold thickness of 40 nm.

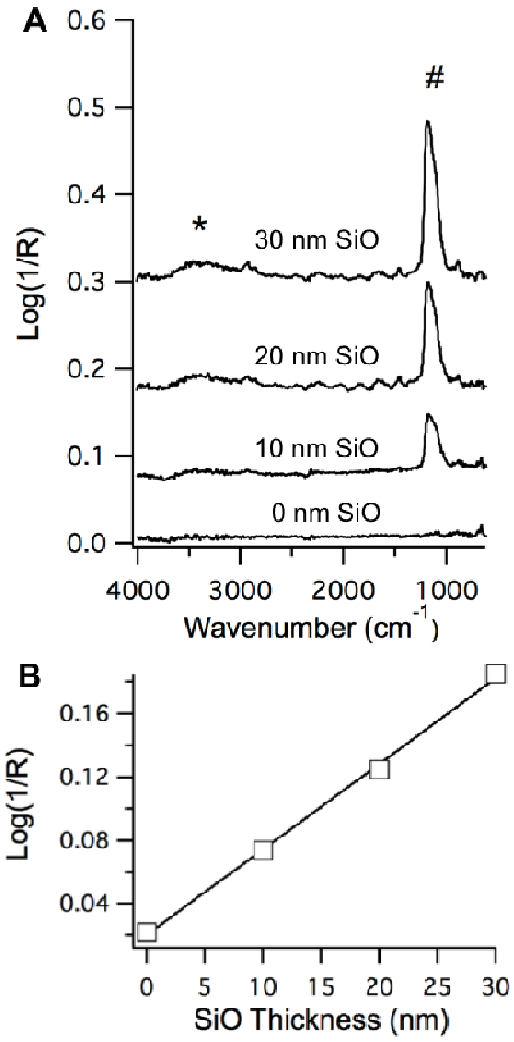

Figure 5 (A) IRRAS of SiO layers on gold-coated grating showing response for SiO film thicknesses of 0, 10, 20, and 30 nm. The major peaks identified in the figure are associated with the stretching vibrations of: # Si-O-Si and * Si-OH. (B) Plot of intensity of Si-O stretching peak (1100 cm^{-1}) versus film thickness.

peak (Figure 4B) are also consistent with the experimental results, with TE_1 showing only a broad peak near 500 nm and TM_1 exhibiting an intense SP peak near □700 nm. The primary difference between the model (Figure 4B) and experimental results (Figure 3) for the +1-order peak is that the experimental data shows more light transmission near 500 nm than the prediction. This could be due to minor differences in the grating shape, gold thickness, or limitations in the experimental optics, such as the nonlinearity of the light source. Nevertheless, the significant features (notably the presence of the SP peak) are consistent with both results.

To demonstrate the ability to track adsorption/film formation on the gold surface using these diffracted peaks, a series of SiO films were coated onto the grating. SiO was vapor-deposited onto the grating at thicknesses of 0, 10, 20, and 30 nm, as determined by a quartz crystal thickness monitor. The composition of the SiO films was confirmed using IRRAS. Features characteristic of the Si−O−Si stretching vibration (denoted by "#") were seen with a sharp peak at □1100 cm^{-1} that increased in magnitude with increasing film thickness (Figure 5A). In addition, a broad, although rather weak, signature associated with the OH stretch- ing vibration from Si−OH (denoted by an asterisk) is observed between 3000 and 3600 cm^{-1}.19 A plot of the intensity of the Si−O peak at 1100 cm^{-1} versus film thickness shows a clear, linear trend, which is consistent with a linearly increasing film thickness (Figure 5B).

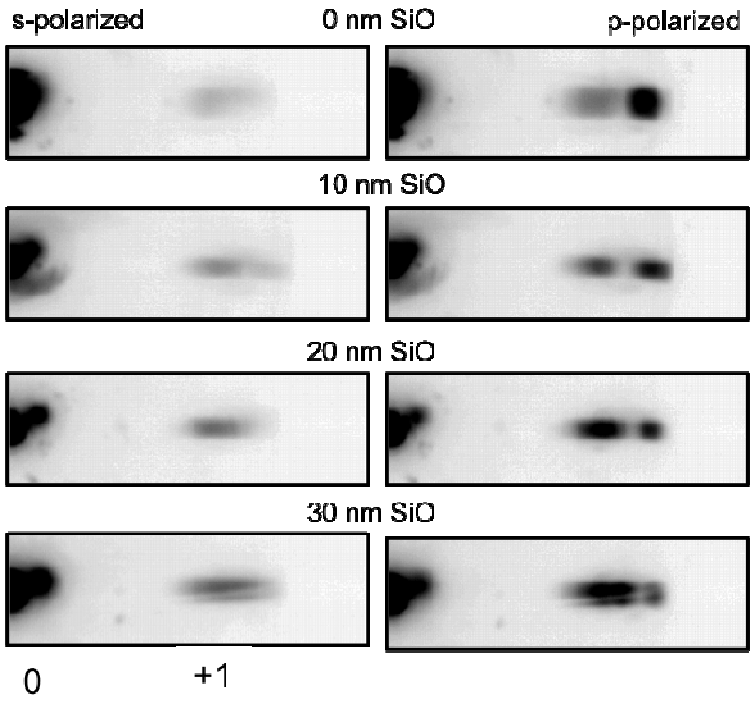

Figure 6 Diffraction images of gold-coated DVD grating using s-polarized (left) and p-polarized (right) light showing -1, 0 and +1 diffracted peaks with samples having SiO thicknesses of 0, 10, 20 and 30 nm.

The impact of the SiO films on the optical response of the gold-coated grating is

illustrated in Figure 6. A series of slices showing the right half of the diffraction images from each sample are shown. The images depict a portion of the diffraction image starting at the zeroth-order peak and including the complete +1-order peak. The -1 peak looks similar to the +1, but is not shown for clarity. The transmission depicted by the +1 peak for s-polarized light shows a broad, shallow band. With increasing SiO thickness, this band increases in intensity, but it remains fixed in position. In contrast, the p-polarized light shows two dominant features in the +1 peak. For the 0 nm SiO sample, the left portion of the +1 peak is a shallow, broad transmission peak similar to what is in the s data; however, the right portion of the +1 spot shows a large peak, which is associated with an enhanced trans- mission that is caused by the formation of a SP at the gold/air interface. With the deposition of a SiO film, the broad, lower-wavelength peak increases in magnitude in a fashion similar to the s-polarized result. In addition, the SPR peak is seen to both broaden slightly and shift to longer wavelengths as the SiO thickness increases from 0 to 10, 20, and 30 nm. In the 30 nm case, the plasmon peak has shifted nearly out of the field of view.

A quantitative view of the spectra associated with the +1 diffracted peaks in Figure 6 are depicted in Figure 7 after converting the intensity-versus-pixel location to transmittance-versus-wavelength. As was evident in the diffraction images, the s-polarized light displays a broad transmission peak centered around 500 nm (denoted as peak 1). With increasing film thick- ness, the magnitude of the transmission peak in this region increases. This increase in transmission can be most readily explained by considering the SiO film as an

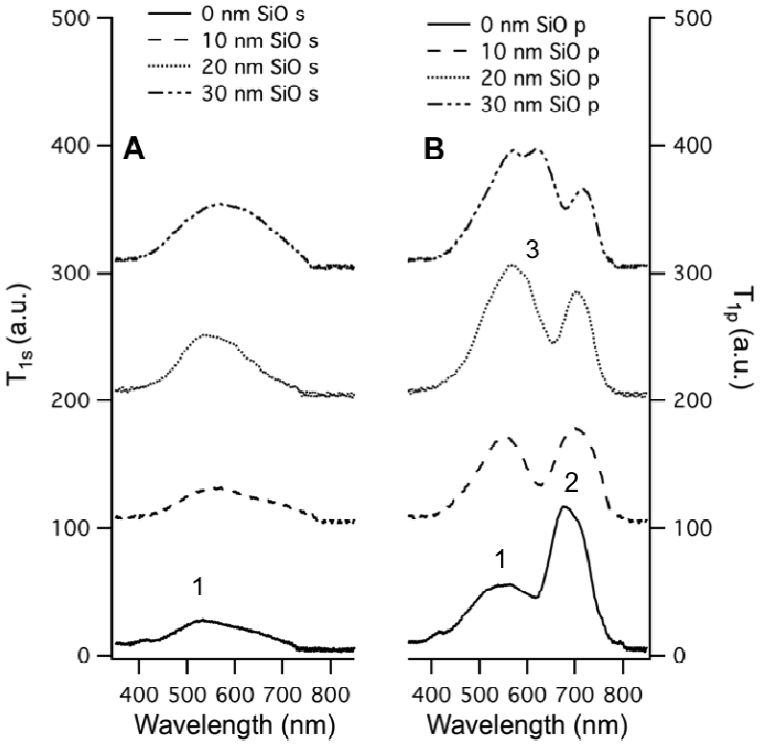

Figure 7 (A) p and (B) s-polarized transmission spectra from +1 order diffraction peak for gold-coated diffraction grating at SiO thicknesses of 0 (solid line), 10 (dashed line), 20 (dotted line), and 30 (dash double-dot) nm.

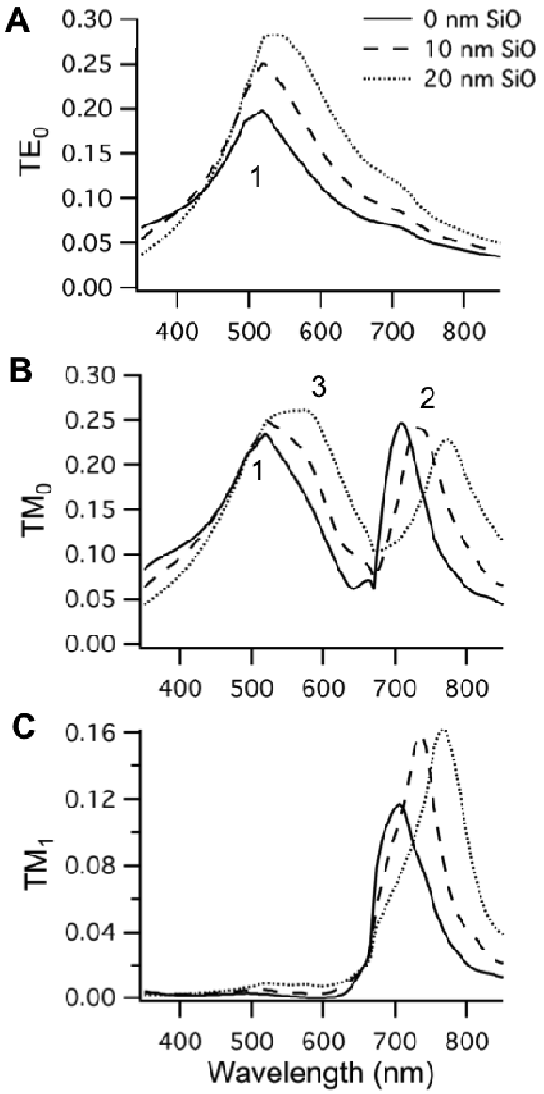

Figure 8 Calculated transmission spectra for model diffraction grating having SiO film thicknesses of 0 (solid line), 10 (dashed line) and 20 (dotted line) nm: (A) $TE_0 = 0^{th}$ order transverse electric (s-polarized), (B) $TM_0 = 0^{th}$ order transverse magnetic (p-polarized), (C) $TM_1 = 1^{th}$ order transverse magnetic (p-polarized). The peaks identified by 1, 2, and 3 are discussed in the text.

antireflective coating. The presence of the SiO film on the gold surface reduces reflection at that surface, which serves to increase the amount of light that is transmitted through and, subsequently, measured at the detector. The spectra determined for the p-polarized trans- mission also show an increase in the light transmitted at smaller wavelengths (peak 1), which is also a result of this antireflective effect. In addition, the spectrum for p-polarized light clearly shows the strong enhanced transmission peak due to SP reso- nance at □700 nm (peak 2) for the 0 nm SiO sample. The 10 nm SiO sample shows a slight attenuation and broadening of the SPR transmission peak and a red shift of the peak position. The peak magnitude continues to decrease, and the peak position red shifts for the 20 and 30 nm films, although the longer wavelength region of both peaks is truncated by the edge of the image win- dow (vide supra). Thus, the SPR peak red-shifts with increasing film thickness, just as would be expected. An additional feature also appears for the 20 and 30 nm SiO films. Peak 3 appears as a shoulder on peak 1 for the 20 nm film and then becomes more clear for the 30 nm film. This additional peak is also a SP peak, although one originating from a second-order diffracted peak on the back side of the grating (the gold/polycarbonate interface).

The sensitivity of this diffraction-based approach for SPR detection of film thickness is consistent with other grating-based SPR detection methods. A quantitative comparison of the peak shifts in the experimental data show a sensitivity of □1.4 nm peak shift/nm film thickness for the thinnest SiO layers and an increasing sensitivity to nearly 5 nm peak shift/nm film thickness for the 30 nm film (Figure S4, Supporting Information). This in- crease in sensitivity (S) is a direct function of the fact that peak shifts for grating-based SPR sensing are proportional to the wave- length ($S \propto \lambda_{peak}$), at which the peaks appear. Thus, longer-wavelength peak positions have a greater sensitivity and give a larger wavelength shift for an equivalent change in

refractive index. Details of these sensitivity calculations as well as comparison of various SPR-based sensing methods have been previously described.[7f,11c]

Figure 8 depicts simulation results for the model DVD grating with SiO films of several different thicknesses. The directly transmitted light associated with s-polarized light (transverse electric, zeroth order: TE_0) is shown in Figure 8A. The simulation results are consistent with those obtained experimentally. A broad peak is observed with a maximum near 500 nm (peak 1). Increasing the thickness of the SiO layer in the model system results in an increase in transmission. Again, this increase can be attributed to an antireflective effect associated with the SiO layer, which increases the transmitted light.

The predicted transmission with p-polarized light (transverse magnetic zeroth order: TM0) in Figure 8B exhibits two dominant peaks in the absence of a SiO film. The peak at 1 was just described, and a second peak appears at □700 nm (peak 2). Peak 2 is an enhanced transmission peak that is due to the excitation of a SP at the gold/air interface. The location of this peak can be readily calculated by considering the momentum matching condition between the wavevector of the SP (k_{sp}) with that of the incident p-polarized light interacting with the diffraction grating (k_{gr}), as given in eq 3

$$k_{sp} = \frac{2\pi}{\lambda_0}\sqrt{\frac{\varepsilon_M^{'}\varepsilon_D}{\varepsilon_M^{'}+\varepsilon_D}} = \frac{2\pi}{\lambda_0}\sqrt{\varepsilon_D}\sin\theta_0 + m\frac{2\pi}{\Lambda} = k_{gr} \qquad (3)$$

where ε'_m is the real part of the metal's dielectric constant, and ε_D is the dielectric constant of the neighboring material (air or polycarbonate). At an incident angle of $\theta = 0°$, this equality may be satisfied by several different conditions. With a grating pitch of $\Lambda = 670$ nm, for example, the first diffracted order ($m = 1$) will satisfy this momentum matching condition at a gold (ε'_m)/air (ε_D) interface at λ_{sp} □ 687 nm. As a plasmon peak at the gold/air interface, its location is

impacted by the local dielectric conditions existing at that interface. The presence of a thin film will cause this peak to red shift due to the increasing dielectric constant associated with that layer (increasing effective ε_D). Indeed, the calculation supports this red shift in the position of peak 2 after the addition of a thin film represented by 10 and 20 nm SiO layers. The calculated shift in peak position is □1.4 nm wavelength shift per nanometer of film at small film thicknesses and increases to almost 6 nm peak shift per nanometer film thickness for the 30 nm film, which is consistent with expectations.[11c]

With the 20 nm SiO film, a third peak emerges (peak 3) in the calculation and appears as a shoulder on peak 1. This is also a SP, but it is associated with the gold/polycarbonate interface at the back side of the DVD grating. The position of this peak can be found by solving eq 3 using the gold/polycarbonate dielectric constants (ε_D □ 2.5) and m = 2, to give λ_{sp} □ 581 nm. Another SP is excited at the gold/polycarbonate interface that is associated with the m = ±1 or first diffracted orders. However, this peak appears at □1100 nm, so it is at higher wavelengths than what is measured in this work.

The predicted values for the first-order diffracted peak behave in a manner consistent with what was seen with the experimental results in that the SP peaks also red shift with increasing film thickness. Figure 8C plots the diffraction efficiency for the first- order diffracted peak for transverse magnetic illumination (TM_1). An intense peak appears at □700 nm, and this peak shifts toward longer wavelengths with the addition of thicker SiO films. Notably, a direct comparison between the peak positions and peak shifts as observed experimentally (see Figure S4 of the Supporting Information) show that both the data and modeling results exhibit a similar peak position and peak shifts for increasing film thicknesses.

It should be noted that the SPs that exist at the back side (gold/polycarbonate) of the

grating sense little of what occurs at the front side (gold/air) of the grating, since the decay length of the SP within the gold is □25 nm under these conditions. More extensive analysis of the modeling results allows one to compare the behavior of peaks appearing at both the back and front side of the grating, and indeed, they are related. In fact, the appearance of SPs at one side of the grating can often be traced to the passing off of an order from the other side of the grating, which creates an evanescent wave and thus excites a SP. Although this behavior indicates that SPs form at several different conditions at the front and back side of the grating, because of the short SP decay lengths within the gold film, only those at the gold/air interface show a significant response to thickness changes in a thin film forming at the front side of the grating. More importantly, the peaks from the gold/air interface are the dominant features in both the experimental and simulated spectra.

3.5 Conclusion

Grating-based coupling strategies for surface plasmon reso- nance sensing represent a simple, yet highly sensitive, method for tracking adsorption and thin film formation. In this work, we have demonstrated how film formation on a grating based upon a commercial DVD-R can be monitored using a simple optical microscope setup. In fact, the ability to use a Bertrand lens to image the diffracted spots associated with the grating allows one to monitor the transmission peaks associated with SPs at the grating directly with a CCD camera and avoid the use of a spec- trometer or monochromator. A comparison of the direct and diffracted transmission data with predicted results as obtained by the RCWA shows a consistency in the behavior of the various peaks and also allows one to identify the origins of the peaks with respect

to the various reflected and transmitted diffracted orders at the back and front sides of the metal surface.

3.6 Acknowledgement

This work was funded by the National Science Foundation (CHE 0809509), the National Institutes of Health (R44 RR023763- 02), and the W. M. Keck Foundation through the W. M. Keck Laboratory for High Throughput Atom-Scale Analysis at Iowa State University.

3.7 Supporting Information

3.7.1 Grating Construction

Two different gratings were used in this work. The first was a commercial holographic transmission grating with a 1000 nm pitch (Edmund Optics). The second was a metal-coated grating prepared from a commercial DVD-R. Grating preparation involved manually splitting the DVD-R into two pieces (Fig.S.1) at the center-plane using a razor blade. The dye layer was removed by rinsing in ethanol, while the silver layer was removed by soaking in concentrated nitric acid. The grating was then thoroughly rinsed with deionized water, dried under nitrogen, and placed in a vacuum chamber for film coating (Denton Vacuum Turbo III, Morrestown, NJ). Gold films of ~40 nm thickness were deposited onto the gratings at a rate of 1–2 A□ s–1 and a pressure of 7×10–5 Torr under nitrogen atmosphere. The thickness was monitored using a quartz crystal thickness gauge. SiO films were also

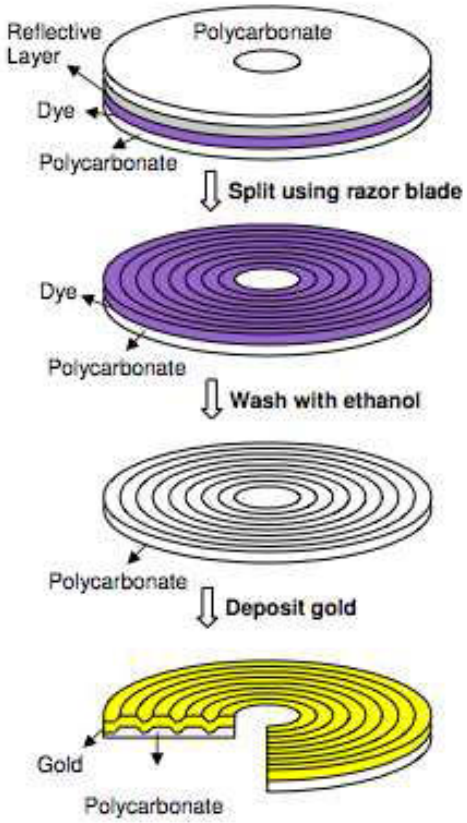

Figure S 1 Schematic showing construction of gold gratings from commercial DVD-R

formed via vacuum evaporation under conditions similar to gold coating. Film thicknesses and compositions were confirmed using atomic force microscopy (AFM) imaging, ellipsometry, and infrared reflectance absoption spectroscopy (IRRAS).

3.7.2 Atomic Force Microscope (AFM) Imaging.

AFM imaging of the sample surfaces was performed with a Dimension 3100 scanning probe microscope and a Nanoscope IV controller (Veeco Metrology, LLC, Santa Barbara, CA). Imaging was performed in tapping mode using silicon TESP7 AFM tips (Veeco Metrology, LLC, Santa Barbara, CA) with a spring constant of ~70 N m–1 and a resonance frequency of ~280 kHz.

3.7.3 Ellipsometry

Film thicknesses were confirmed using ellipsometry. A motorized variable- angle null ellipsometer (Multiskop, Optrel GbR) operating as a rotating analyzer ellipsometer (RAE) in the polarizer-sample-analyzer (PSA) configuration utilizing a broadband light source at 70° angle of incidence was used to measure the ellipsometric parameters Δ and Ψ. The values of Δ and Ψ were converted into equivalent optical thicknesses using a n-layer model. The optical constants of the gold substrate (refractive index *n* and the absorption coefficient *k)* were first determined using a two-phase model (air/substrate). The thickness of the adsorbed films were then found using a three-phase model (air/film/substrate).

3.7.4 Infrared Reflection Absorption Spectroscopy (IRRAS)

A Fourier transform infrared spectrometer (Nicolet Magna 750, Thermo Scientific) using a liquid nitrogen-cooled MCT detector was used to obtain infrared spectra. Reflectance spectra

were collected using a specular reflectance accessory (VeeMax, Pike Technologies) and a ZnSe polarizer using p-polarized light incident at 80o with respect to the surface normal. These spectra are presented as log(1/R), where R is the sample reflectance divided by a reference surface. Each spectrum represents an average of 512 individual sample and reference scans acquired at 2 cm-1 resolution. A freshly prepared, gold coated, glass slide served as the reference sample.

3.7.5 Optical Modeling

Rigorously coupled wave analysis (RCWA) algorithm is used to simulate experimetal results with defined parameters which are equivalent to experiment conditions. In brief, RCWA calculates both TE and TM incident light which pass through a defined gold-coated grating and expresses the results in terms of transmission efficiency versus wavelength. The scope of simulation covers 0 order transmission and +1 order diffraction with approximate defined grating profile. Simulations are performed in Matlab environment with a custom-built m. file.

RCWA requires a defined grating to calculate transmission, absorption, and reflection. To achieve this, the AFM image of DVD grating was fit and yields a defined profile shown in Figure S.2. The profile was sliced to a series of layer with defined effective index by a Fourier expansion of the refractive index with a particular geometry for each layer. With proper boundary conditions between sliced layer, Frensal's equations are imposed to calculate transmission and reflection coefficients for each layer. Thus, for all diffraction orders, corresponding transmission, diffraction, and reflection ratio can be reproduced. In order for simulation to converge, the Fourier expansion for the refractive index values within the grating layers were described by 42 terms for TE polarization (± 21 diffracted orders) and 122 terms for TM polarization ±61 diffracted orders).

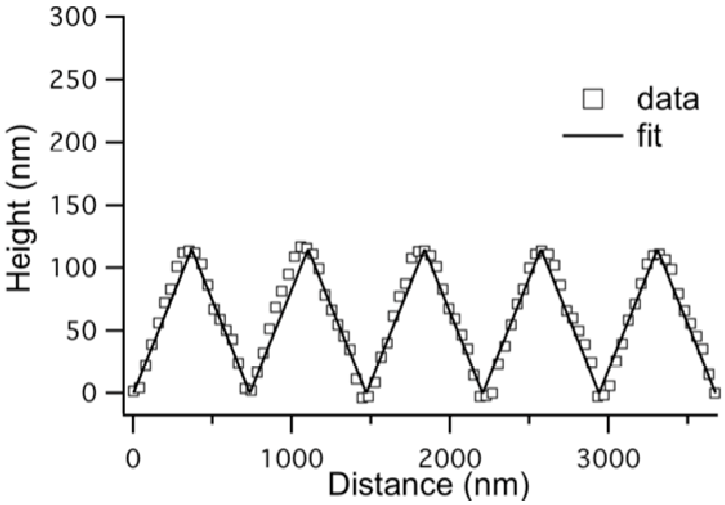

Figure S 2. AFM profile of line scan and profile fit. The pitch is 670 nm and amplitude is 120 nm.

3.8 References

1. (a) Y. Xia, N. J. Halas, *MRS Bull.* 2005, *30*. 338-343; (b) W. L. Barnes, A. Dereux, T. W. Ebbesen, *Nature* 2003, *424*. 824-830.
2. T. W. Ebbesen, H. J. Lezec, H. F. Ghaemi, R. Thio, P. A. Wolff, *Nature* 1998, *391*. 667-669.
3. (a) M. E. Stewart, C. R. Anderton, L. B. Thompson, J. Maria, S. K. Gray, J. A. Rogers, R. G. Nuzzo, *Chem. Rev.* 2008, *108*. 494-521; (b) J. Homola, *Chem. Rev.* 2008, *108*. 462-493; (c) A. J. Haes, C. L. Haynes, A. D. McFarland, G. C. Schatz, R. P. Van Duyne, S. Zou, *MRS Bull.* 2005, *30*. 368-375; (d) J. Homola, *Anal. and Bioanal. Chem.* 2003, *377*. 528-539.
4. (a) A. G. Brolo, R. Gordon, B. Leathem, K. L. Kavanagh, *Langmuir* 2004, *20*. 4813-4815; (b) S. M. Williams, K. R. Rodrigues, S. Teeters-Kennedy, A. D. Stafford, S. R. Bishop, U. K. Lincoln, J. V. Coe, *J. Phys. Chem. B* 2004, *108*. 11833-11837.
5. T. Rindzevicius, Y. Alaverdyan, A. Dahlin, F. Hook, D. S. Sutherland, M. Kall, *Nano Lett.* 2005, *5*. 2335-2339.
6. Y. S. Jung, Z. Sun, J. Wuenschell, H. K. Kim, P. Kaur, L. Wang, D. Waldeck, *App. Phys. Lett.* 2006, *88*.
7. (a) F. Yu, S. J. Tian, D. F. Yao, W. Knoll, *Anal. Chem.* 2004, *76*. 3530-3535; (b) S. J. Tian, N. R. Armstrong, W. Knoll, *Langmuir* 2005, *21*. 4656-4660; (c) B. K. Singh, A. C. Hillier, *Anal. Chem.* 2006, *78*. 2009-2018; (d) P. Adam, J. Dostalek, J. Homola, *Sens. and Act. B* 2006, *113*. 774-781; (e) B. K. Singh, A. C. Hillier, *Anal. Chem.* 2008, *80*. 3803-3810; (f) J. Homola, I. Koudela, S. S. Yee, *Sens. and Act. B* 1999, *54*. 16-24; (g) C. J. Alleyne, A. G. Kirk, R. C. McPhedran, N. A. P. Nicorovici, D. Maystre, *Optics Express*

2007, *15*. 8163-8169; (h) J. Dostalek, J. Homola, *Sensors and Actuators B-Chemical* 2008, *129*. 303-310; (i) R. C. Bailey, J.-M. Nam, C. A. Mirkin, J. T. Hupp, *Journal of the American Chemical Society* 2003, *125*. 13541-13547; (j) H. J. Lee, A. W. Wark, R. M. Corn, *Analyst* 2008, *133*. 596-601.

8. (a) H. J. Lezec, A. Degiron, E. Devaux, R. A. Linke, L. Martin-Moreno, F. J. Garcia-Vidal, T. W. Ebbesen, *Science* 2002, *297*. 820-822; (b) P. R. H. Stark, A. E. Halleck, D. N. Larson, *Methods* 2005, *37*. 37-47; (c) A. J. Haes, R. R. Van Duyne, *J. Amer. Chem. Soc.* 2002, *124*. 10596-10604; (d) C. L. Haynes, R. R. Van Duyne, *J. Phys. Chem. B* 2001, *105*. 5599; (e) J. Prikulis, P. Hanarp, L. Olofsson, D. S. Sutherland, M. Kaell, *Nano. Lett.* 2004, *4*. 1003; (f) Y. Xia, G. M. Whitesides, *Ann. Rev. Mater. Sci.* 1998, *28*. 153.

9. J. Homola *Surface Plasmon Resonance Based Sensors*; Springer Series on Chemical Sensors and Biosensors Springer-Verlag: Berlin-Heidelberg-New York, 2006.

10. J. Dostalek, J. Homola, M. Miler, *Sens. and Act. B* 2005, *107*. 154-161.

11. (a) N. Zhang, R. Schweiss, Y. Zong, W. Knoll, *Electrochim. Acta* 2006, *52*. 2869-2875; (b) S. C. Kitson, W. L. Barnes, G. W. Bradberry, J. R. Sambles, *J. Appl. Phys.* 1996, *79*. 7383-7385; (c) W.-H. Yeh, J. Kleingartner, A. C. Hillier, *Analytical Chemistry* 2010, *82*. 4988-4993.

12. D. Nazarova, B. Mednikarov, P. Sharlandjiev, *Applied Optics* 2007, *46*. 8250-8255.

13. L. V. Kondrachova, R. A. May, C. W. Cone, D. A. V. Bout, K. J. Stevenson, *Langmuir* 2009, *25*. 2508-2518.

14. M. D. Abramoff, P. J. Magelhaes, S. J. Ram, *Biophotonics International* 2004, *11*. 36-42.

15. (a) P. Lalanne, G. M. Morris, *J. Opt. Soc. Am. A.* 1996, *13*. 779-784; (b) M. G. Moharam, E. B. Grann, D. A. Pommet, T. K. Gaylord, *J. Opt. Soc. Am. A.* 1995, *12*. 1068-1076; (c) M. G. Moharam, D. A. Pommet, E. B. Grann, T. K. Gaylord, *J. Opt. Soc. Am. A.* 1995, *12*. 1077-1086.

16. P. B. Johnson, R. W. Christy, *Phys. Rev. B* 1972, *6*. 4370-4379.

17. G. Hass, C. D. Salzberg, *J. Opt. Soc. Am.* 1954, *44*. 181-187.

18. S. N. Kasarova, N. G. Sultanova, C. D. Ivanov, I. D. Nikolov, *Optical Materials* 2007, *28*. 1481-1490.

19. (a) H. Tada, *Langmuir* 1995, *11*. 3281-3284; (b) M. Klevenz, S. Wetzel, M. Trieloff, H.-P. Gail, A. Pucci, *Phys. Status Solidi B* 2010, *247*. 2179-2184.

CHAPTER 4 RESONANCE QUENCHING AND GUIDED MODES ARISING FROM THE COUPLING OF SURFACE PLASMONS WITH A MOLECCULAR RESONANCE

Analytical Chemistry, **84** 1139-1145 (2012)

Wei-Hsun Yeh, Joe W. Peptefish, Andrew C. Hillier

4.1 Abstract

In this report, we describe experimental and modeling results that illucidate the nature of coupling between surface plasmon polaritons in a thin silver film with the molecular resonance of a zinc phthalocyanine dye film. This coupling leads to several phenomena not generally observed when plasmons are coupled to transparent materials. The increased absorption coefficient near a molecular resonance leads to a discontinuity in the refractive index, which causes branching of the plasmon resonance condition and the appearance of two peaks in the p-polarized reflectance spectrum. A gap exists between these peaks in the region of the spectrum associated with the molecular resonance, and reflects quenching of the plasmon wave due to violation of the resonance condition. A second observation is the appearance of a peak in the s-polarized reflection spectra. The initial position of this peak corresponds to where the refractive index of the adsorbate achieves its largest value, which occurs at wavelengths just slightly larger than the maximum in the molecular resonance. Although this peak initially appears to be nondispersive, both experimental data and optical modeling indicate that increasing the film thickness shifts the peak position to longer wavelengths, which implies that this peak is not associated with the molecular resonance but, rather, is dispersive in nature. Indeed, modeling shows that this peak is due to a guided mode in the film, which appears in these conditions due to

the abnormally high refractive index of the film near the absorbance maximum. Results also show that, with increasing film thickness, numerous additional guided modes appear and move throughout the visible spectrum for both s and p-polarized light. Notably, these guided modes are also quenched near the location of the molecular resonance. The quenching of both the plasmon resonance and the guided modes can be explained by a large decrease in the in-plane wave propagation length that occurs near the molecular resonance, which is a direct result of the film's large absorption coefficient.

4.2 Introduction

The resonance conditions of surface plasmons (SPs) at a metal-dielectric interface are highly sensitive to the local environment. This behavior has led to their extensive use in thin film and adsorption sensing.[1-3] The majority of these applications have involved measurements with transparent films or adsorbates possessing a negligible optical absorption coefficient. Changes in the resonance condition in response to a simple dielectric material can be readily explained in terms of the metal's refractive index and the optical thickness of the dielectric layer.[4] In the presence of a film with a larger dielectric constant than the surroundings, the increased optical density results in a decrease in the energy associated with the SP resonance and a corresponding red-shift in the resonance position.

For adsorbates possessing a molecular resonance, the coupling with SPs is much more complex and also information rich. The complexity of this coupling has been demonstrated with propagating SPPs (or surface plasmon polaritons) in thin metal films. Early studies with SPPs showed that the coupling of Langmuir-Blodgett dye assemblies using attenuated total reflection on thin silver films lead to branching of the dispersion curves near the molecular

resonance.[5-7] Notably, studies of SPP-adsorbate interactions benefit from the ability to directly measure dispersion relations via simple angle and wavelength scanning. A number of studies involving the coupling of SPPs with J-aggregates and other absorbing materials have been published.[8-10] In analytical applications, the interaction of SPPs and molecular adsorbates has led to various advanced forms of surface plasmon spectroscopy.[11,12] Examples of these advancements include spectral fingerprinting,[13] enhancements in sensitivity for SPR thickness shifts[14,15] and signal enhancement for absorbance detection.[16]

The interaction of molecular resonances with localized surface plasmon resonance (LSPR) at nanoparticles has received increasing attention.[17] Details of the interaction between a molecular resonance and the LSPR at nanoparticles is strongly influenced by the size (and shape) of the nanoparticle, as well as the degree of overlap between the LSPR and the molecular resonance.[18] Indeed, the coupling leads not only to variation in the magnitude of the LSPR shifts, but also to resonance quenching, which has been exploited for detection methods such as plasmon resonance energy transfer.[19,20] In addition to the ability to exploit plasmon-molecule interactions to improve the efficiency of photochemical and photoelectrochemical processes,[21] molecule-plasmon coupling can be used to perform active optical switching.[22,23] A merging of local and extended surface plasmon coupling with molecular resonances, via ordered arrays of nanostructures, can potentially lead to even greater flexibility and control of SP-molecule coupling and the resulting phenomena.[24,25]

In order to more fully understand the interaction between a molecular resonance in an adsorbed material and an SP in a metal film, we describe the results of a series of experiments and optical modeling studies that demonstrate the coupling between propagating SPPs in a thin silver film and the molecular resonance associated with thin films of a zinc

phthalocyanine (ZnPC) dye. The optical reflection of thin films of ZnPC on silver is examined in the Krestchmann configuration as a function of wavelength and angle of incidence. The well-defined SP resonance on a bare silver film red-shifts in the presence of a thin ZnPC film. With increasing thickness, the SP resonance overlaps with the Q-band of the ZnPC film. In the region of the spectrum where the ZnPC Q-band absorbance lies, the SP resonance is quenched, and the SP is split into a low and high energy state, evidenced by the appearance of two separate peaks in the reflectance of p-polarized light. Under these same conditions, an additional peak appears in the s-polarized spectrum. Optical modeling is used to verify the origins of this SP resonance quenching and also to assist in interpreting this new peak, which is the consequence of a guided wave in the dye film and not directly related to the molecular resonance. Also, the presence of the molecular resonance leads to quenching of both plasmon and guided modes within the spectral region associated with the large optical absorbance in the film as a result of the decreased propagation length of the plasmon wave.

4.3 Experimental Section

4.3.1 Materials and Reagents

ZnPC, hydrogen peroxide solution (30%), and sulfuric acid were purchased from Sigma-Aldrich (St. Louis, MO). Glass slides were purchased from Fisher Scientific (Pittsburgh, PA). Index matching fluid and BK7 prisms were purchased from Edmund Optics (Barrington, NJ). Silver (99.999%), tungsten wire baskets, and alumina-coated tungsten evaporation baskets were purchased from Ted Pella, Inc. (Redding, CA). Deionized water with electrical resistivity greater than 18 MΩ·cm was used during the rinsing and cleaning procedures (NANOPure, Barnstead, Dubuque, IA).

4.3.2 Sample Preparation

Metal and dye films were deposited using thermal evaporation onto planar glass slides. Fresh piranha solution (mixture of 3:1 concentrated sulfuric acid to 30% hydrogen peroxide solution) was used to clean the glass slides. Caution: piranha solution reacts violently with organic compounds! Following the cleaning, the glass slides were rinsed vigorously with deionized water and dried under nitrogen. The slides were subsequently placed in a vacuum chamber (model Bench Top Turbo III, Denton Vacuum, Moorestown, NJ) for deposition of □45 nm of silver by resistive heating from a tungsten wire basket at a rate of 1 A□ s^{-1} and a pressure of $<10^{-5}$ Torr. The Ag-coated slides were then immediately transferred to a second vacuum chamber (model DV502A, 1 Denton Vacuum). Thin films of ZnPC were slowly (<0.1 A□ s^{-1}) deposited on Ag-coated slides under a pressure of $<10^{-5}$ Torr from alumina-coated tungsten evaporation baskets.

4.3.3 Atomic Force Microscopy (AFM) Imaging

AFM imaging of the sample surfaces was performed with a Dimension 3100 scanning probe microscope and a Nanoscope IV controller (Veeco Metrology, LLC, Santa Barbara, CA). Imaging was performed in tapping mode using silicon TESP7 AFM tips (Veeco Metrology) with a spring constant of □70 N m^{-1} and a resonance frequency of □280 kHz. Film thicknesses were determined by using a razor blade to remove a region of film, and a line profile across this boundary was used to determine the height difference between the substrate and film.

4.3.4 Surface Plasmon Resonance Reflection Measurements

A computer-controlled variable-angle ellipsometer (Multiskop, Optrel GbR, Sinzing, Germany) was modified to perform broad-band reflection measurements by removing the compensator, replacing the He−Ne laser with a fiber-coupled, broad-band, tungsten−halogen

light source (OSL1, Thor Lab, Newton, NJ), and mounting an optical fiber spectrophotometer (HR4000CG-UV-NIR, Ocean Optics, Inc., Dunedin, FL) as the detector. Control of the angle of incidence was achieved with the instrument's motorized two-circle goniometer. Reflection measurements were performed in the Kretschmann configuration, with metal-coated glass slides attached to a 45° BK7 prism using index matching fluid. Reflectance values are reported in terms of p-polarized (Rp) or s-polarized (Rs) reflectance, which is calculated by dividing the reflected light intensity (p or s) by the s-polarized reflectance from an uncoated silver (47 nm) surface at the same angle of incidence (θ).

4.3.5 Spectroscopic Ellipsometry

Rotating analyzer ellipsometry (RAE) was performed in the polarizer−sample−analyzer (PSA) configuration using the optical system described above. Light from a tungsten−halogen light source was polarized at 45° and reflected by the sample surface at an incident angle of 70°. The analyzer was rotated from 0° to 180°, and a fiber-optic spectrometer was used to capture spectra of reflected intensities at 5° intervals. The measured intensity spectra were numerically integrated over the range of analyzer angles to obtain the ellipsometry parameters Δ and Ψ between 400 and 1000 nm. The values of Δ and Ψ were then converted into equivalent optical thicknesses using an N-phase model (vide infra). The optical constants of the silver substrate (refractive index n and absorption coefficient κ) were first determined using a three- phase model (air/silver/BK7) with the AFM-measured silver thickness (47 nm). The optical constants of the ZnPC films were then found by fitting a four-layer model (air/ZnPC film/ silver/BK7) using the AFM-measured thicknesses for the Ag (47 nm) and ZnPC (19 nm).

4.3.6 Optical Modeling

N-phase Fresnel calculations were used to model reflection and transmission through the multilayer air/ZnPC/silver/BK7 prism system as a function of the wavelength, angle of incidence, and polarization state of the incident light.[22] Scripts were written in MATLAB (The MathWorks, Inc., Natick, MA) to calculate reflection for three-phase (BK7/silver/air) or four-phase (BK7/silver/ZnPC film/air) models. Wavelength-dependent refractive indices of BK7 glass were used in the calculations. The dispersion of BK7 glass was estimated using the Sellmeier equation:

$$n^2(\lambda) = 1 + \frac{B_1\lambda^2}{\lambda^2 - C_1} + \frac{B_2\lambda^2}{\lambda^2 - C_2} + \frac{B_3\lambda^2}{\lambda^2 - C_3} \qquad (1)$$

where n is the refractive index of BK7, λ is the wavelength of light (μm), and the values of the constants were taken from Schott glass: B1 = 1.03961212, B2 = 2.31792344 × 10−1, B3 = 1.01046945, C1 = 6.00069867 × 10−3 μm2, C2 = 2.00179144 × 10−2 μm2, C3 = 1.03560653 × 102 μm2. The refractive index values for silver (Figure S3, Supporting Information) and ZnPC (Figure S4, Supporting Information) were derived from fitting the experimental spectroscopic ellipsometry results (Figure S2, Supporting Information) from the experimentally prepared thin films.

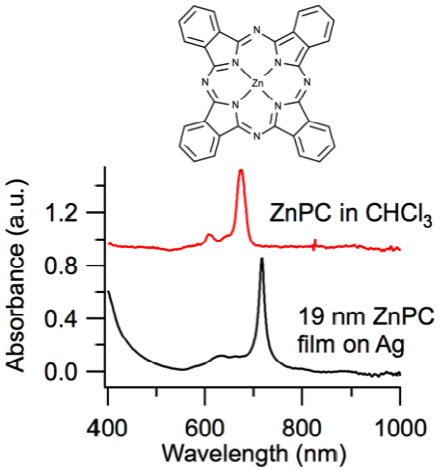

Figure 1 Absorbance spectra of ZnPC in solution (50 μm in $CHCl_3$) and as 19 nm film on Ag-coated (47 nm) glass.

4.4 Results and Discussion

Organic dyes such as zinc phthalocyanine (ZnPC) have generated considerable interest due to their large molar absorptivities and potential use as artificial pigments and in applications such as memory storage, catalysis, and optoelectronics.[27] In solution, ZnPC exhibits a strong molecular resonance near 680 nm associated with the dye's Q-band (Fig.1). When formed as a thermally evaporated thin film on silver, there is a slight red-shift of the Q-band to ~710 nm (Fig.1). Optical constants, as determined for the thin ZnPC film using spectroscopic ellipsometry (*see Supporting Information, Figs.S.2, S.3 and S.4*), illustrate the strong absorbance (κ_{ZnPC}) for the thin film near 700 nm and the corresponding discontinuity in the refractive index (n_{ZnPC}) over this same spectral region.

The coupling of this ZnPC film, with its strong molecular resonance, with a SP in the Ag substrate was studied by measuring the optical reflection of p (R_p) and s-polarized (R_s) light with the sample in the Kretschmann configuration (Fig.2A). The uncoated silver film (47 nm thick) exhibits the expected sharp decrease in reflectivity for p-polarized light associated with the formation of an SP. At an incident angle of 48°, the reflectance minimum occurs at a wavelength of ~437 nm (Fig.2B). Reflection of s-polarized light under these conditions results in a high reflectivity (Fig.2C), consistent with conditions of total internal reflection. The addition of a thin (6 nm) ZnPC film to the silver results in a red-shift of the SP to 492 nm, and no change in the s-polarized response. The behavior of a thicker (19 nm) ZnPC film shows several notable features. The reflectance minimum in p-polarized light has

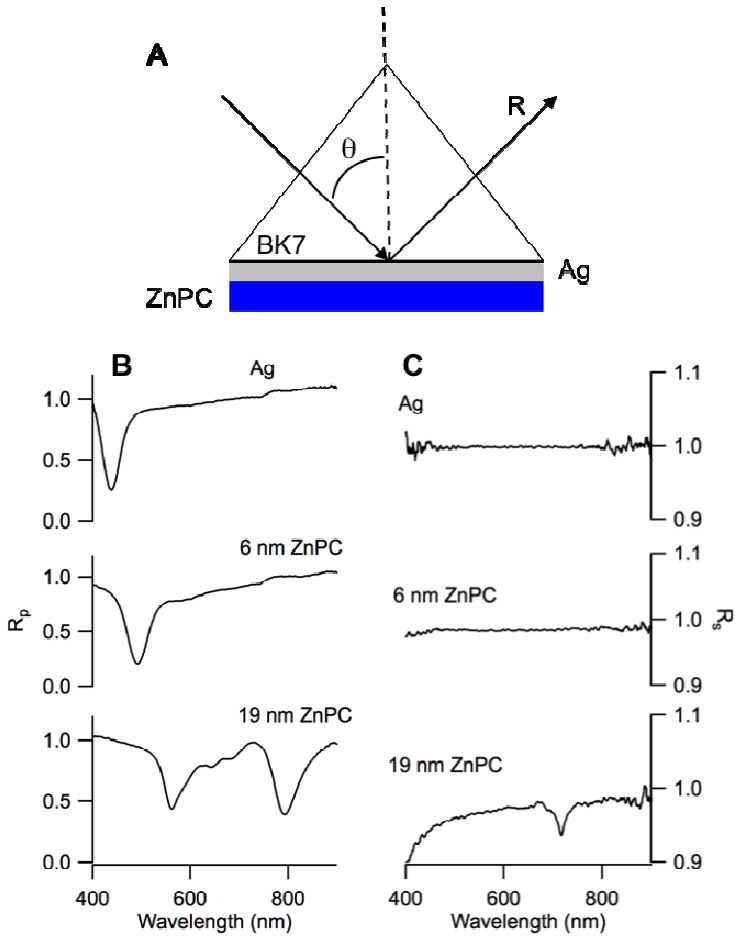

Figure 2 (A) Schematic of Krestchmann configuration used for measurement of reflectance spectra. Reflectance spectra for 0, 6 and 19 nm thick ZnPC films in air on 47 nm Ag/BK7 prism in Kretschmann configuration at 48° angle of incidence: (B) p-polarized reflectance (R_p) and (C) s-polarized reflectance (R_s).

red-shifted, but it has also split into two distinct minima, one appearing at ~561 nm and the other at 792 nm. In addition, reflection of s-polarized light now shows an unusual reflectance minimum, albeit a weak one, at 716 nm

More detail about the nature of these features can be illustrated with reflection images taken at several different incident angles (Fig.3). These reflection images for the bare silver film (Fig.3A) show the expected behaviors: the s-polarized image (R_s) is uniform and a strong resonance minimum appears in the p-polarized image (R_p). The dispersive nature of the SP in the p-polarized image is highlighted by the red-shifting of the reflection minimum with decreasing angle (Fig.3A). Reflection images of the 19 nm ZnPC film on silver show two clearly resolved minima, with a gap in between (Fig.3B). The peak that appears at longer wavelengths displays an obvious dispersive behavior by shifting to longer wavelengths with decreasing angle. The shorter wavelength peak also shifts, but to a lesser degree. A notable feature in this image is that the SP resonance is completely quenched between the two minima at all angles. The minimum in the s-polarized image (Fig.3B) is also apparent and this feature appears nondispersive under these conditions, with its position unaffected by changing angle. However, this peak is indeed dispersive, as we will show in subsequent data and calculations (*vide infra*).

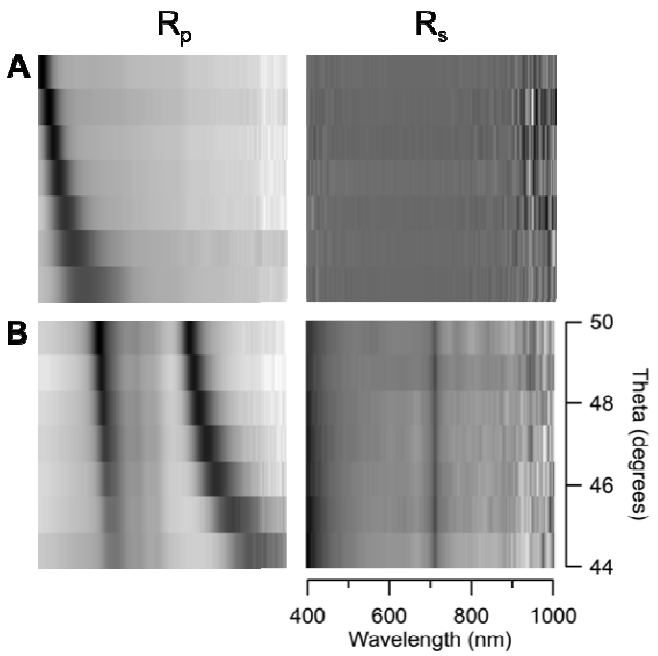

Figure 3 Measured reflectance images for p-polarized (R_p) and s-polarized (R_s) light as a function of the angle of incidence and wavelength for (A) 47 Ag film and (B) with additional 19 nm ZnPC in Kretschmann configuration. The intensity ranges correspond to $0 < R_p < 1.2$ and $0.9 < R_s < 1.1$.

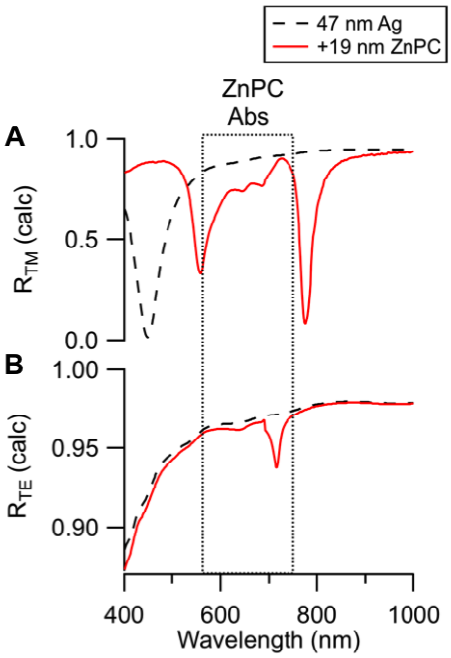

Figure 4 Calculated reflectance (R) spectra for 47 nm Ag (dashed lines) and 47 nm Ag + 19 nm ZnPC (solid red lines) films in Kretschmann configuration at 48° angle of incidence using transverse magnetic (TM = p-polarized) and transverse electric (TE = s-polarized) light. The dotted box denotes the region of the visible spectrum enclosing the molecular resonance for ZnPC.

Red-shifting of the resonance peak in the p-polarized data associated with film formation is the behavior typically seen with SPs. Therefore, the appearance of two peaks, and the quenching of the resonance in the spectral region near the molecular resonance, must be associated with the coupling that occurs between the molecular resonance and the SP resonance. This behavior can be explained by considering the nature of the plasmon and the impact of the molecular resonance on the SP matching condition (*vide infra*). The appearance of a minimum in the s-polarized spectra near a molecular resonance has not been reported, although a recent publication has highlighted an enhanced transmission through a nanohole metal array when coated with a thin dye film.[25] We believe that the peak appearing in that result, and the peak appearing here, have the same fundamental origin, which is the emergence of a guided wave in the thin adsorbed film (*vide infra*).

In order to more fully understand the coupling of the molecular resonance of ZnPC and the SP in the silver film, we completed a series of optical modeling calculations. The optical constants of silver and ZnPC were determined by combining the film heights, as measured by atomic force microscopy (*see Supporting Information, Fig.S1*) with spectroscopic ellipsometry of the two films. A four-layer optical model was then used to calculate the reflection of transverse magnetic (TM = p-polarized) and transverse electric (TE = s-polarized) light as a function of ZnPC thickness, wavelength, and angle for the BK7 prism/Ag/ZnPC/air multilayer. Modeling results for a bare 47 nm Ag film and also with an additional 19 nm ZnPC layer at 48° are shown in Fig.4. A comparison between the calculated reflectance spectra in Fig.4 with the experimental results in Fig.2 shows a significant similarity. The bare silver films show a nearly identical resonance minimum in the p-polarized spectrum (Fig.4A) and little of note in the s-polarized result (Fig.4B). The addition

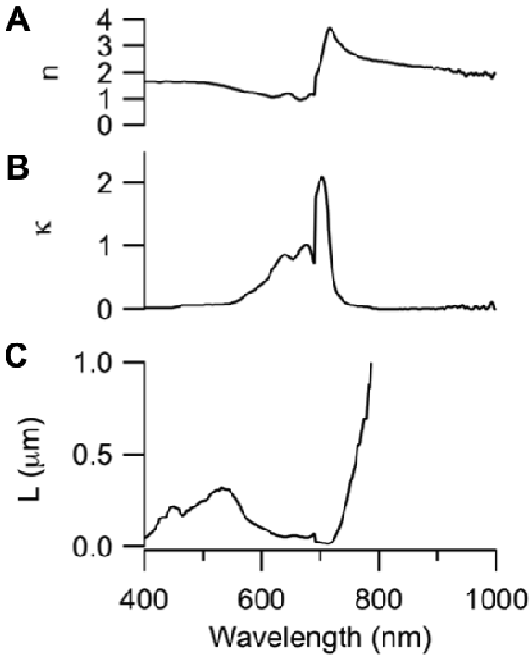

Figure 5 (A) Refractive index (n) and (B) absorption coefficient (κ) for ZnPC as determined by spectroscopic ellipsometry of 19 nm film. (C) Calculated propagation length (L) for optical wave along interface of silver and ZnPC.

of a 19 nm ZnPC film shows the same red-shifting and splitting of the resonance in the p-polarized spectrum, with nearly identical fine structure as seen in the experimental results. Notably, the strong resonance minima in the p-polarized spectra are completely outside the region of the spectrum where the ZnPC Q-band absorbance lies (denoted by the dotted box in Fig.4), indicating the same quenching behavior as the experimental results. The new minimum observed in the s-polarized data with the 19 nm ZnPC is also apparent in the calculated results. Thus, both of these behaviors can be explained by standard optical theory, and are the direct result of the optical properties of the ZnPC dye, and how they interact with the SP in the Ag film.

The splitting of the SP resonance and the quenching that occurs near the molecular resonance of the ZnPC film can be explained by considering the wavevector ($\square_{sp}$) of the SP parallel to the ZnPC/Ag interface. For a macroscopically thick ZnPC film, this wavevector can be described by the following relationship

$$k_{sp} = \frac{2\pi}{\lambda}\sqrt{\frac{\varepsilon_m \varepsilon_d}{\varepsilon_m + \varepsilon_d}} \qquad (2)$$

where ε_m is the dielectric constant of the silver, and ε_d is the dielectric constant of the ZnPC film. In a general case, $\square_{sp}$ is a complex number

$$k_{sp} = k_{sp}^{'} + i \cdot k_{sp}^{"} \qquad (3)$$

In order for this SP to exist and propagate along the metal/film interface, the propagation length (L),[4] as defined by

$$L = \frac{1}{k_{sp}^{"}} \qquad (4)$$

must have a nonzero value. This propagation length can be readily calculated by considering the wavelength-dependent optical constants of the metal and dielectric films. The

refractive index (n) and absorption coefficient (κ) for ZnPC (Fig.5A and B) illustrate the resonance associated with the Q-band. The absorption coefficient goes through a maximum in this region (~ 700 nm), and, as is consistent with the Kramers-Kronig relation, the refractive index decreases when approaching this absorbance from smaller wavelengths and then exhibits a discontinuity to reach a maximum value just to the right of the absorbance maximum, before decreasing again. Using these optical parameters for ZnPC, along with the dielectric properties of Ag, allows one to calculate the propagation length (L) for this interface as a function of wavelength (Fig.5C). These results indicate that L obtains nonzero values between ~ 400 and 550 nm, and then again above ~750 nm. However, between 550 and 750 nm, L approaches zero. These results indicate that the SP can exist above and below this spectral region, but is unable to propagate near the molecular resonance. This behavior is primarily the result of the large value of the absorption coefficient κ for ZnPC in this region, which makes the imaginary part of ε_d large, and consequently creates a large value for $\square_{sp}''$ and a vanishing value for L. Similar calculations using a nonabsorbing material (*Supporting Information, Fig.S7A&B*) show only an increasing L with increasing wavelength, which supports the presence of a propagating SP over much of the visible spectrum. An idealized absorbing material, with a Lorentzian absorbance peak, gives a value of nearly L = 0 over the entire spectral region associated with the absorbance peak (*Supporting Information, Fig.S7C&D*).

For a metal/film interface, the SP wavevector can be simplified. At energy levels well away from the plasma frequency for a given metal, the imaginary part of the metal's dielectric constant takes on large, negative values, which allows $\square_{sp}$ to be approximated by

$$k_{sp} \approx \frac{2\pi}{\lambda}\sqrt{\varepsilon_d} \qquad (5)$$

Far from the molecular absorbance (or for a non-absorbing material), where the absorption coefficient of the film is zero, this wavevector can be written as

$$k_{sp} \approx \frac{2\pi}{\lambda} n_d \qquad (6)$$

which is a purely real number, indicating that the propagation constant L is very large and that the plasmon is supported at this interface. However, near the molecular resonance, the imaginary part of the film's dielectric constant goes through an inflection that tracks the value of n ($\varepsilon_d^{'} = 2n\kappa$), while the real component approaches a negative square of the absorption coefficient ($\varepsilon_d^{''} = n^2 - \kappa^2$). Thus, the plasmon wavector can be approximated as

$$k_{sp} \approx \frac{2\pi}{\lambda} i \cdot \kappa \qquad (7)$$

and the propagation constant approaches the limit of

$$L = \frac{1}{2\pi\kappa} \qquad (8)$$

Thus, the larger the value of the absorption coefficient (κ), the smaller the wave propagation length will be. Therefore, a molecular resonance will result in the extinguishing of the SP.

The second feature in both experimental and modeling results was the appearance of a new peak in the s-polarized spectrum. More detail regarding the nature and

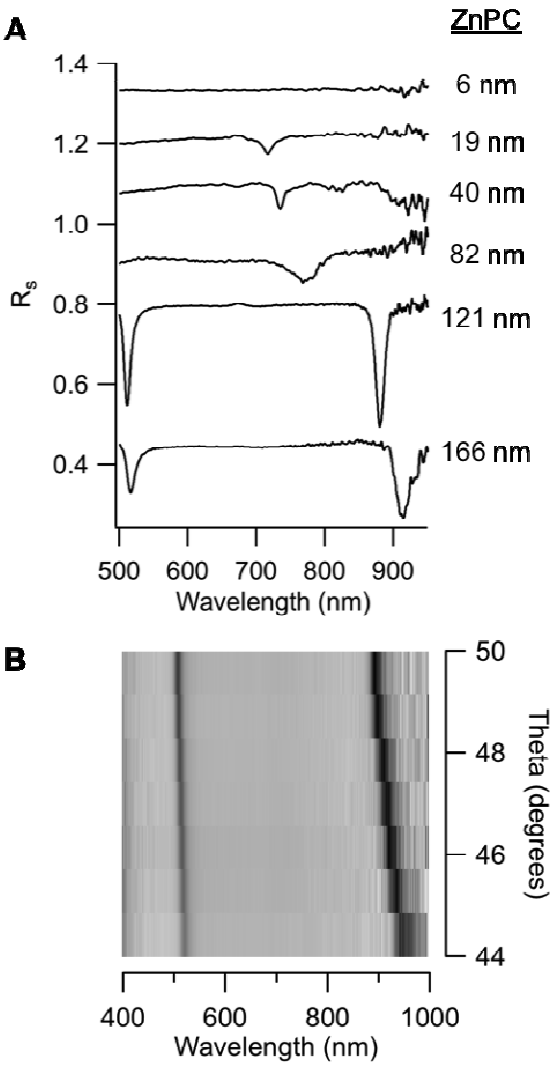

Figure 6 Measured reflectance spectra with s-polarized light (R_s) for (A) ZnPC films of increasing thickness on 47 nm Ag in Kretschmann configuration at 48° angle of incidence. (B) Reflectance image for s-polarized (R_s) light as a function of angle of incidence and wavelength for 166 nm ZnPC film on 47 nm Ag.

origins of this peak can be deduced through some additional experimental data, and complementary optical modeling results. The results from Fig.3B show that the minimum in the s-polarized data does not change wavelength with angle, which would suggest that it is a nondispersive peak, and somehow related to the molecular absorbance. However, increasing the thickness of the film suggests that this peak is indeed dispersive. Fig.6 shows experimental reflectance spectra for ZnPC films of various thicknesses between 6 and 166 nm on Ag. The absence of a peak is noted in the 6 nm film, followed by the first appearance of the peak with a 19 nm film. With larger ZnPC film thicknesses, the peak position is seen to red-shift significantly. The peak magnitude also increases as the film thickness increases from 19 to 121 nm. The red-shifting of the peak position for the 19 nm film from its initial value at 716 nm to the final peak position of ~920 nm for the 166 nm ZnPC film clearly shows that this peak is dispersive. Additional evidence of dispersion can be seen in Fig.6B for the 166 nm thick ZnPC film, which shows a red-shift in the peak position with decreasing angle of incidence. A second peak, whose origin is similar to the first (*vide infra*), is also observed in the two thickest ZnPC films at wavelengths near ~510 nm.

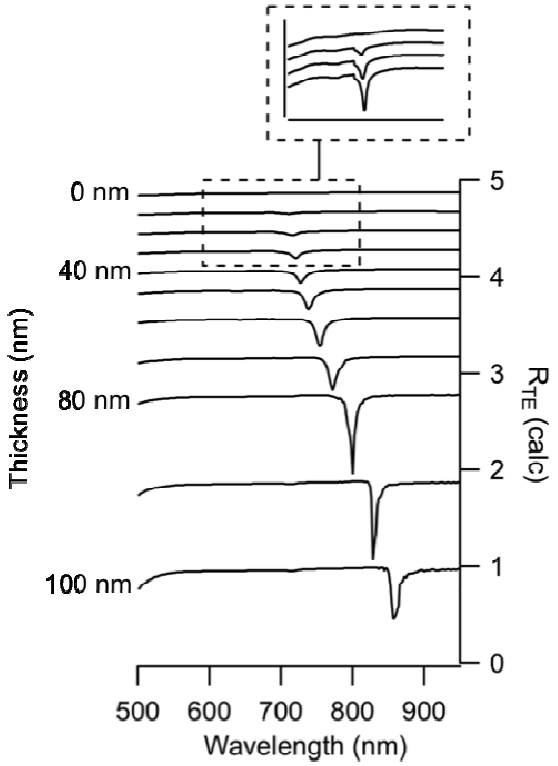

Figure 7 Calculated reflectance spectra using transverse electric (TE) light (s-polarized) for increasing ZnPC film thicknesses on Ag in Kretschmann configuration. Line plots showing reflectance spectra with increasing ZnPC film thickness from 0 to 100 nm. The inset shows an expanded view of the films with 0, 10, 20 and 30 nm ZnPC thicknesses.

Optical modeling supports the behavior seen in this experimental data. Fig.7 depicts a series of computed reflectance spectra using s-polarized (TE) light as a function of ZnPC thickness. Spectra are plotted for film thicknesses between 0 and 140 nm, at increments of 10 nm. The thinnest films are highlighted in the figure inset, and show spectra for films of 0 to 30 nm. As expected, the peak is absent at 0 nm ZnPC, corresponding to the silver layer. The peak first appears at 10 nm, and then increases in magnitude, but does not shift appreciably, up to 30 nm. At thicknesses greater than 30 nm, the peak grows in magnitude, and also shifts appreciably to the red. Thus, the dispersive nature of this peak is confirmed with the large red-shift with increasing thickness. Although the original peak position was located near the maximum in the molecular absorbance, the dispersive nature of the peak confirms that this initial peak position being near the molecular absorbance was coincidental. As we will prove in the following passages, the origin of this peak is ultimately that of a guided mode within the ZnPC layer, which is excited by a SP in the silver film.[4]

With increasing ZnPC thickness, the SP that is excited at the silver-ZnPC interface is able to couple to a guided mode within the ZnPC layer, which produces a peak in the s-polarized spectra. The location and magnitude of this guided mode is impacted by the coupling between the SPP in the Ag film and the molecular resonance on the ZnPC layer due. The propagation of this guided mode is also hindered by the quenching of the SPP associated with the molecular resonance, which explains the reduced amplitude of the peaks when they are located near the molecular resonance.

Evidence that numerous guided modes can be excited by both s and p-polarized light at increasing film thickness can be shown by additional model results. As an illustration, Fig.8 depicts computed p and s-polarized spectra with ZnPC films of thicknesses between 0

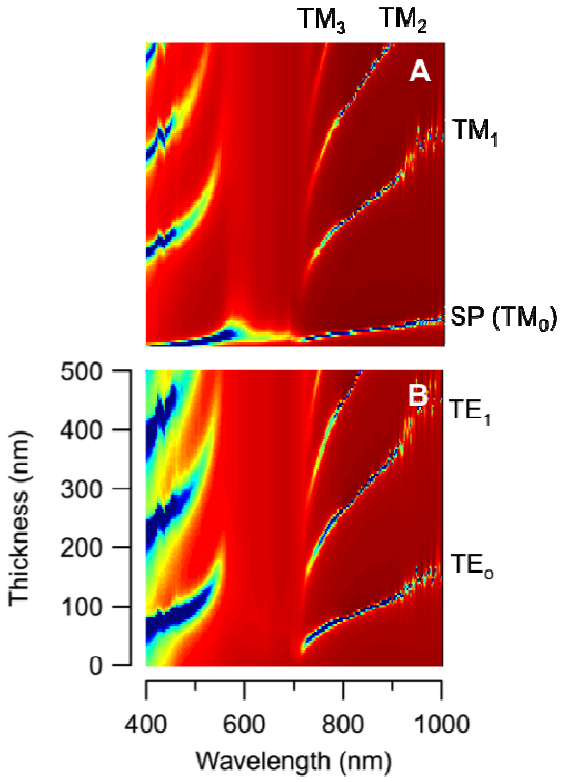

Figure 8 Calculated reflectance images for ZnPC-coated Ag (dashed lines) as a function of ZnPC thickness from 0 to 500 nm in Kretschmann configuration at 48° angle of incidence using (A) transverse magnetic (TM = p-polarized) and (B) transverse electric (TE = s-polarized) light. The modes for the guided waves are identified in the figure. The scale bars are $0.4 < R_{TM} < 1$ and $0.8 < R_{TE} < 1$.

and 500 nm. Numerous guided modes appear in these spectra, and labels for particular modes have been included. The peaks observed in the experimental data of Fig.6 correspond to the TE_0 mode (Fig.8B). For TE_0, the first peak to appear at small film thicknesses is near 700 nm. It then red-shift with increasing film thicknesses. As the film thickness reaches ~80 nm, a second peak appears in the TE_0 mode at small (~400 nm) wavelengths. This peak also shifts to longer wavelengths with increasing film thicknesses. This second peak in the simulated results for TE_0 corresponds to the second peak observed near ~510 nm for the 121 and 166 nm thick films in the experimental data.

It should be noted that several features in the waveguide modes depicted in Fig.8 differ from what would be observed in a typical nonabsorbing waveguide layer. The modes shown here are highly nonlinear with thickness, and are quenched near the molecular resonance so that their magnitudes go to zero. In contrast, the location of a guided mode in a nonabsorbing dielectric slab waveguide would vary linearly with thickness, and appear over the entire spectral region. To illustrate this further, a slab waveguide sandwiched between two perfect mirror layers, for example, would support guided modes for TE excitation that satisfy the relationship[4,28,29]

$$\frac{2\pi}{\lambda} n_d h_d \cos(\theta) = m\pi \qquad (9)$$

where n_d is the dielectric constant of the waveguide layer, h_d is the waveguide thickness, θ is the incident angle, and m = 1, 2, ... are the modes of the TE guided wave. The increase in wavelength with increasing film thickness would be strictly linear in this case, with the slope increasing for higher modes (increasing m). Numerical results for an asymmetric waveguide slab, as is the case here, with a nonabsorbing, dielectric film in the Kretschman configuration on

a 47 nm Ag film, also exhibits a linear increase in wavelength with thickness (*Supporting Information, Fig.S9)*.

Although the complete solution describing the matching conditions for an asymmetric waveguide is more complex,[4,28] the general behavior for the ZnPC film system can still be interpreted with Eqn.9. As noted, the peaks in Fig.8 are nonlinear. However, they approach linearity far from the molecular absorbance (high and low wavelengths). In these near-linear regions, the peaks exhibit an increasing slope with increasing mode number, which is consistent with Eqn.9. A simple explanation for the nonlinear shape of the modes near the molecular resonance comes from the fact that the layer height (h_d) and the refractive index (n_d) are inversely proportional in the guided mode (Eqn.9). By simply inverting the refractive index curve for ZnPC from Fig.5A, one can reproduce the shape of the curves in Fig.8. The most notable consequence of this behavior in the experimental results is that the guided mode appears in the s-polarized spectra at much smaller film thicknesses with ZnPC than would be the case with a nonabsobing, dielectric material because of the abnormally high value of n_d provided by the molecular resonance.

Ultimately, for a guided mode to persist, it must be able to propagate within the waveguide layer. However, the conditions that lead to quenching of the SP also lead to quenching of the guided modes. The increased absorption coefficient near the molecular resonance in the ZnPC film diminishes the propagation length of the guided modes so that they are also quenched. Nevertheless, all other features of these modes are consistent with what would be observed in a traditional dielectric waveguide.

4.5 Conclusion

The interaction of surface plasmons with a molecular resonance leads to the appearance of several new features not typically observed with SPs that are coupled to transparent materials. The molecular resonance in a ZnPC dye film, for example, causes the SP in a silver layer to split into two branches. The gap between these branches reflects quenching of the SP. The origin of this quenching is due to the decreased propagation length for the SP due to the large absorption coefficient for the dye near the molecular resonance. The magnitude of the quenching is a strong function of the strength of the molecular resonance, as well as the degree of overlap between the SP resonance and that of the adsorbed molecule.

The appearance of a guided mode in the s-polarized spectra is a feature that occurs with this particular dye, but also appears in transparent films. In a transparent film, this guided mode (and others appearing in p and s-polarized light) would display a linear dispersion relation. However, with the dye film, the guided mode is also quenched near the molecular resonance, and the resulting dispersion curve is highly nonlinear near the resonance location. However, the nature of this dispersion relation follows what would be expected based upon the optical properties, particularly the refractive index, of the molecular film.

The coupling of molecular resonances to surface plasmons provides an information rich system for optical sensing and the ability to tune the optical response through the degree of overlap with the molecular resonance. The novel features exhibited by this type of system have been used in the design of new analytical and sensing schemes in both nanoparticle (LSPR) and thin film (SPP) systems. One could envision exploiting these features further in the development of new optical spectroscopies, sensor systems, and in optoelectronic devices.

4.6 Acknowledgement

This work was funded by the National Science Foundation (CHE 0809509), the National Institutes of Health (R44 RR023763- 02), and the W. M. Keck Foundation through the W. M. Keck Laboratory for High Throughput Atom-Scale Analysis at Iowa State University.

4.7 Supporting Information

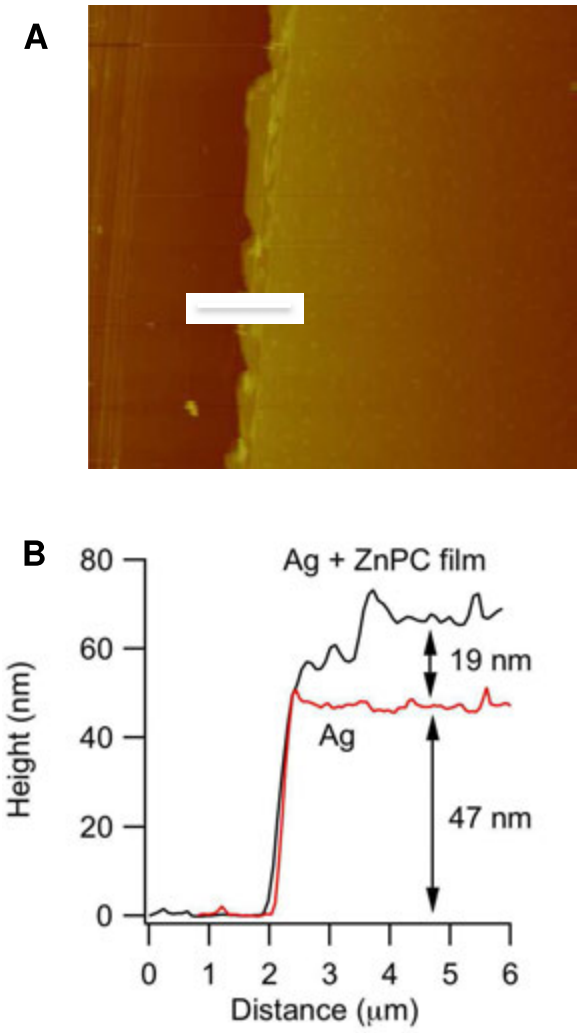

Figure S1 (A) Atomic force micrograph and (B) line scan showing 47 nm Ag film and 19 nm ZnPC film on mica.

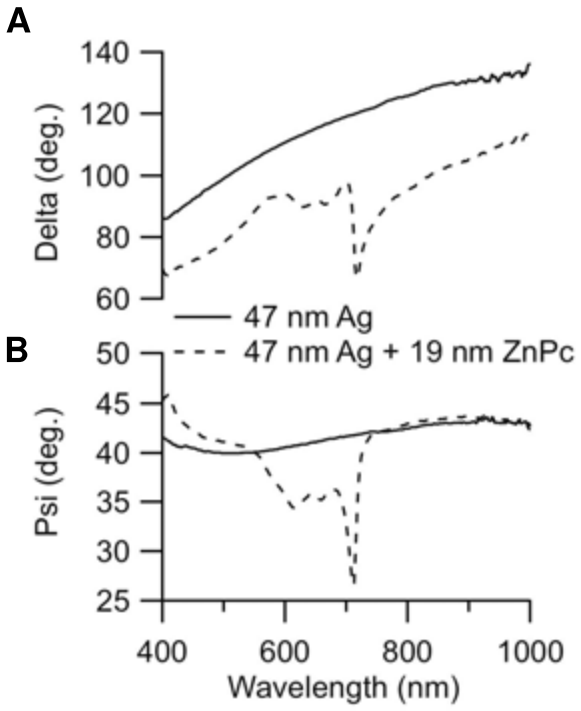

Figure S2 Spectroscopic ellipsometry of 47 nm Ag (solid line) and 47 nm Ag + 19 nm ZnPC (dashed line) films on glass. (A) Delta and (B) Psi. Measurements were taken using a custom rotating analyzer ellipsometer (RAE) at 70 degrees with a tungsten halogen light source.

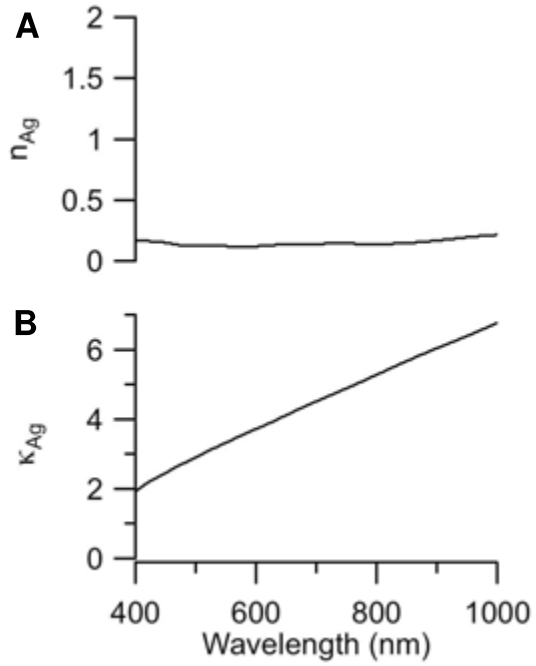

Figure S3 Refractive index (n) and absorption coefficient (κ) for 47 nm Ag film on glass determined with spectroscopic ellipsometry.

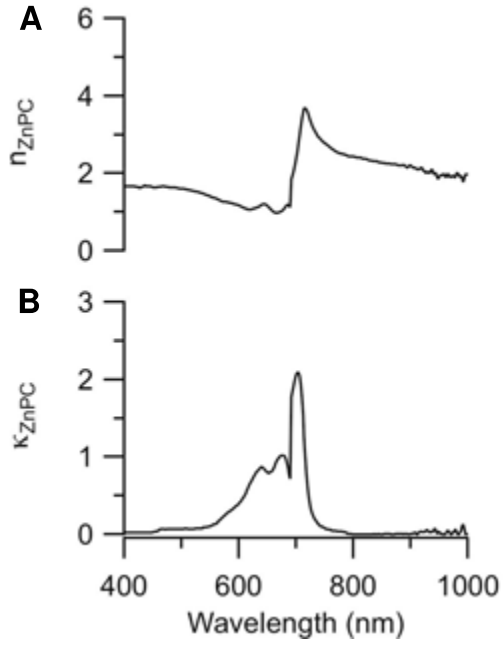

Figure S4 Refractive index (n) and absorption coefficient (κ) for ZnPC as determined by fitting spectroscopic ellipsometry results (Fig.S2) for 19 nm ZnPC film on 47 nm Ag/Glass.

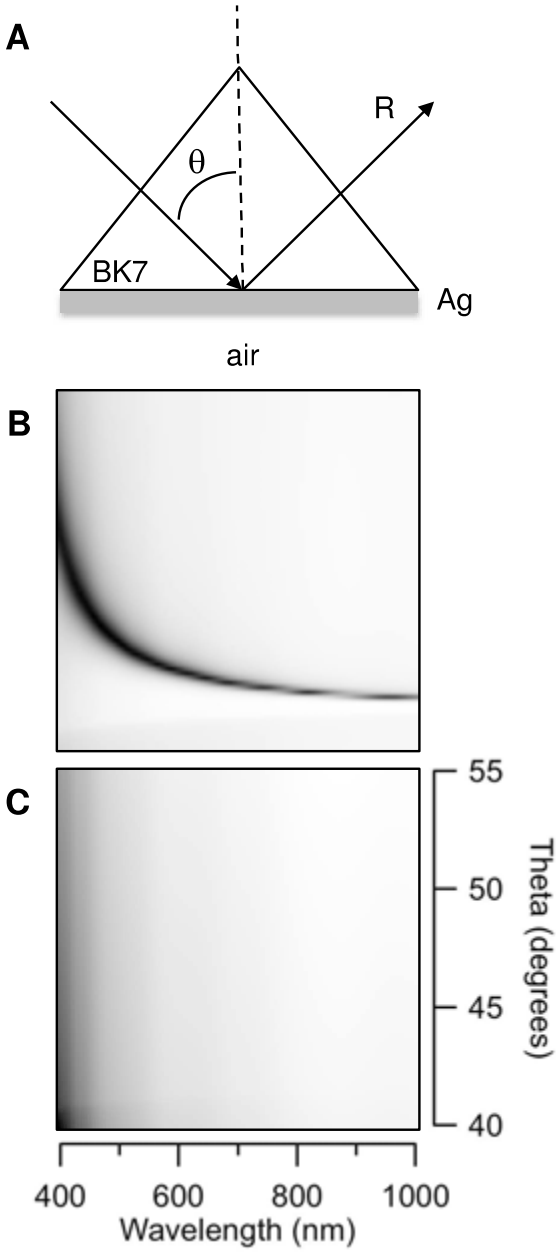

Figure S5 Calculated reflectance spectrum for BK7 prism with 47 nm Ag film in Kretschmann configuration (A) as a function of angle of incidence. Reflectance for (B) transverse magnetic (TM) and (C) transverse electric (TE) light. The intensity scales are:(B)0<RTM <1.2and(C)0.9<RTE <1.1

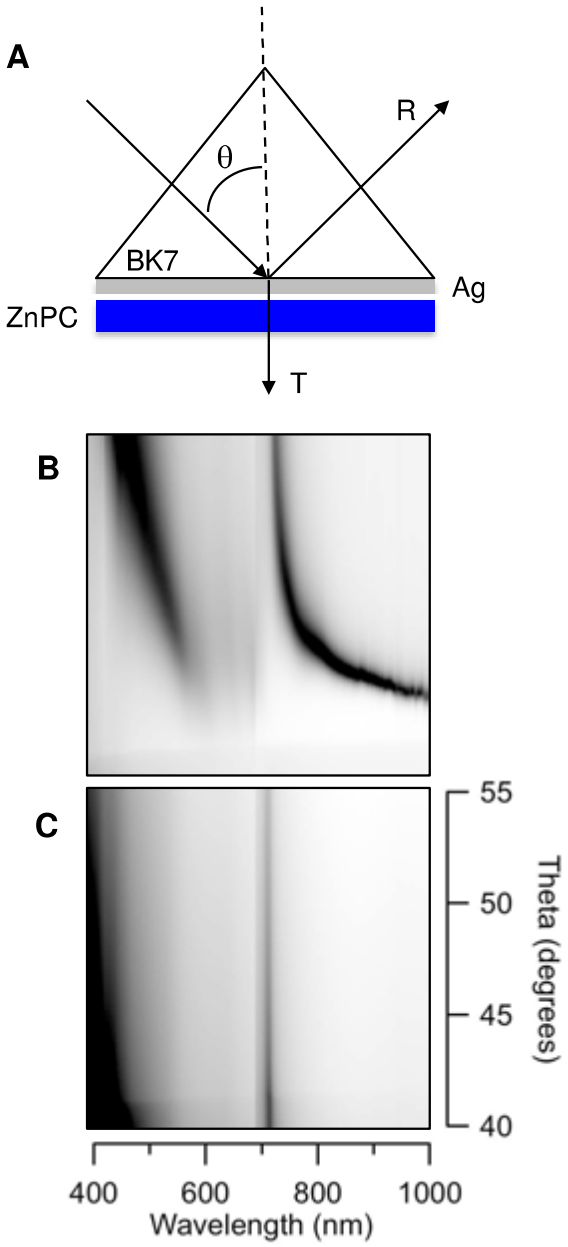

Figure S6 Calculated reflectance spectra for Kretschman configuration (A) using BK7 prism with 47 nm Ag and 19 nm ZnPC films as a function of angle of incidence. Reflectance for (B) transverse magnetic (0 < RTM < 1.2) and (C) transverse electric (0.9 < RTE < 1.1) light.

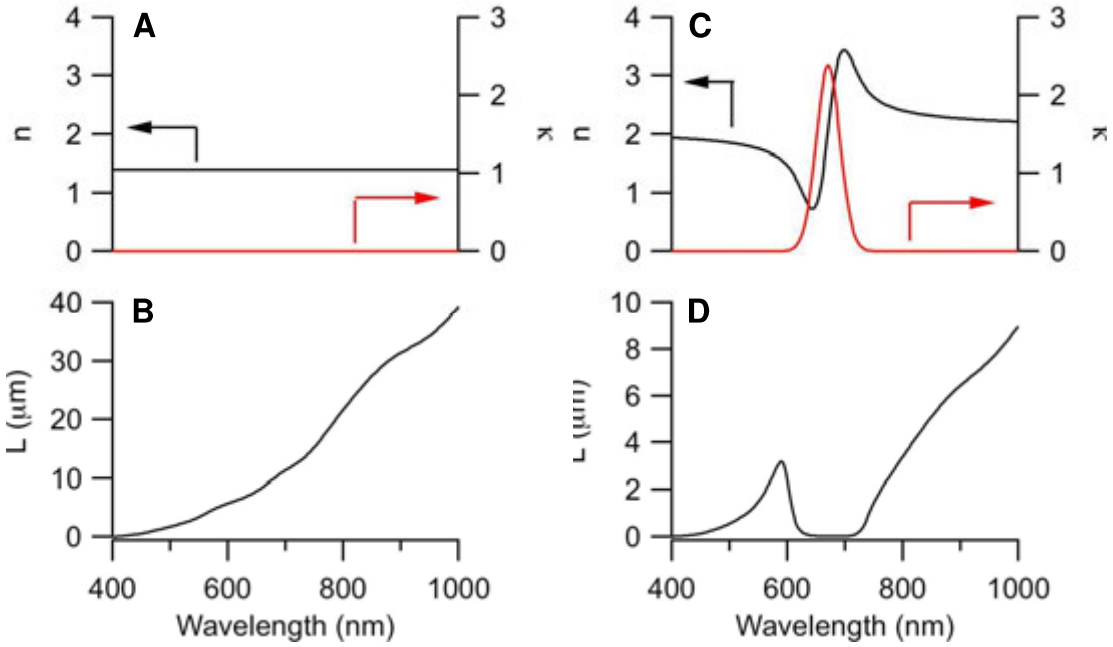

Figure S7 Optical constants and SPR propagation length for films on silver. Non-absorbing material (κ=0) with constant refractive index: (A) optical constants and (B) SPR propagation length. Hypothetical material with strong molecular resonance (κ ≠ 0) with variable refractive index: (C) optical constants and (D) SPR propagation length.

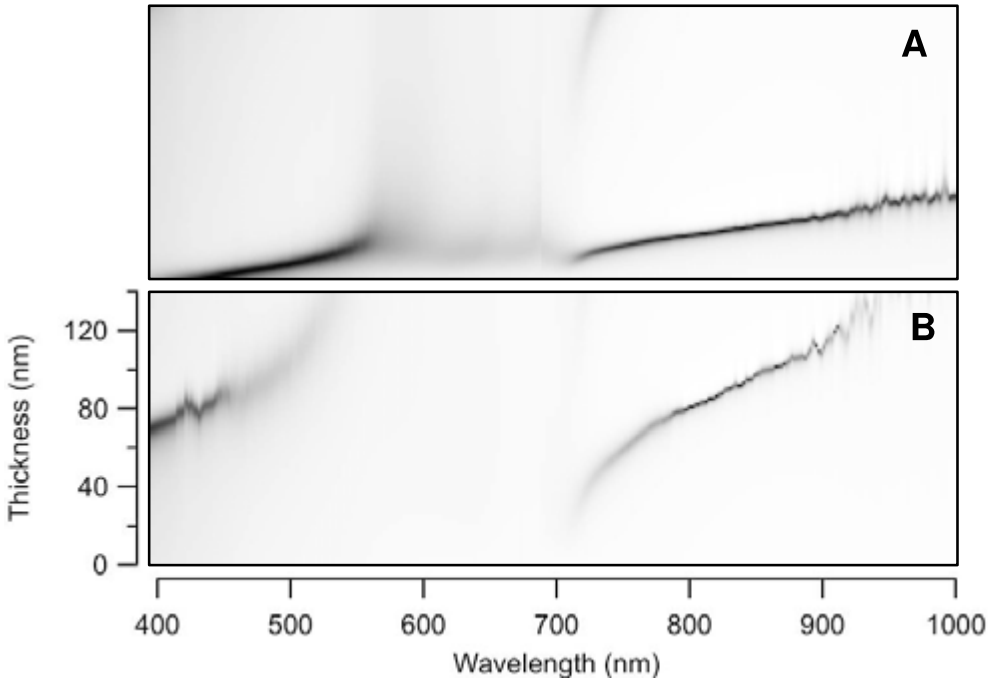

Figure S8 Calculated reflectance spectrum for Kretschman configuration at θ = 46° using BK7 prism with 47 nm Ag as a function of ZnPC film thickness from 0 to 140 nm ZnPC. Reflectance for (A) transverse magnetic (0 < RTM < 1.2) and (B) transverse electric (0.9 < RTE < 1.1) light.

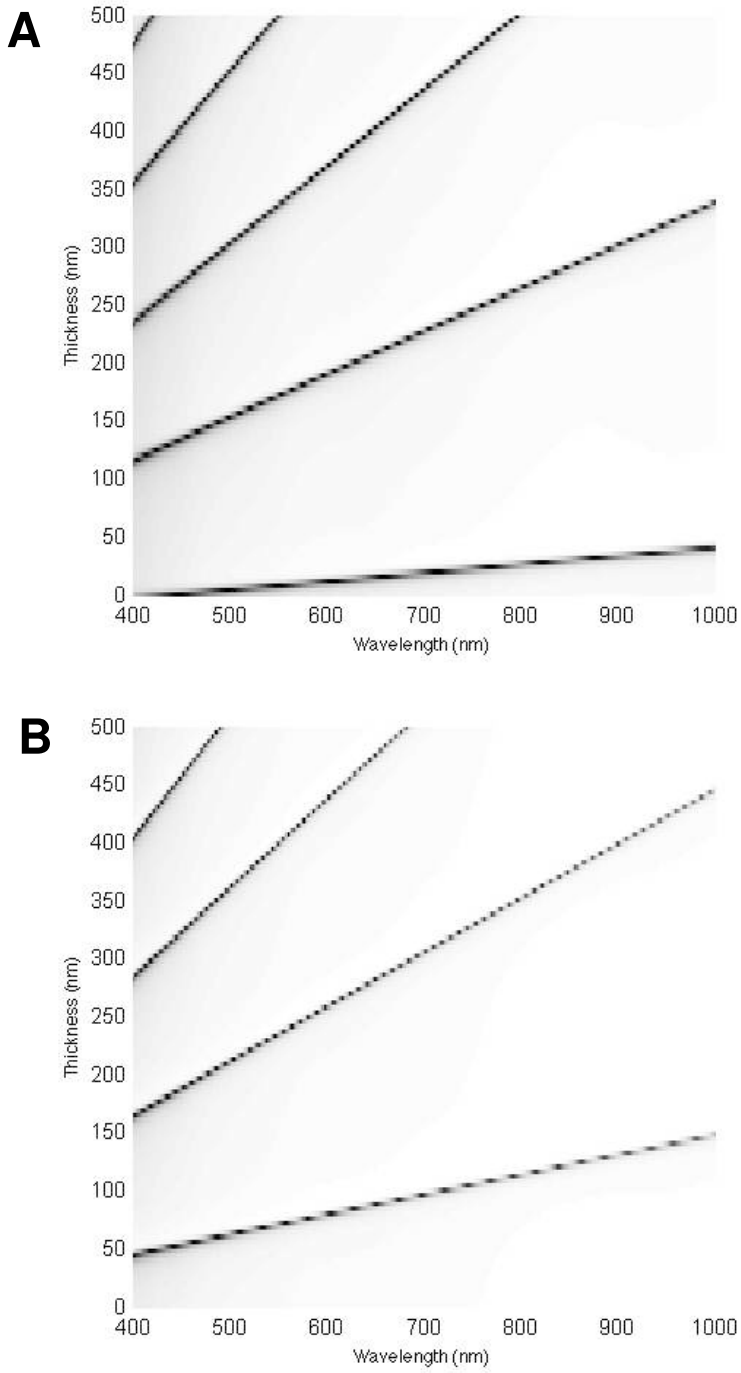

Figure S9 Calculated reflectance spectrum for Kretschman configuration at θ = 46° using BK7 prism with 47 nm Ag as a function of thickness of dielectric film (n_{film} = 2, κ_{film}=0) from 0 to 500 nm. Reflectance for (A) transverse magnetic and (B) transverse electric light.

4.7 References

(1) Homola, J. *Anal Bioanal Chem* **2003**, *377*, 528-539.

(2) Homola, J. *Chem Rev* **2008**, *108*, 462-493.

(3) Homola, J.; Yee, S. S.; Gauglitz, G. *Sensor Actuat B-Chem* **1999**, *54*, 3-15.

(4) Knoll, W. *Annu Rev Phys Chem* **1998**, *49*, 569-638.

(5) Pockrand, I.; Brillante, A.; Mobius, D. *J Chem Phys* **1982**, *77*, 6289-6295.

(6) Pockrand, I.; Swalen, J. D.; Gordon, J. G.; Philpott, M. R. *J Chem Phys* **1979**, *70*, 3401-3408.

(7) Pockrand, I.; Swalen, J. D.; Santo, R.; Brillante, A.; Philpott, M. R. *J Chem Phys* **1978**, *69*, 4001-4011.

(8) Fischer, U. C.; Bortchagovsky, E.; Heimel, J.; Hanke, R. T. *Appl Phys Lett* **2002**, *80*, 3715-3717.

(9) Bellessa, J.; Bonnand, C.; Plenet, J. C.; Mugnier, J. *Phys Rev Lett* **2004**, *93*.

(10) Vasa, P.; Pomraenke, R.; Cirmi, G.; De Re, E.; Wang, W.; Schwieger, S.; Leipold, D.; Runge, E.; Cerullo, G.; Lienau, C. *Acs Nano* **2010**, *4*, 7559-7565.

(11) Boussaad, S.; Pean, J.; Tao, N. J. *Anal Chem* **2000**, *72*, 222-226.

(12) Wang, S.; Boussaad, S.; Wang, S.; Tao, N. J. *Anal Chem* **2000**, *72*, 4003-4008.

(13) Zangeneh, M.; Doan, N.; Sambriski, E.; Terrill, R. H. *Appl Spectrosc* **2004**, *58*, 10-17.

(14) Hur, Y.; Ock, K.; Kim, K.; Jin, S.; Gal, Y.; Kim, J.; Kim, S.; Koh, K. *Anal Chim Acta* **2002**, *460*, 133-139.

(15) Nakkach, M.; Lecaruyer, P.; Bardin, F.; Sakly, J.; Ben Lakhdar, Z.; Canva, M. *Appl Optics* **2008**, *47*, 6177-6182.

(16) Wang, S.; Boussaad, S.; Tao, N. J. *Rev Sci Instrum* **2001**, *72*, 3055-3060.

(17) Chen, H. J.; Ming, T. A.; Zhao, L.; Wang, F.; Sun, L. D.; Yan, C. H.; Wang, J. F. *Nano Today* **2010**, *5*, 494-505.

(18) Haes, A. J.; Zou, S. L.; Zhao, J.; Schatz, G. C.; Van Duyne, R. P. *J Am Chem Soc* **2006**, *128*, 10905-10914.

(19) Liu, G. L.; Long, Y. T.; Choi, Y.; Kang, T.; Lee, L. P. *Nat Methods* **2007**, *4*, 1015-1017.

(20) Qu, W. G.; Deng, B.; Zhong, S. L.; Shi, H. Y.; Wang, S. S.; Xu, A. W. *Chem Commun* **2011**, *47*, 1237-1239.

(21) Nabika, H.; Takase, M.; Nagasawa, F.; Murakoshi, K. *J Phys Chem Lett* **2010**, *1*, 2470-2487.

(22) Zheng, Y. B.; Yang, Y. W.; Jensen, L.; Fang, L.; Juluri, B. K.; Flood, A. H.; Weiss, P. S.; Huang, T. J.; Stoddart, J. F. *Nano Lett* **2009**, *9*, 819-825.

(23) Zheng, Y. B.; Kiraly, B.; Cheunkar, S.; Huang, T. J.; Weiss, P. S. *Nano Lett* **2011**, *11*, 2061-2065.

(24) Zheng, Y. B.; Juluri, B. K.; Jensen, L. L.; Ahmed, D.; Lu, M. Q.; Huang, T. J.; Jensen, L. *Adv Mater* **2010**, *22*, 3603-+.

(25) Hutchison, J. A.; O'Carroll, D. M.; Schwartz, T.; Genet, C.; Ebbesen, T. W. *Angew Chem Int Edit* **2011**, *50*, 2085-2089.

(26) Hansen, W. N. *J Opt Sci Am* **1968**, *58*, 380-390.

(27) *Applications of Phthalocyanines*; Kadish, K. M.; Smith, K. M.; Guilard, R., Eds.; Academic Press: San Diego, 2002; Vol. 19.

(28) Marcuse, D. *Theory of Dielectric Optical Waveguides*; Second Edition ed.; Academic Press: New York, 1991.

(29) Syms, R.; Cozens, J. *Optical Guided Wave Components and Devices*; McGraw-Hill Companies: New York, 1992.

CHAPTER 5 USE OF DISPERSION IMAGING FOR GRATING-COUPLED SURFACE PLASMON RESONANCE SENSING OF MULTILAYER LANGMUIR-BLODGETT FILMS

Analytical Chemistry, **85** 4080-4086 (2013)

Wei-Hsun Yeh and Andrew C. Hillier

5.1 Abstract

We report grating-coupled surface plasmon resonance measurements involving the use of dispersion images to interpret the optical transmission through a metal-coated grating, and the influence of multilayer Langmuir-Blodgett films of arachidic acid on that response. Optical transmission through a grating coated with a thin, gold film exhibits features characteristic of the excitation of surface plasmon resonance due to coupling with the nanostructured grating surface. Evidence of numerous surface plasmon modes associated with coupling at both front (gold/air) and back (gold/substrate) grating interfaces is observed. The influence of wavelength and angle of incidence on plasmon coupling can be readily characterized via dispersion images, and the associated image features can be indexed to matching conditions associated with several diffracted orders at both the front and back of the grating. These features collapse onto a set of global dispersion curves when plotted as peak energy versus the grating wavevector, with feature locations clustered according to the refractive index values of the neighboring dielectric material, either air or polycarbonate. Coating of the grating with multilayer arachidic acid films via Langmuir-Blodgett deposition results in red-shifting of some, but not all, of the plasmon features. The magnitude of the shift is a function of the film thickness, wavelength, and angle of incidence. Dispersion images clearly depict the red-shifting and also broadening of the front side

features with increasing film thickness. In contrast, little change is observed in features associated with the back-side of the grating. The nature and magnitude of the interaction between the plasmon modes appearing at the front and back sides of the grating are discussed and analyzed in terms of the predicted interactions determined via optical modeling calculations.

5.2 Introduction

Optical sensors based upon surface plasmon resonance (SPR) have become exceedingly popular analytical tools for thin film and adsorption sensing.[1] One of the key design parameters for SPR sensors is the choice of optical coupler, which is needed to match the momentum of an input light wave to the surface plasmons at a metal/dielectric interface. The most commonly used coupling method is the so-called Kretschmann-Raether configuration, whereby attenuated total internal reflection at the interface of a high refractive index prism is used to generate the matching conditions necessary to excite surface plasmons.[2] An alternative and increasingly attractive approach is one that exploits nanostructured surfaces to couple to surface plasmons.[3] Some examples of nanostructures used for SPR sensing include nano-hole arrays,[4] single nanometer-scale holes,[5] nanoslit arrays,[6] and various grating-type and diffractive nanostructures.[7] One of the most readily accessible nanostructures that can be used to excite surface plasmons are those based upon diffraction gratings.[8] Notably, the very first observation of surface plasmons was made in 1902 by Wood when studying a metallic diffraction grating.[9] Gratings are advantageous in that they are commercially available in a variety of forms, either as optical elements used for spectroscopy or as CDs, DVD and blue-ray discs. In addition, custom gratings can be readily fabricated via machining and laser-based interferometry techniques.[7, 10]

Grating-based SPR sensing has several key advantages compared to other SPR methods.[1c, 11]

Gratings represent an inherently information-rich substrate due to surface plasmons appearing in not only the directly reflected or transmitted peaks, but also in the various diffracted orders.[10a] In addition, the plasmon response is highly tunable based upon the size and shape of the grating topology. Indeed, changing the amplitude, shape or pitch of the grating profile has a dramatic effect on the wavelength and shape of the plasmon resonance.[7a, 12] Thus, this substrate represents a highly flexible and tunable platform for sensor development.

One of the challenges associated with grating-based SPR platforms involves the fact that the nature of this surface is complex and can lead to the simultaneous excitation of multiple surface plasmons, and overlap between those various modes. For example, more than one surface plasmon mode can be excited due to the opportunity for coupling to several diffracted orders from the grating interface.[13] In addition, the two-sided nature of grating couplers allows surface plasmons to be excited at both metal-dielectric interfaces. This means that surface plasmons can exist at both the "front" and "back" sides of the grating. Ultimately, the formation of multiple surface plasmon modes leads to the appearance of additional features and complexity in the optical response, which can complicate interpretation of this data. In order to address the added complexity of grating-coupled SPR, we describe the use of dispersion images to provide a detailed picture of surface plasmon excitation at a model metal-coated grating. An asymmetric grating comprised of a plastic/metal/ambient interface is constructed and analyzed via angle-scan transmission measurements. Various optical features in this response are analyzed in terms of the associated diffracted orders at the metal/dielectric interface to accurately identify the origin of these features. These data are also compared to results from optical modeling. The impact of a dielectric coating consisting of a multilayer Langmuir-Blodgett film is also examined in terms of the shifts (or lack thereof) of the various plasmon peaks.

5.3 Experimental Section

5.3.1 Materials and Reagent

Arachidic acid and chloroform were purchased from Sigma Aldrich (St. Louis, MO). All chemicals and reagents were used as received. Deionized water 3with electrical resistivity greater than 18 MΩ□cm was used during rinsing and cleaning procedures (NANOPure, Barnstead, Dubuque, IA). Recordable digital versatile discs (DVD-R, 4.7GB) were purchased from Inkjet Art Solutions (Salt Lake City, UT). Gold (99.999%) and Tungsten wire baskets were purchased from Ted Pella, Inc. (Redding, CA).

5.3.2 Grating Construction

Gratings substrates were prepared from commercial DVD-Rs, which were split with a razor blade, cleaned, and then coated with a thin layer of gold, as described previously.[7c] Gold was coated to a thickness of ~ 40 nm using a thermal metal evaporator (Benchtop Turbo III, Denton Vacuum). The metal thickness was verified during deposition using a quartz crystal thickness monitor and confirmed post-deposition using a combination of atomic force microscopy and optical absorbance measurements.

5.3.3 Langmuir-Blodgett Deposition

Multilayer films of arachidic acid were deposited onto the gold-coated grating by Langmuir-Blodgett deposition using a computer-controlled deposition trough (Model 610, Nima Technologies). Films of arachidic acid were spread onto a pure water subphase using chloroform as a solvent. Following solvent evaporation, the surface film was compressed to a surface pressure of ~ 15 mN m^{-1}. Films were then formed on the grating substrates by automated dip-

coating. Gratings were translated at a rate of 1 mm min^{-1} through the air/water interface and the arachidic acid was replenished between deposition strokes to maintain a constant surface pressure. Film thicknesses were confirmed using a combination of quartz crystal gravimetry, ellipsometry, and atomic force microscopy.

5.3.4 Atomic Force Microscope (AFM) Imaging

AFM imaging of the sample surfaces was performed with a Dimension 3100 scanning probe microscope and a Nanoscope IV controller (Veeco Metrology, LLC, Santa Barbara, CA). Imaging was performed in tapping mode using silicon TESP7 AFM tips (Veeco Metrology, LLC, Santa Barbara, CA) with a spring constant of ~70 N m–1 and a resonance frequency of ~280 kHz.

5.3.5 Optical Characterization

All optical transmission measurements were carried out using a custom-built optical system (Fig.S.1, Supporting Information). White light from a tungsten- halogen source (Model LS1, Ocean Optics, Dunedin, FL) was collimated using a convex lens with focal length of 150 mm (Newport Corp.). The resulting beam passed through a Glan Thompson polarizer before illuminating the grating sample through a 2 mm diameter aperture. The sample was mounted on a motorized, rotating sample stage (Model PRM1Z8, Thorlabs) for automated alignment and rotation. The transmitted light was collected using a 600 μm optical fiber and recorded with a fiber optic spectrometer (SD2000, Ocean Optics, Inc., Dunedin, FL). Dispersion images were acquired by rotating the sample using the motorized sample stage, and synchronizing this rotation with the acquisition of transmission spectra through the spectrometer using a custom-built Labview code.

5.3.6 Optical Modeling

The rigorously coupled wave analysis (RCWA) method was used to model the optical response of the grating with various coated layers, as described previously.[14] Briefly, diffraction efficiencies were computed for transmitted and reflected light using both transverse magnetic (TM) and transverse electric (TE) incident light as a function of wavelength and angle of incidence. A custom-built code was written in Matlab to perform the computations. The grating geometry was approximated based upon fitting AFM images of the grating surface. The surface profile of the grating was represented using two-different shapes, one with a sawtooth profile and the other with a more segmented shape, and both having a pitch of 700 nm and amplitude of 120 nm. Wavelength-dependent refractive index values used in the computations included published values for gold.[15] The polycarbonate substrate was modeled using the Sellmeier equation.[16]

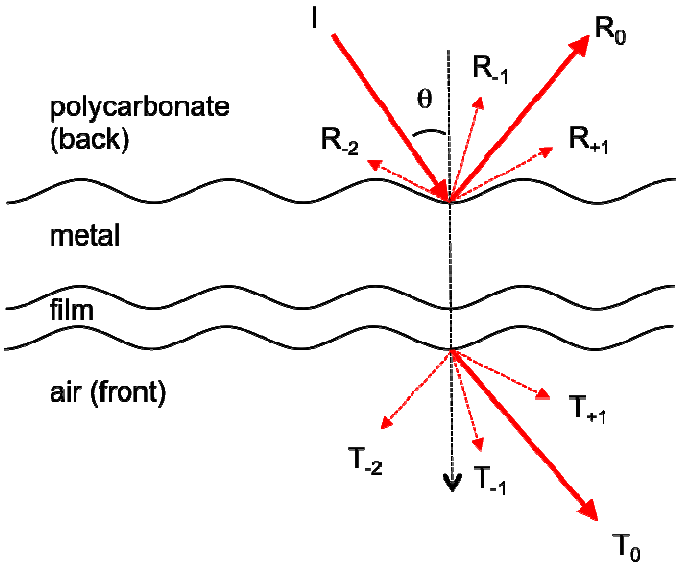

Scheme 1 Schematic of grating showing air/film/metal/polycarbonate interfaces and primary reflected (R_i) and transmitted (T_i) modes from several diffracted orders at the front (metal/film) and back (metal/polycarbonate) grating interfaces.

5.4 Results and Discussion

A representative sample geometry used for grating-coupled surface plasmon resonance (GC- SPR) is depicted in Scheme 1. A typical sample consists of an optically-transparent substrate (polycarbonate, in this case) on which the grating topology is molded. A thin gold film is coated on one side of the grating in order to support the generation of surface plasmon polaritons (SPPs) at the metal-dielectric interfaces. For sensing applications, a thin film or adsorbate is anchored at the metal/air interface, which changes the local dielectric environment near the metal surface and perturbs the resonance conditions for the SPPs. This generally produces a red-shift in the resonance conditions that can be observed through changes in the transmitted or reflected light.[2a] Coupling to SPPs can occur via several different grating orders on both back (gold/polycarbonate) and front (gold/film/air) sides of the grating interface and can be observed in both transmission (T) and reflection (R) modes, as depicted in Scheme 1.

Grating-coupled SPR has been shown to produce enhanced optical transmission at specific wavelengths associated with a matching of the grating wavevector with that of SPPs at the metal/dielectric interface.[7c] An example of this enhancement is shown in Fig.1, which depicts a series of p-polarized transmission spectra for light incident on a gold-coated grating as a function of angle of incidence. An enhanced transmission peak is evident at ~750 nm for directly transmitted light ($\theta = 0°$). Changing the angle of incidence shifts the location of the

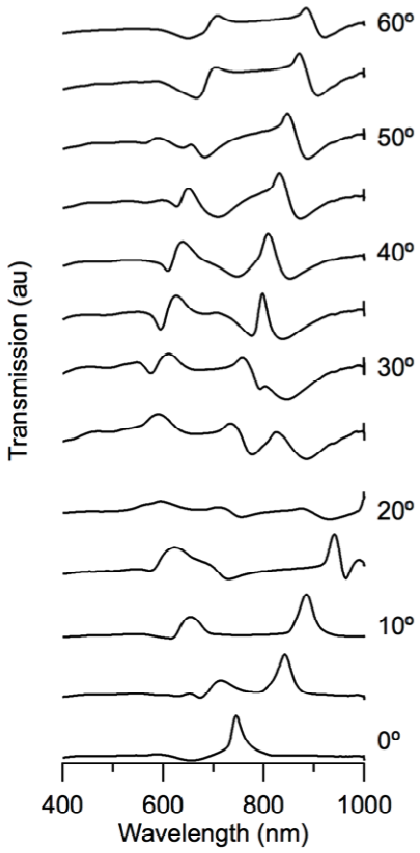

Figure 1 Experimental transmission spectra (p-polarized light) through gold-coated (40 nm) DVD grating as a function of wavelength and angle of incidence.

enhanced transmission peak, as well as producing additional features in the transmission spectra. Indeed, several of the peaks appearing in Fig.1 can be indexed according to specific diffracted orders coupling to SPPs in the metal film, and the change in these peak positions with angle of incidence has been previously noted.[7c, 17] A closer look at the various transmission spectra shows fine structure, however, that is difficult to immediately identify.

A more complete picture of the transmission response, and greater detail about the subtle features observed in the spectra, can be more readily seen in the form of a dispersion image (Fig.2A). This image represents a dense compilation of experimentally measured spectra taken over a range of incident angles. These data were acquired by recording p-polarized transmission spectra every 0.5° while rotating the sample grating about its axis using a computer controlled rotation stage. The image was normalized by dividing it by the s-polarized transmission spectra of a flat, gold-coated surface with the same gold thickness. Within this dispersion image appears a series of crossing lines of either enhanced (light) or suppressed (dark) intensity. At the center of the image, for example, is a pair of light-colored features in the form of an x-pattern associated with the most intense, enhanced light transmission. These features correspond to SPPs generated at the gold/air interface through coupling to the grating's ± 1 diffracted orders (the +1 order has a negative slope and the -1 order has a positive slope).[7c] Additional light and dark lines are also seen throughout the image. These additional features are also SPPs, which are generated through coupling to various other diffracted orders at either the front (gold/air) or the back (gold/polycarbonate) sides of the grating (*vide infra*).

Identifying the specific location (front or back of grating) and diffracted orders associated

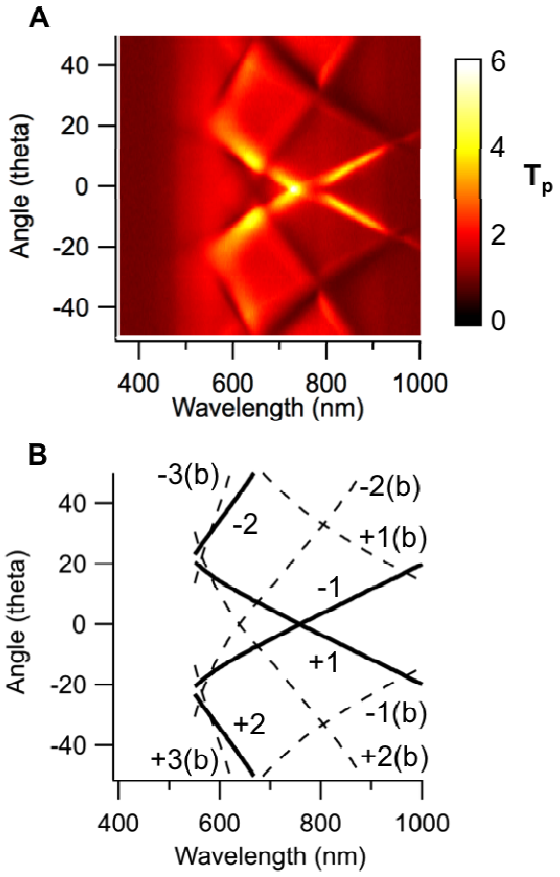

Figure 2 (A) Dispersion image showing a compilation of experimental p-polarized transmission data (T_p) versus wavelength and angle of incidence through a gold- coated grating. The data has been normalized by dividing by the s-polarized transmission spectra of a flat surface with the same gold thickness. (B) Calculated SPR matching conditions for gold-coated grating having a 700 nm pitch. The matching conditions and corresponding diffraction orders are identified with solid and dashed lines. All backside (gold/polycarbonate) diffraction features are identified with (b) and dashed lines. The remaining front side (gold/air) features are identified with solid lines.

with each of these features can be achieved by indexing them with respect to the grating (k_{gr}) and surface plasmon (k_{sp}) wavevectors. The matching condition between the SPP and a grating is given by:

$$k_{sp} = \frac{2\pi}{\lambda_0}\sqrt{\frac{\varepsilon_M^{'}\varepsilon_D}{\varepsilon_M^{'}+\varepsilon_D}} = \frac{2\pi}{\lambda_0}\sqrt{\varepsilon_D}\sin\theta_0 + m\frac{2\pi}{\Lambda} = k_{gr} \qquad (1)$$

where λ is the wavelength of light, ε'_M is the real value of the metal's dielectric constant, ε_D is the dielectric constant of the neighboring layer (polycarbonate or air), n is the refractive index of the incident medium (air), θ is angle of incidence, m is an integer (0, ±1, ±2, ...) indicating the diffracted order, and Λ is the grating pitch.[1b, 2a, 8] Using this formula, the dispersion relations for SPP matching in a gold film can be determined for the various diffracted orders. Fig.2B depicts these relations for several diffracted orders corresponding to the front (gold/air, solid lines) and back (gold/polycarbonate, dashed lines) of the grating. The primary front side feature of note is the matching associated with the +1 and -1 diffracted orders. As noted earlier, these correspond to the largest enhanced transmission features in the experimental dispersion image (Fig.2A). In addition, there are features associated with coupling to the ± 2 diffracted orders at the front side of the grating. These appear as enhanced transmission at larger angles and lower wavelengths in the experimental data. The majority of the other features in the dispersion images, which are primarily dark features, can be associated with SPPs generated at the back or polycarbonate/gold side of the grating (as noted by dashed lines in Fig.2B). All of these back-side SPPs appear as reduced transmission or valleys in the experimental dispersion images.

The various features associated with the front and back side SPPs can also be considered in terms of the overall dispersion relations as described in Eqn. (1). In particular,

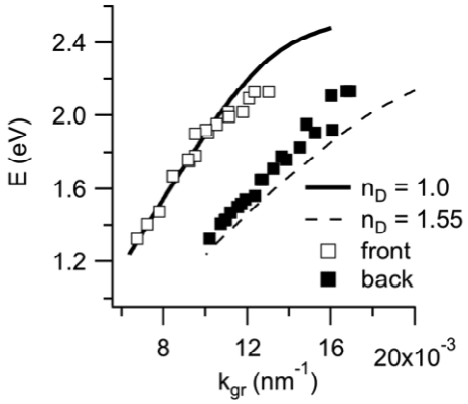

Figure 3 Plot of peak energy (E) versus grating wavevector (k_{gr}) for matching conditions identified in Fig.2.B for refractive index values of $n_D = 1$ (air, solid line) and 1.55 (polycarbonate, dashed line). Data points corresponding to front-side (open squares) and back-side (solid squares) features are also plotted.

if one plots the matching conditions for the SPPs in terms of the plasmon energy (in eV) versus the grating wavevector (in nm^{-1}), the front and back side features all collapse onto two curves, distinguished by the refractive index value of the material at the specific metal/dielectric interface. Fig.3 shows such a plot, where the calculated results from Fig. 2B have been recast in terms of the peak energy (E) versus the grating wavevector (k_{gr}).[18] All diffracted orders associated with SPPs at the metal/air interface collapse onto the line associated with the dielectric constant for air (n_D = 1, solid line), while all those associated with the metal/polycarbonate interface collapse onto the line associate with a refractive index of n_D ~1.55 (dashed line), which is approximately the value reported for polycarbonate in the visible spectrum.[16] In addition, when data from the light (open squares) and dark (filled squares) features in the experimental data in Fig.2A are plotted in Fig. 3, they all fall either on the front or back-side curves, corresponding to the refractive index of the nearest dielectric material.

Although the comparison between the SPP matching condition (Eqn. 1) and the experimental results showed good agreement in terms of feature location, subtle details in the experimental data, such as the intensity of the transmitted light or details of the regions where front and back-side features overlap, cannot be represented by this equation. In order to more fully explore the nature of the various features in the dispersion image, a simulation of the optical transmission through a model grating structure was performed. Two different grating shapes were examined. Both shapes are approximations of the measured profile of the grating surface (Fig. S.2, Supporting Information). The first modeled topology was a simple sawtooth profile having the same pitch and amplitude as the sample grating. The structure in

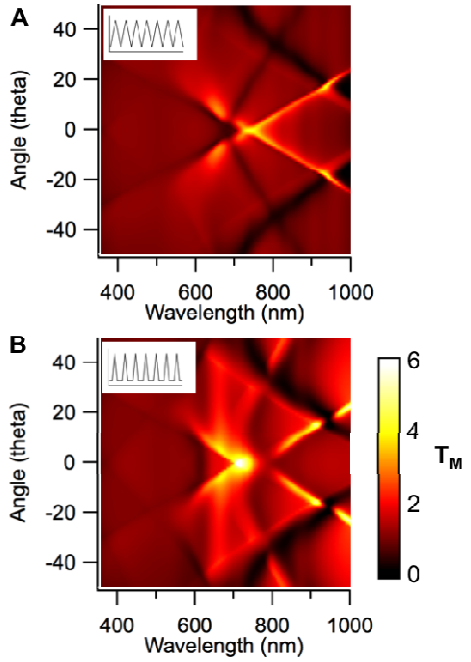

Figure 4 Computed dispersion images for transverse magnetic (T_M) light through two different grating profiles having a 700 nm pitch and 120 nm amplitude with a 40 nm gold layer: (A) sawtooth profile and (B) segmented profile. The surface profiles for each image are identified in the insets.

the optical model was constructed with a polycarbonate base ($n_D \sim 1.55$), a gold film with a thickness of 40 nm, and an ambient environment of air. A second profile was constructed with a sharper peaked shape to more closely approximate the experimental profile. Both the sawtooth and peaked profile are shown as insets in Fig.4.

The optical response of these gratings was computed using the rigorously coupled wave analysis (RCWA) method.[14] The results are shown for transverse magnetic (TM) polarized light through the grating structure, divided by transverse electric (TE) polarized light through a flat, gold-coated surface. The upper image (Fig.4A) is for the sawtooth and the lower (Fig.4B) is for the peaked profile. The computed transmission images have numerous features in common with the experimental results (Fig.2A). Notably, the location and intensity of the bright crossing lines associated with the +/-1 diffracted peaks are in approximately the same location and exhibit a similar magnitude of enhancement (with $T_{M,max} \sim 5$). For the sawtooth profile (Fig.4A), the enhanced transmission features associated with the +/- 1 diffracted orders are continuous until they intersect with the +/- 2 back-side peaks at ~650 nm, where the intensity is extinguished. This behavior is also observed in the experimental data. However, in the experimental data, an additional drop in the light enhancement for the +/- 1 order features is observed at ~750 nm, where a vertical energy gap appears. This energy gap is consistent with behavior associated with coupling of SPPs to higher order harmonics in the surface periodicity (more precisely, a surface possessing an additional grating wavevector at twice that coupling to the SPP), as has been reported previously.[19] Notably, if one closely examines the model results from the peaked profile (Fig.4B), which possesses a more significant harmonic component in its profile, a similar energy gap also appears at ~750 nm. In addition to these features, the location and orientation

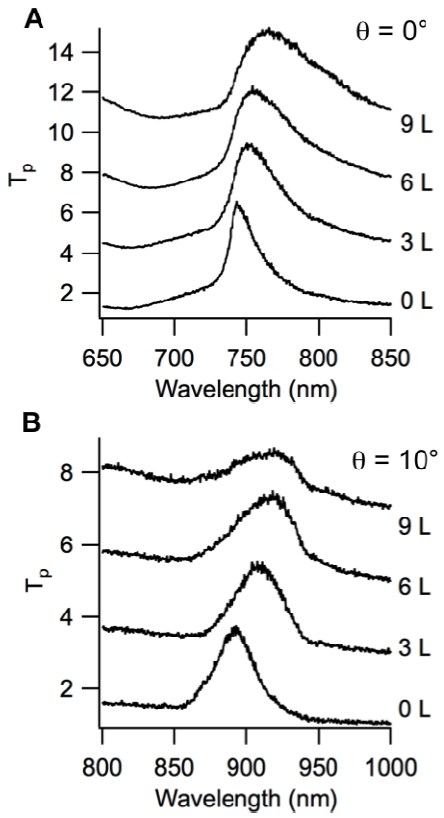

Figure 5 Transmission spectra measured at an angle of incidence of (A) 0° and (B) 10° through gold-coated grating with Langmuir-Blodgett films of arachidic acid at 0, 3, 6 and 9 layer (L) thicknesses. The spectra have been offset in the vertical direction for clarity.

of the other peaks and valleys in the simulated images are quite similar to the measured image. Notably, all of these features can be associated with the excitation of SPPs at either the front (gold/air) or back (gold/polycarbonate) sides of the grating. Of these modeled responses, the experimental results more closely follow the behavior of the peaked profile in Fig.4B.

We, and others, have previously demonstrated that enhanced transmission peaks associated with grating-coupled surface plasmon resonance can be used to quantify the thickness of adsorbed thin films or changing dielectric media.[7c, 13, 17, 20] In order to investigate the impact of thin, coated films on the various transmission features observed in Fig.2, we constructed multilayer films of arachidic acid. Langmuir-Blodgett film deposition was used in order to controllably fabricate films of varying thickness. Arachidic acid was spread onto a deionized water subphase from a chloroform solution, and deposited at a fixed film pressure (Fig.S.3, Supporting Information). The arachidic acid monolayer was compressed to a deposition pressure of ~ 15 mN m^{-1}. Film coating was then performed by dipping the grating substrate through the arachidic acid monolayer at air/water interface. Multiple layers were formed by sequential dipping at this film pressure.

The typical response of the enhanced transmission peaks to increasing adsorbed film thickness is to produce a red-shift in the peak positions. This is clearly seen for the transmission peak associated with the -1 order (Fig.5) at two different angles of incidence. At $\theta = 0°$, films of 0, 3, 6 and 9 layers of arachidic acid are shown, where each layer corresponds to a bilayer of arachidic acid that forms during a dipping stroke down and back up through the monolayer. The addition of these films produces a red-shifting and broadening of the transmission peak (Fig.5A). A similar red-shifting and broadening is seen

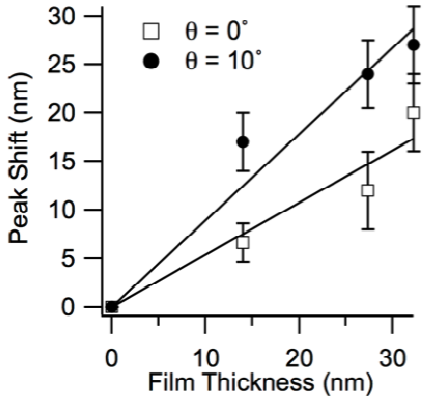

Figure 6 Comparison of the shift in enhanced transmission peaks (from Fig.5) versus film thicknesses (as determined by spectroscopic ellipsometry) at angles of incidence of 0° and 10° for arachidic acid multilayers.

when this peak is measured at an incident angle of θ =10° (Fig.5B). A quantitative comparison of the peak shifts is illustrated in Fig.6, where the shift in the transmission peak position is plotted versus the film thickness. The film thicknesses were measured using ellipsometry. According to the ellipsometry results, the average thickness of the arachidic acid layer formed during a single down/up dipping stroke is ~ 4.5 nm, which is consistent with a bilayer of arachidic acid being deposited (a Y-type film).[21] Literature reports for a single arachidic acid layer give a thickness of between 2.2 and 2.8 nm,[22] which is approximately half the measured thickness and consistent with the formation of a bilayer. The thickness sensitivity of the plasmon peak shifts are ~0.55 nm shift/nm thickness at θ =0° and ~0.9 nm shift/nm thickness at θ =10°. These values are similar to previous measurements of thin 11 organic films,[7c, 13] and consistent with the fact that the sensitivity of the peak shifts increases at higher resonant wavelengths, which is the case for the higher sensitivity of the m = -1 peak at θ =10° versus at θ =0°.

Although the enhanced transmission peak associated with the -1 diffracted order red-shifts in the presence of an adsorbed film as one would expect, the other transmission features appearing throughout the transmission spectrum do not all behave similarly. A more complete picture of the transmission response can be seen with dispersion images of the surface with various film coatings. The shifts (and lack thereof) can be seen most clearly through the use of subtraction images. Fig.7 depicts two such images. Fig.7A shows an image created by subtracting the bare substrate image (Fig.6A) from the dispersion image after deposition of a 3L film (Fig.6B). This subtraction image will show high contrast, and a blue followed by yellow/red stripes where there has been a red shift in the peaks. Fig.7A shows these features primarily along the +/- 1 diffracted orders associated with the front side

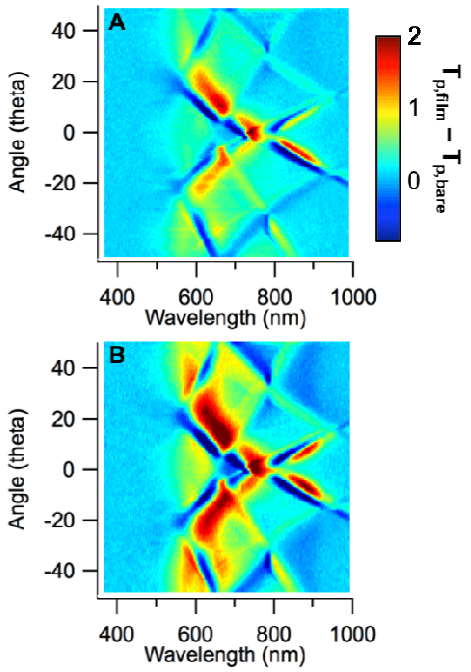

Figure 7 Difference ($T_{p,film} - T_{p,bare}$) images created by taking dispersions images of the (A) 3 layer and (B) 6 layer films and subtracting the bare or uncoated grating. High contrast (red to blue) regions on this image indicate significant red-shifting of the associated dispersion features on the film-coated samples.

of the grating. A smaller, yet still noticeable, contrast change is seen at the +/- 2 front side peaks. Very little change is seen at the back-side peaks. This behavior is even more evident when plotting the subtraction image created from the dispersion image from the 6 layer film minus the bare substrate (Fig.7B). In this image, strong blue to red contrast is observed along the +/- 1 and +/- 2 front side features, with a much smaller change along the back-side features. An explanation for this behavior, and a more complete picture of the origins and nature of the features in these data can be obtained by modeling the optical response of this grating structure.

The influence of a film on the front side (gold/air) interface on the location of the various SPP features can also be more clearly seen by using the matching relation in Eqn. (1). The addition of a film on the front gold/air interface has the effect of increasing the effective refractive index at that interface from a value of that for air ($n_D = 1$), to a larger value. If one considers how that behavior impacts the SPP coupling conditions as described by Eqn.1, it produces a red-shift in all of the SPPs. This is shown in Fig.8A, which plots the front side peaks associated with the +/- 1 and +/- 2 diffracted orders for refractive index values of 1, 1.1, and 1.2 for the neighboring dielectric. All of these peaks red-shift with increasing refractive index value. When plotted as energy (E) versus grating wavevector (k_{gr}) (Fig.8B), the result of a changing dielectric constant is the appearance of a single new dispersion curve for each refractive index. Thus, the effect of a film is to increase the effective refractive index of the air/gold interface, which shifts the entire set of front-side plasmon peaks to longer wavelengths (or lower energies). Notably, under conditions where the plasmon decay length within the metal is small, such as due to the lack of optical symmetry at the front and back metal surfaces, the plasmons that form at the front and back side do not communicate. In this circumstance, the back side peaks would be

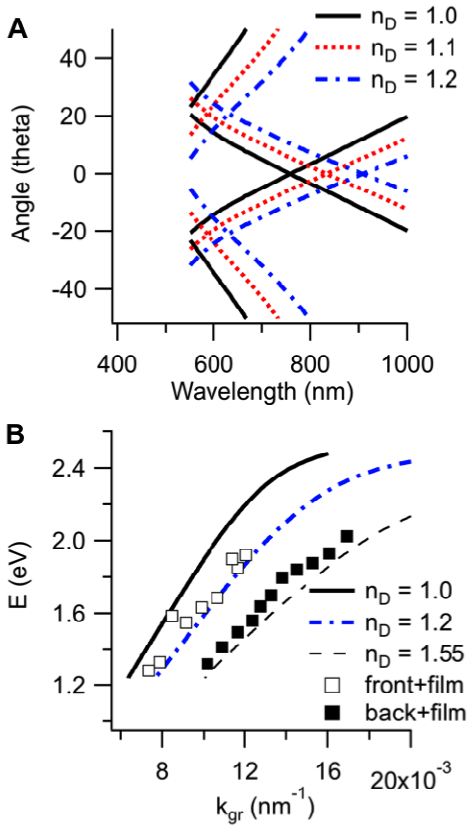

Figure 8 (A) Calculated SPR matching conditions for front-side peaks as a function refractive index of the surrounding dielectric (n_D). (B) Plot of peak energy versus grating wavevector for refractive index values of 1.0 (air), 1.2, and 1.55 (polycarbonate). Data points for 12 L arachidic acid film on grating for front-side (open squares) and back-side (solid squares) features are also shown.

unaffected by the presence of a film on the front side of the grating, which would support the observed behavior where the back side peaks do not appear to shift in the presence of the arachidic acid films. Indeed, if one considers experimental results from a 12 L arachidic acid film, the front and back side features exhibit this behavior. In Fig. 8B, the positions of several front side peaks are plotted (open squares) and they all fall nearly along the curve for an effective refractive index of $n_D = 1.2$, as opposed to falling on the $n_D = 1.0$ line without the film. In contrast, the back-side peaks (filled squares) still remain near the line corresponding to the higher refractive index of the polycarbonate ($n_D = 1.55$). Notably, there are conditions, such as in the presence of a very thin metal layer or with a symmetric that can support long-range plasmons, where the front and back sides SPPs would interact and both would be impacted by changes in the dielectric environment on the other side of the grating. However, that does not appear to be the case here.

5.5 Conclusions

Surface plasmon resonance sensors using nanostructured surfaces, including diffraction gratings, have become an increasingly popular alternative to the more traditional prism-type couplers. The ability to fabricate nanostructures with well-defined surface topologies allows for fine-tuning of the optical response, and a greater ability to control the nature of the coupling to surface plasmons. With this added control, however, comes an added complexity. For example, multiple features, including multiple peaks and valleys, often appear in the optical response of grating- coupled SPR. These additional features are associated with the excitation of several surface plasmon modes, which can be due to the two-sided nature of the grating and also to excitation via higher diffracted orders.

This study focused on understanding the complex optical response that can result from a grating-coupler scheme for surface plasmon resonance sensing. For transmission-based sensing, surface plasmons existing at both the front and back sides of the grating can appear as features, either peaks or valleys, in the transmission spectrum. Interpretation of these features can be assisted through the use of dispersion images, which plot the transmission spectrum as a function of angle of incidence. Combined with optical modeling, we have shown how the features in these dispersion images can be directly indexed to specific plasmon modes, including the associated diffraction order and the interface (front or back side) that the surface plasmon exists. In addition, the sensitivity of these features to changes in the local refractive index, such as via the deposition of thin films, is highly dependent upon the location of the refractive index change. For the deposition of thin films on the metal/ambient or "front-side" of the grating, only the front side features exhibited the characteristic red-shifting. Features in the optical spectrum associated with metal/substrate interface or "back-side" of the grating did not shift in the presence of film formation on the grating's front side. For an asymmetric grating, like the one used here, this would be the general behavior. However, for a grating in which the wavefunctions of the surface plasmons at the front and back side interfaces overlapped, such as with a symmetric grating or for one with an exceedingly thin metal film, one would expect a more complex response.

5.6 Acknowledgement

This work was funded by the National Science Foundation (CHE 0809509), the National Institutes of Health (R44 RR023763- 02), and the W. M. Keck Foundation through the W. M. Keck Laboratory for High Throughput Atom-Scale Analysis at Iowa State University.

5.7 References

(1) (a) Homola, J. *Anal. Bioanal. Chem.* **2003**, *377*, 528-539. (b) Homola, J. *Chem. Rev.* **2008**, *108*, 462-493. (c) Homola, J.; Yee, S. S.; Gauglitz, G. *Sens. Actuators, B* **1999**, *54*, 3-15.

(2) (a) Knoll, W. *Ann. Rev. Phys. Chem.* **1998**, *49*, 569-638. (b) Kretschmann, E.; Raether, H. *Z. Naturforsch., A: Phys. Sci.* **1968**, *A 23*, 2135-&.

(3) (a) Barnes, W. L.; Dereux, A.; Ebbesen, T. W. *Nature* **2003**, *424*, 824-830.(b) Stewart, M. E.; Anderton, C. R.; Thompson, L. B.; Maria, J.; Gray, S. K.; Rogers, J. A.; Nuzzo, R. G. *Chem. Rev.* **2008**, *108*, 494-521.

(4) (a) Brolo, A. G.; Arctander, E.; Gordon, R.; Leathem, B.; Kavanagh, K. L. *Nano Lett.* **2004**, *4*, 2015-2018. (b) Liu, Y.; Bishop, J.; Williams, L.; Blair, S.; Herron, J. *Nanotech.* **2004**, *15*, 1368-1374.

(5) Rindzevicius, T.; Alaverdyan, Y.; Dahlin, A.; Hook, F.; Sutherland, D. S.; Kall, M. *Nano Lett.* **2005**, *5*, 2335-2339.

(6) Jung, Y. S.; Sun, Z.; Wuenschell, J.; Kim, H. K.; Kaur, P.; Wang, L.; Waldeck, D. *Appl. Phys. Lett.* **2006**, *88*.

(7) (a) Adam, P.; Dostalek, J.; Homola, J. *Sens. Actuators, B* **2006**, *113*, 774-781. (b) Singh, B. K.; Hillier, A. C. *Anal. Chem.* **2006**, *78*, 2009-2018. (c) Singh, B. K.; Hillier, A. C. *Anal. Chem.* **2008**, *80*, 3803-3810. (d) Tian, S. J.; Armstrong, N. R.; Knoll, W. *Langmuir* **2005**, *21*, 4656-4660.(e) Yu, F.; Tian, S. J.; Yao, D. F.; Knoll, W. *Anal. Chem.* **2004**, *76*, 3530-3535.

(8) Raether, H., *Surface plasmons on smooth and rough surfaces and on gratings*. Springer-Verlag: Berlin ; New York, 1988; p x, 136 p.

(9) (a) Wood, R. W. *Proc. Phys. Soc. London* **1902**, *18*, 269. (b) Wood, R. W. *Phys. Rev.* **1935**, *48*, 928-936.

16(10) (a) Dostalek, J.; Homola, J.; Miler, M. *Sens. Actuators, B* **2005**, *107*, 154-161. (b) Hutley, M. C., *Diffraction Gratings*. Academic Press: London, 1982.

(11) Dostalek, J.; Homola, J. *Sens. Actuators, B* **2008**, *129*, 303-310.

(12) (a) Kitson, S. C.; Barnes, W. L.; Bradberry, G. W.; Sambles, J. R. *J. Appl. Phys.* **1996**, *79*, 7383-7385. (b) Zhang, N.; Schweiss, R.; Zong, Y.; Knoll, W. *Electrochim. Acta* **2006**, *52*, 2869-2875.

(13) Yeh, W.-H.; Kleingartner, J.; Hillier, A. C. *Anal. Chem.* **2010**, *82*, 4988-4993.

(14) (a) Lalanne, P.; Morris, G. M. *J. Opt. Soc. Am. A.* **1996**, *13*, 779-784.(b) Moharam, M. G.; Grann, E. B.; Pommet, D. A.; Gaylord, T. K. *J. Opt. Soc. Am. A.* **1995**, *12*, 1068-1076. (c) Moharam, M. G.; Pommet, D. A.; Grann, E. B.; Gaylord, T. K. *J. Opt. Soc. Am. A.* **1995**, *12*, 1077-1086. (15) Johnson, P. B.; Christy, R. W. *Phys. Rev. B* **1972**, *6*, 4370-4379. (16) Kasarova, S. N.; Sultanova, N. G.; Ivanov, C. D.; Nikolov, I. D. *Opt. Mater.* **2007**, *28*, 1481-1490. (17) Gurel, K.; Kaplan, B.; Guner, H.; Bayindir, M.; Dana, A. *Appl. Phys. Lett.* **2009**, *94*. (18) Andrew, P.; Barnes, W. L. *Science* **2004**, *306*, 1002-1005. (19) (a) Chen, Z.; Hooper, I. R.; Sambles, J. R. *J. Opt. A - Pure Appl. Op.* **2008**, *10*. (b) Barnes, W. L.; Preist, T. W.; Kitson, S. C.; Sambles, J. R. *Phys. Rev. B* **1996**, *54*, 6227-6244. (c) Barnes, W. L.; Preist, T. W.; Kitson, S. C.; Sambles, J. R.; Cotter, N. P. K.; Nash, D. J. *Phys. Rev. B* **1995**, *51*, 11164-11167. (d) Kitson, S. C.; Barnes, W. L.; Bradberry, G. W.; Sambles, J. R. *J. Appl. Phys.* **1996**, *79*, 7383-7385. (e) Fischer, B.; Fischer, T. M.; Knoll, W. *J. Appl. Phys.* **1994**, *75*, 1577-1581.

17

(20) (a) Baba, A.; Tada, K.; Janmanee, R.; Sriwichai, S.; Shinbo, K.; Kato, K.; Kaneko, F.; Phanichphant, S. *Adv. Funct. Mater.* **2012**, *22*, 4383-4388. (b) Dou, X.; Phillips, B. M.; Chung,

P.-Y.; Jiang, P. *Opt. Lett.* **2012**, *37*, 3681-3683. (c) Janmanee, R.; Baba, A.; Phanichphant, S.; Sriwichai, S.; Shinbo, K.; Kato, K.; Kaneko, F. *ACS Appl. Mater. Interfaces* **2012**, *4*, 4270-4275. (d) Monteiro, J. P.; Ferreira, J.; Sabat, R. G.; Rochon, P.; Leite Santos, M. J.; Girotto, E. M. *Sens. Actuators, B* **2012**, *174*, 270-273. (e) Yeh, W.-H.; Petefish, J. W.; Hillier, A. C. *Anal. Chem.* **2011**, *83*, 6047-6053. (f) Nazarova, D.; Mednikarov, B.; Sharlandjiev, P. *Appl. Opt.* **2007**, *46*, 8250-8255.

(21) Kurnaz, M. L.; Schwartz, D. K. *J. Phys. Chem.* **1996**, *100*, 11113-11119.

(22) Viswanathan, R.; Schwartz, D. K.; Garnaes, J.; Zasadzinski, J. A. N. *Langmuir* **1992**, *8*, 1603-1607.

CHAPTER 6 TUNING AND OPTIMIZING SURFACE PLASMON RESONANCE-ENHANCED TRANSMISSION THROUGH A MULTI-AMPLITUDE GRATING

An article prepared for Analytical Chemistry

6.1 Abstract

We report the fabrication and testing of enhanced transmission through a multi-amplitude grating. This grating has a constant pitch but varying amplitude along its surface. A series of enhanced transmission spectra are collected at several positions of the grating. The magnitude of the enhanced transmission peaks varies as the amplitudes of the grating varies. Maximum magnitude of transmission peaks is observed as the amplitude has a critical value. Beyond or below the critical value, the magnitude of transmission peaks decreases. We also found that transmission enhancements are strongly affected by the diffraction efficiencies. A maximum enhancement is observed as diffraction efficiency is largest where amplitude reaches the critical value. The experimental results are then compared to the simulation.

6.2 Introduction

Metal-coated nanostructured surfaces induce surface plasmons when p-polarized light interacts with free electrons on the surface. Enhanced transmission is one of optical responses from SPR and has gained increasingly interest recently.[1, 2] Considerable research has been conducted to obtain enhanced transmission by using different nanoscaled and patterned surfaces, such as nanohole arrays,[3] nanoslit arrays,[4] and diffraction gratings.[5, 6]

Diffraction gratings are an attractive SPR platform in that they are inexpensive and commercially available. For example, CDs and DVDs discs are commercially low-cost diffraction gratings and have been used as sensitive SPR sensors.[6-8] Another advantage of diffraction gratings is the tunable optical behavior of SPs. That is, the optical responses of enhanced transmission can be tuned by changing the topology of gratings. The shape, pitch, and amplitude of the grating impact the behavior of SPs. We have previously demonstrated that a chirped diffraction grating that has varying topology along its surface posses rich information about SPR.[5] The wavelength and magnitude of transmission peaks are drastically impacted by the pitch and amplitude of the grating.

By using interference lithography, the topology of the gratings can be precisely dialed into desired pitch and amplitude values.[9-11] The period of the intensity modulation defines the pitch of the grating. The amplitude of the gratings can be tuned by the exposure dose of laser on the photoresist or by the development time in the lithography process. Lloyd's mirror is one common configuration of interference lithography.[12] Lloyd's mirror is advantageous in that the setup is simple and large area of a grating can be readily fabricated.

In this work, enhanced transmission is demonstrated by utilizing a diffraction grating that has a chirped amplitude profile. We illustrate how the amplitudes of the grating impact the magnitudes of the enhanced transmission peaks. Several amplitudes are fabricated by changing the development time of the positive photoresist in the lithography procedure. An optically transparent replica of the grating is fabricated by using a procedure in our previous work. A series of transmission spectra through the silver-coated grating at different positions are collected and the experimental results are then compared to the simulation and a precise mechanism is proposed to produce the maximum transmission enhancement.

6.3 Experimental Section

6.3.1 Material and Reagents

Microposit S1813 Positive photoresist and Microposit 352 developer was from Rohm and Haas Electronic Materials LLC. UV curable photopolymer (NOA 61, Edmund Optics), polydimethylsiloxane (SYLGARD 182, Dow Corning), sulfuric acid and hydrogen peroxide (30%) (Sigma Aldrich) were used as received. Glass slides were purchased from Fisher Scientific (Pittsburgh, PA). Silver (99.999%) and tungsten wire baskets were purchased from Ted Pella, Inc. (Redding, CA). Deionized water with electrical resistivity greater than 18 MΩ·cm was used during rinsing and cleaning procedures (NANOPure, Barnstead, Dubuque, IA).

6.3.2 Grating Construction

Fresh piranha solution (mixture of 3:1 concentrated sulfuric acid to 30% hydrogen peroxide solution) was used to clean the glass slides. Caution: piranha solution reacts violently with organic compounds! Following cleaning, the glass slides were rinsed vigorously with deionized water and dried under nitrogen. Glass slides were prebaked at 100 °C for 3 minutes to remove moisture before photoresist deposition. After prebaking, a glass slide was transferred to the stage of a spin coater (WS-650MZ-23NPP, Laurell Technology Corp.) and then positive photoresist was spin cast to form a thin film onto the glass slide. The rotation speed of the stage was first set at 500 rpm for 5 seconds. The speed was then increased to 4000 rpm for 40 seconds. The acceleration time between these two steps is less than 3 seconds. Following deposition, the film-coated slide was baked at 90 °C for 3 minutes to accelerate solvent evaporation. After baking, the slide was transferred to the sample holder of Lloyd's mirror (Scheme 1). [13] Expended laser beam (405 nm) illuminates the sample

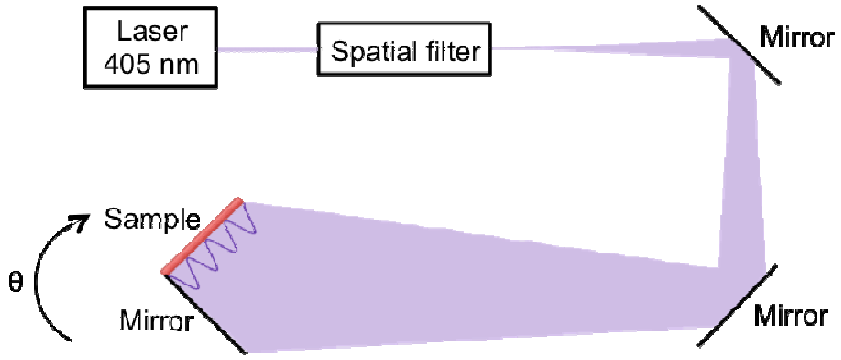

Scheme 1 The setup of Lloyd's configuration. A laser with a wavelength at 405 nm is used, and a spatial filter is used to expand laser beam. After passing through a pinhole, the expended laser beam hits both sample and mirror and via interference creates modulated sinusoidal intensity profile on the surface of the sample.

holder and the reflection from both the photoresist and the mirror forms an interference pattern on the surface of the photoresist. The interference pattern has a sinusoidal modulated intensity profile. The period of the intensity profile is controlled by the incident angle. In our case, the incident angle is ~ 19° and the period is ~ 624 nm. The period of the profile then defines the pitch of exposed modulation which forms on the photoresist. After laser exposure, the sample was postbaked at 110 °C for 3 minutes to improve the adhesion between photoresist and slides. Following postbaking, the sample was transferred to the mount of motor arm. The motor arm was controlled by a custom-built LabVIEW code. The developing process is shown in Scheme 2. The sample was dipped into the developer with a step distance = 2 mm and the time interval between each step is 30 second. As the number of steps increases the development time becomes longer. Longer development time leads to larger penetration depth of exposed photoresist and thus forms larger amplitude. By varying developing time as shown in Scheme 2, we obtained the chirped amplitude diffraction grating. After development, the grating was rinse vigorously with deionized water and dried under nitrogen.

A replicate of the multi-amplitude grating was obtained by using procedures described in our previous work.[5] Briefly, PDMS was used to form a stamp that has the topology of chirped amplitude grating. A liquid photopolymer (NOA 61, Edmund Optics) was applied on the polydimethylsiloxane (PDMS) stamp a nd cured under UV light. By peeling off the PDMS stamp, a transparent rigid grating was obtained. The samples was subsequently placed in a vacuum chamber (model Bench Top Turbo III, Denton Vacuum, Moorestown, NJ) for deposition of □40 nm of silver by resistive heating from a tungsten wire basket at a rate of 0.1 Å s^{-1} and a pressure of $<10^{-5}$ Torr.

6.3.3 Atomic Force Microscopy (AFM) Imaging

AFM imaging of the sample surfaces was performed with a Dimension 3100 scanning probe microscope and a Nanoscope IV controller (Veeco Metrology, LLC, Santa Barbara, CA). Imaging was performed in tapping mode using silicon TESP7 AFM tips (Veeco Metrology) with a spring constant of □70 N m−1 and a resonance frequency of □280 kHz.

6.3.4 Optical Characterization

All optical transmission measurements were carried out using a custom-built optical system.[8] White light from a tungsten-halogen source (Model LS1, Ocean Optics, Dunedin, FL) was collimated using a convex lens with focal length of 150 mm (Newport Corp.). The resulting beam passed through a Glan Thompson polarizer before illuminating the grating sample through a 2 mm diameter aperture. The transmitted light was collected using a 600 μm optical fiber and recorded with a fiber optic spectrometer (SD2000, Ocean Optics, Inc., Dunedin, FL).

6.3.5 Optical Modeling

A commercial software, PCGrate, was used to model the optical responses from the grating having different amplitudes. Briefly, diffraction efficiencies were computed for transmitted and reflected light using both transverse magnetic (TM) and transverse electric (TE) incident light as a function of wavelength and angle of incidence. The grating geometry was approximated on the basis of fitting AFM images of the grating surface. Wavelength-dependent refractive index values used in the computations included published values for silver.[13] The polycarbonate substrate was modeled using the Sellmeier equation.[14]

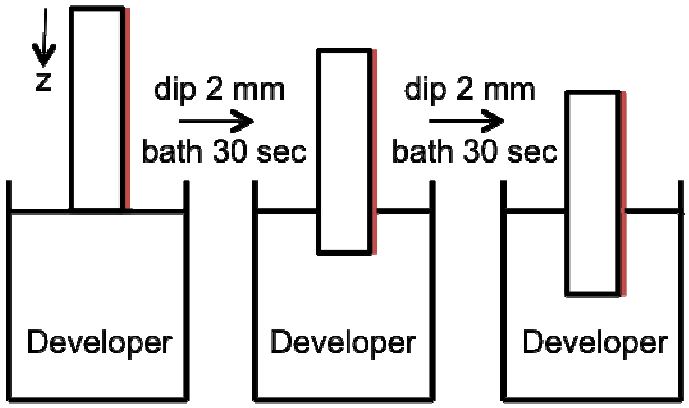

Scheme 2 Illustration of the fabrication of a chirped amplitude grating by increasing development time with time increment = 30 seconds. Positive photoresist is spin cast on a glass slide. After exposed to laser, the sample is mounted onto a motor stage and the stage is operated via custom-built Labview code to control dipping distance and duration of incubation. Larger amplitude is obtained as the development time increases.

6.4 Results and Discussion

Enhanced transmission is an optical phenomenon excited by surface plasmon resonance (SPR) as p-polarized light passes through metal-coated nanostructured substrates. [2] Diffraction gratings are one of these substrates used to obtain enhanced transmission.[6] The optical behaviors of enhanced transmission peaks can be tuned by the surface topology of diffraction gratings. In our previous work, we illustrated that various topologies on a chirped diffraction grating impacts both the wavelength and magnitude of transmission peaks.[5]

The wavelengths of the transmission peaks can be deduced by considering the momentum matching condition between the wavevector of SPs with that of p-polarized incident light interacting with the grating. The momentum matching condition can be described by the analytical solution from Maxwell's equations,

$$k_{SP} = \frac{2\pi}{\lambda}\sqrt{\frac{\varepsilon'_M \varepsilon_D}{\varepsilon'_M + \varepsilon_D}} = \frac{2\pi}{\lambda} n \sin\theta + m\frac{2\pi}{\Lambda} = k_{gr} \qquad (1)$$

where where λ is the wavelength of light, ε'_M is the real part of the metal's dielectric constant, ε_D is the dielectric constant of the neighboring layer (polycarbonate or air), n is the refractive index of the incident medium (air), θ is angle of incidence, m is an integer (0, ±1, ±2, ...) indicating the diffracted order, and Λ is the grating pitch It is evident that at $\theta = 0°$ the wavelength of transmission peaks tracks with the pitch of diffraction gratings. However, Eqn. (1) does not describe how other topology features, such as amplitudes of gratings,

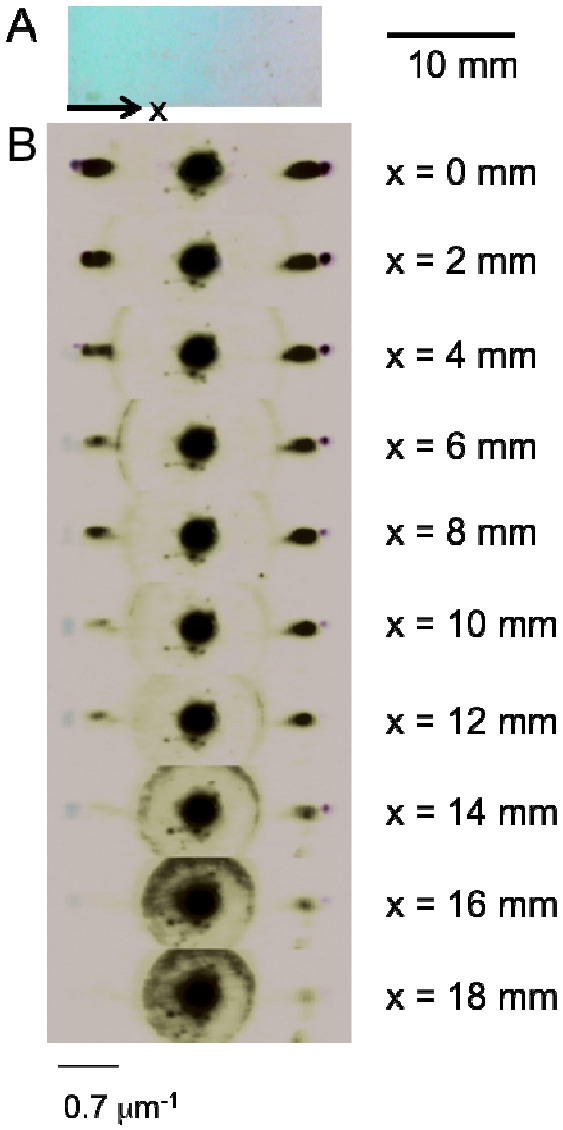

Figure 1 (A) An optical image showing reflection from a silver-coated chirped amplitude grating. The x-axis is used to denote the spatial positions where diffraction images are taken (see below). (B) Optical diffraction images acquired at various *x*-positions along the center of the diffraction grating. An optical microscope with a Bertend lenses attachment is used to obtains the images.

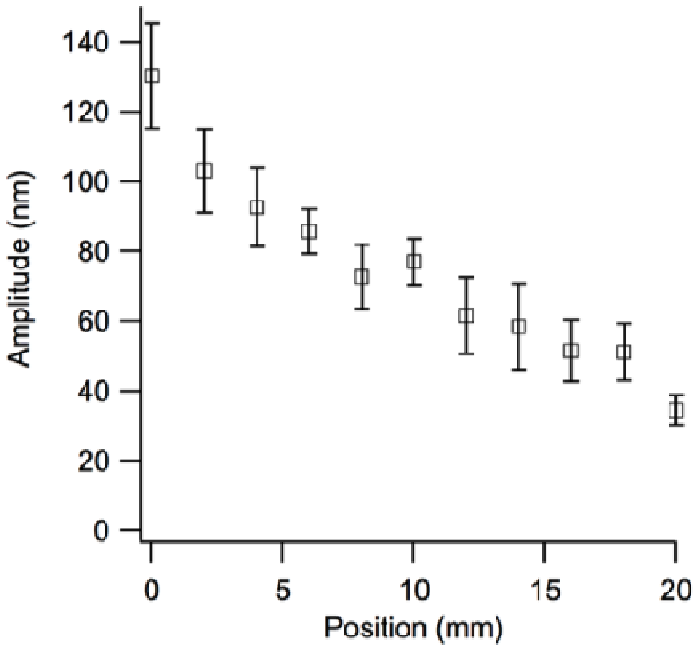

Figure 2 Surface topology of silver-coated chirped amplitude grating at x = 6 mm. (A) AFM image of chirped amplitude grating. (B) Cross sectional profile of chirped amplitude grating at x = 6 mm. The grating has an averaged pitch ~ 624 nm.

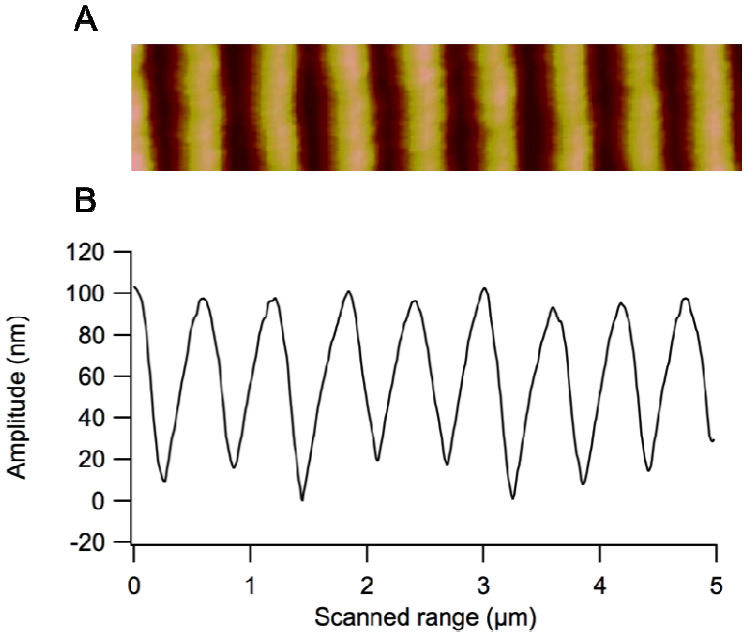

Figure 3 Amplitudes of the chirped grating along its spatial position. The amplitudes and error bars are calculated by analyzing AFM images. The spatial position corresponds to x-axis in Figure 1.

impact the optical responses of transmission peaks. For example, no information can be acquired from Eqn. (1) to predict the magnitude of the peaks. To understand more about how the amplitudes impact transmission peaks, we fabricated a chirped amplitude grating that has a fixed pitch but the amplitudes vary along its spatial position. Fig 1(A) displays a picture of the silver-coated chirped amplitude grating. The blue color from reflection from the grating has an intensity gradient. Strongest blue color shows at the left end of the sample. As the spatial position (x) increases the blue color starts to become lighter and disappears at the right end of the sample. The loss of blue light indicates the absence of diffraction at the right end of the sample.

The periodic nature of the surface can be identified by optical diffraction. Figure 1(B) displays a series of optical diffraction images collected along the central spatial x-positions of the sample. The diffraction images are acquired via an optical microscope with a Bertrend lens that focuses a Fourier spectrum of the sample image on the camera's image plane. The left end of the sample (x = 0 mm), indicated by the top diffraction panel in Figure 1B, has clear and strong diffracted spots (first order diffraction). As the spatial position increases (Figure 1A, x-axis), the transmitted intensity of diffracted spots in each corresponding panel becomes lighter (Figure 1B). For example, at x = 12 mm, diffracted spots have much weaker intensity compared to the spots shown in the top panel (x = 0 mm). A decrease in intensity of diffraction spots is due to smaller diffraction efficiency, an indication of a smaller amplitude value. Therefore, the series of diffraction images indicate qualitatively that the amplitudes of the grating gradually decrease from the left to the right of the sample. At x = 18 mm, almost no diffracted spots are observed and only the central diffuse spot from zero order transmission displays. This indicates that the surface is almost flat. Notably, both Figure 1A and 1B show decrease in diffraction along the x-position and therefore indicate the nature of the chirped amplitude grating.

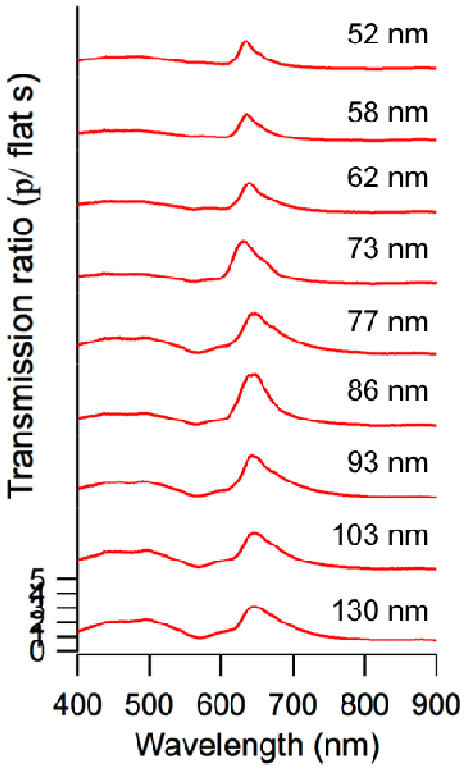

Figure 4 The spectra of transmission ratio through silver-coated (40 nm) chirped amplitude grating. The transmission ratio is obtained by dividing p-polarized spectrum through the grating by s-polarized spectra um through a silver-coated flat surface. Transmission spectra are collected at different amplitudes ranging from 52 nm to 130 nm. For each spectrum, 50 independent measurements are taken and averaged. All spectra are collected at incident angle = 0°.

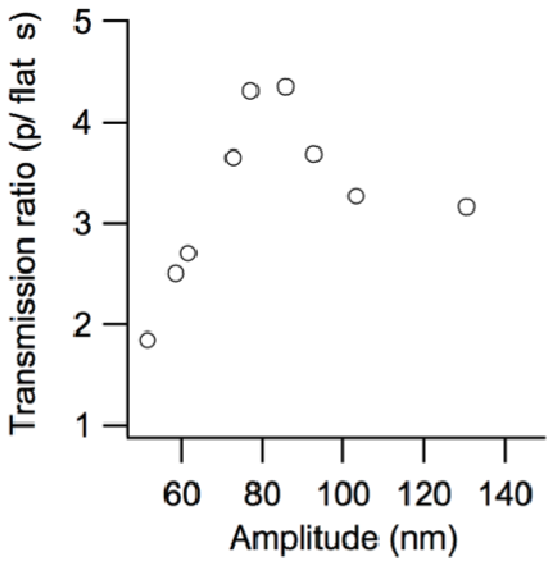

Figure 5 Maximum values of transmission peaks versus the amplitudes of the chirped amplitude grating. The transmission ratio is obtained by dividing p-polarized spectrum through the grating by s-polarized spectra um through a silver-coated flat surface.

A series of AFM measurements are conducted to examine the surface topology of the chirped amplitude grating. Figure 2A shows the sample's surface topology at x = 6 mm (x-axis, Figure 1A) and Figure 2B is the cross sectional profile of the image shown in Figure 2A. The cross sectional profile indicates the averaged amplitude and pitch at x = 6 mm are ~ 86 nm and ~ 624 nm, respectively. A summary of the AFM measurements at several x-positions is given in Figure 3. The amplitudes are analyzed and averaged based on the cross sectional profiles of AFM images. At x = 0 mm, the averaged amplitude has a maximum value = 130 nm. As the spatial position increases, the averaged amplitude gradually decreases. A smallest amplitude is observed = 35 nm at x = 20 mm before the surface becomes flat. In addition, the pitch of the grating is analyzed base on all profiles of images and has an averaged value ~ 624 nm.

To evaluate the degree of enhancement of transmission peaks, transmission ratio is used. The ratio is defined as a p-polarized transmission spectrum through a silver-coated grating dividing by a s-polarized spectrum through a silver-coated flat surface. Figure 4 shows a series of transmission spectra collected at several amplitudes on the chirped amplitude grating at incident angle = 0°. Each spectrum shown in Figure 4 represents an averaged spectrum obtained from 50 independent transmission measurements. At amplitude = 52 nm, a very small peak is observed has enhancement ~ 2.5. As the amplitude of the grating increases from 52 to 77 nm, the magnitude of enhancement gradually increases. The magnitude reaches maximum at amplitude = 86 nm and has a value ~ 4.35. The enhancement decreases as the amplitude further increases from 93 to 130 nm. Therefore, the amplitudes of gratings impact the magnitudes of enhanced transmission peaks. Figure 5 shows a summary of the enhancement versus the amplitude. It is clear that the magnitude of the enhanced transmission excited by SPR can be tuned and

maximized by the amplitude of the grating. In our case, the enhancement is largest at amplitude = 86 nm.

We used PCGrate® to simulate the optical responses of transmission peaks by changing amplitudes of the gratings. Figure 6 shows a series of transmission ratio spectra at different amplitudes. The ratio is a p-polarized transmission spectrum from a grating over s-polarized spectrum from a surface flat surface. The input pitch is 624 nm and the thickness of silver is 40 nm. The top spectrum in Figure 6 shows a small transmission peak at ~ 645 nm. As the amplitude increases from 52 nm to 86 nm, the enhancement increases and reaches maximum at 86 nm. As the amplitude increases further from 93 to 130 nm, the enhancement decreases and the peak becomes broader. The simulation results are summarized and plotted as transmission ratio versus amplitude (Figure 7). It is evident that transmission ratio reaches maximum = 12.5 at amplitude 86 nm. Notably, both simulation and experimental results show that the magnitude of enhancement can be tuned and maximized by the amplitudes of the grating. It should be noted that the enhancements from simulation are greater than those from experiments. Possible causes could be minor differences in the grating profile, silver thickness, structural defects on the gratings, or limitations in the experimental optics, such as the nonlinearity of the light source.

In Figure 8, diffraction efficiency of first order diffraction is plotted versus the amplitude of the grating. We used PCGrate® to simulate the optical responses of the grating at different amplitudes. The optical responses include intensity of diffracted, reflected, and transmitted light. Figure 8(A) shows calculated diffraction efficiency from first order diffraction. The diffraction efficiency used here is first order diffraction efficiency and is defined as the ratio of intensity from first diffraction over the intensity of incident light. The incident light is p-polarized (or transverse magnetic). Figure 8(B) shows relative diffraction efficiency versus the amplitude of

the grating. The relative diffraction is the intensity of blue light from first diffraction spots (details in supporting information). From Figure 8, the amplitudes clearly impact the diffraction efficiencies. Both the diffraction efficiency and relative diffraction efficiency increase as the amplitude increases and reach maximum as the amplitude reaches a critical value. For simulation, the maximum is ~ 0.25 at ~ 90 nm. The experimental results show the maximum is ~ 120 (a.u.) at ~ 90 nm. Both calculated and relative diffraction efficiency decrease as the amplitude increases beyond the critical value (~ 90 nm). Notably, simulation is consistent with experimental results.

To examine how the diffraction efficiency impacts the transmission enhancement, diffraction efficiency is plotted versus enhancement ratio, as shown in Figure 9. Y-axis in Figure 9(A) is calculated enhancement ratio (Figure 6) and enhancement ratio in Figure 9(B) is from experimental results (Figure 4). High diffraction efficiency has large transmission enhancement while low efficiency reflects small transmission enhancement. Evidently, diffraction efficiency tracks with transmission enhancement. Thus, surface plasmon resonance-enhanced optical transmission is strongly influenced by the performance (or diffraction efficiency) of the gratings. For grating-based SPR couplers, diffraction is needed in order to excite SPs which result in enhanced transmission. As the surface of the grating is almost flat (or has small amplitudes), SPs almost cannot be supported due to little diffraction and, thus, the magnitude of enhanced transmission peak is small. As the diffraction efficiency increases more intensity of light is diffracted. Increased intensity from diffraction contributes more to the intensity of enhanced transmission peak and thus the enhancement is higher.

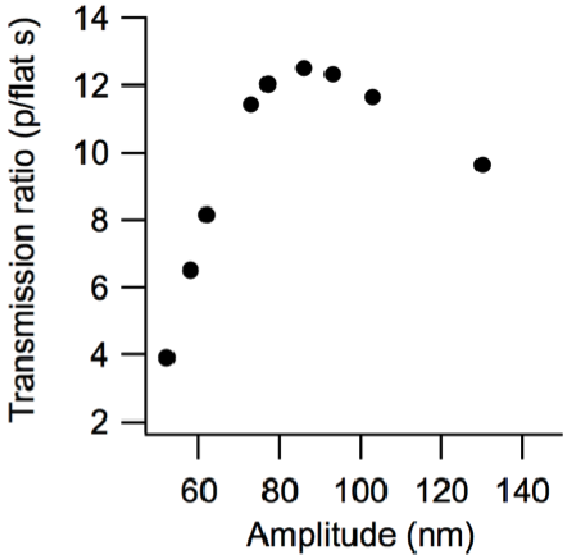

Figure 6 Transmission spectra of p-polarized over s-polarized light acquired by simulation. The thickness of silver is set at 40 nm and incident angle is 0°. Transmission spectra are calculated at different amplitudes ranging from 52 nm to 130 nm.

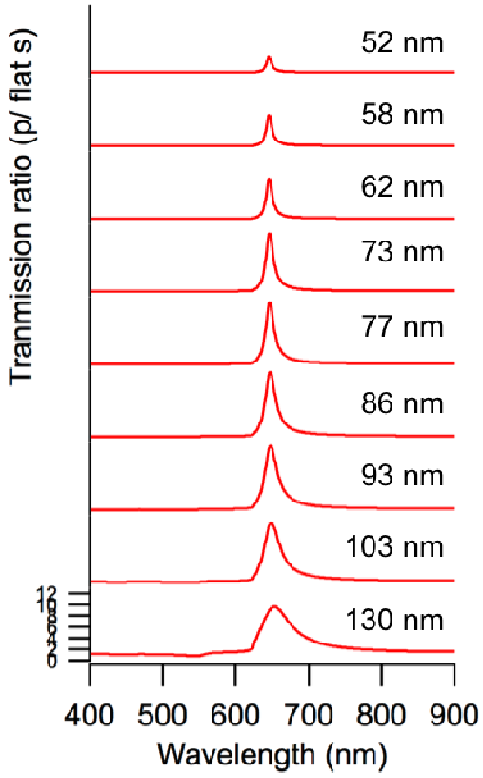

Figure 7 Maximum values of transmission peak versus the amplitudes of the grating. The transmission ratio is obtained by dividing p-polarized spectrum through the grating by s-polarized spectra through a silver-coated flat surface. The thickness of silver is 40 nm and incident angle = 0°.

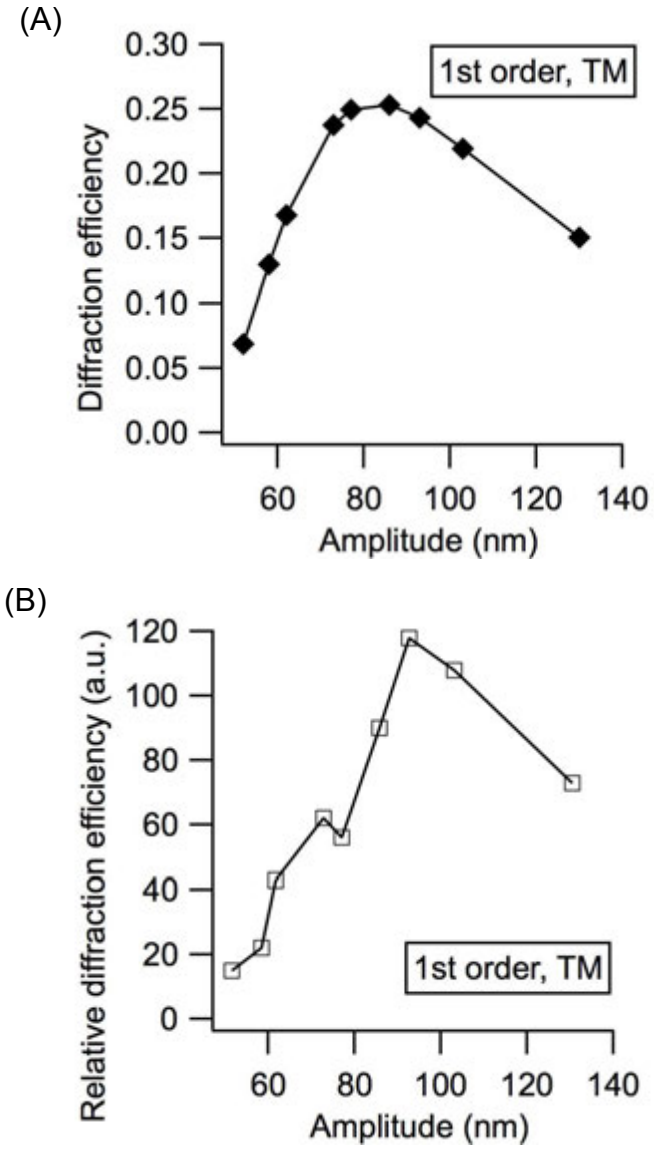

Figure 8 Diffraction efficiency versus amplitudes of gratings. (A) Calculated diffraction efficiency of first order versus the amplitudes of the grating. (B) Relative diffraction efficiency of first order versus the amplitudes of the grating. The incident light is transverse magnetic (TM), and incident angle is 0°.

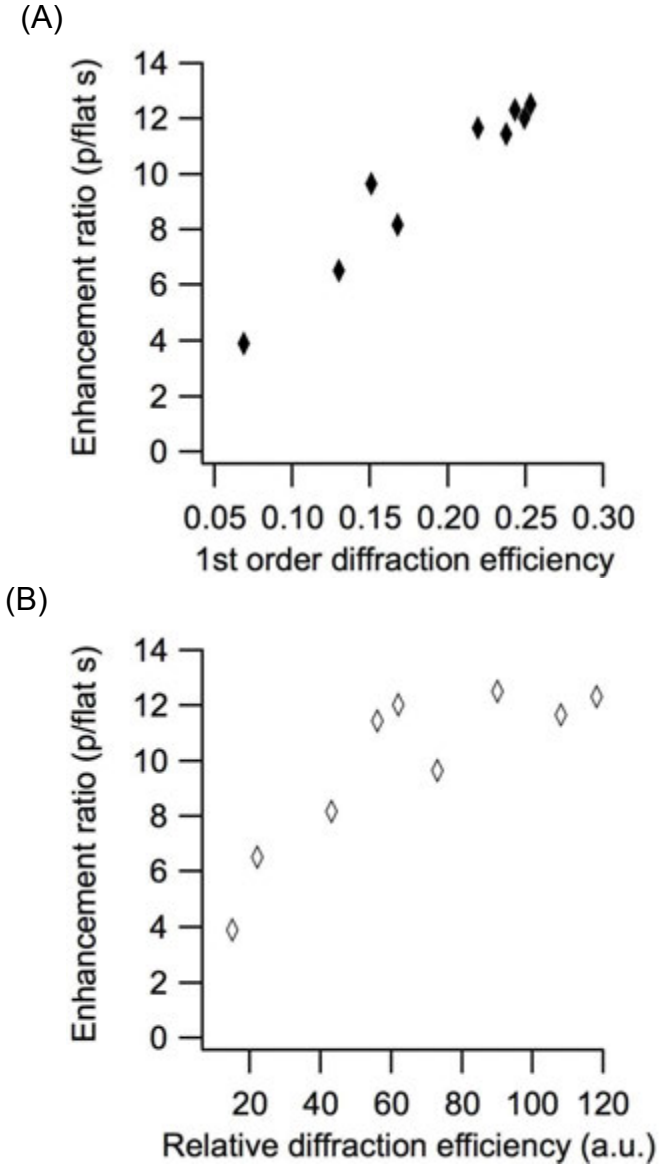

Figure 9 Enhancement ratio versus diffraction efficiency. (A) Calculated enhancement ratio versus the amplitudes of the grating (B) Experimental enhancement ratio versus the amplitudes of the grating. The values of the ratio represent maximum values in Figure 4 and Figure 6.

6.5 Conclusion

Periodic nanostructured substrates are a sensitive yet robust platform to excite surface plasmon resonance and the optical behaviors of surface plasmons can be tuned by changing the topology of the substrates. In this work, we demonstrate how the amplitudes of a chirped amplitude grating can tune the optical responses of enhanced transmissions. Several magnitudes of transmission peaks at a fixed wavelength, which are due to the changing amplitudes, are observed in a single sample. A transmission peak having maximum (or optimized) enhancement appears at a critical amplitude. Comparison of the predicted transmission peaks from simulation shows a consistency in the behaviors of the transmission peaks. Knowing critical amplitude of a grating allows ones to design diffraction-based sensors that have highest SRR signal enhancement and, therefore, the detection limit of these sensors can be further improved.

Supporting Information

Figure S1 illustrates a series of diffraction images (that are produced by illuminating p-polarized light) along the spatial position of the grating. The intensity of light source is set constant. The intensity of diffracted spots is acquired along the blue line and the sectional intensity profile versus the spatial positions of the grating is then plotted in Figure S2. Since the intensity output of same light source is set constant the degree of diffraction can be realized as how efficient the topology diffracts light. Thus, the intensity of diffracted light represents relative diffraction efficiency of the grating. Since we know the relation between the amplitudes and spatial positions (Figure 3), Figure 8B can be obtained.

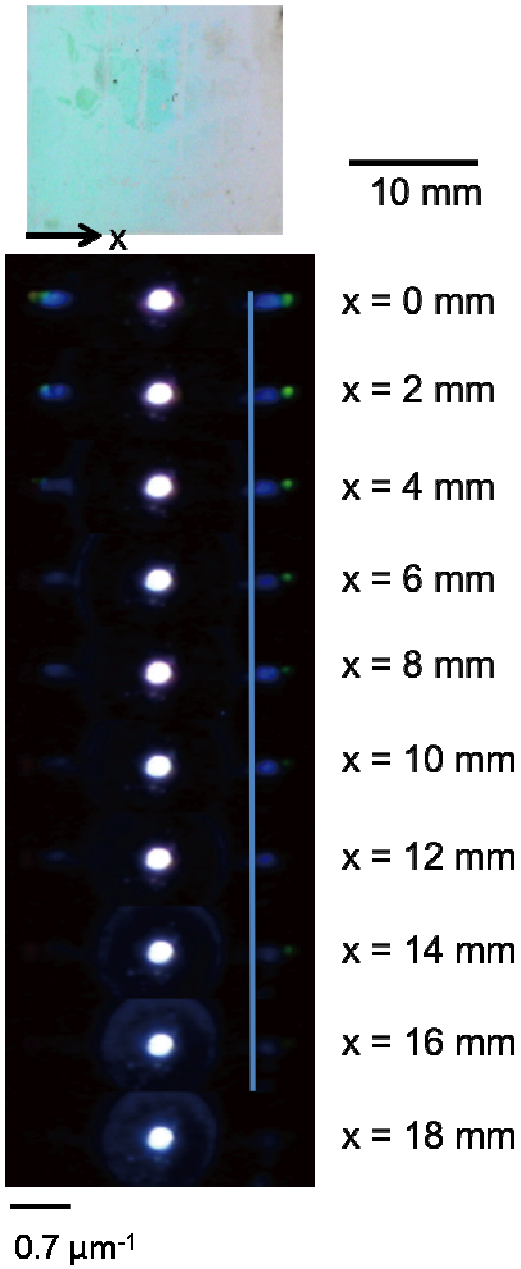

Figure S1 Optical diffraction images acquired at various *x*-positions along the center of the diffraction grating. An optical microscope with a Bertend lenses attachment is used to obtains the images.

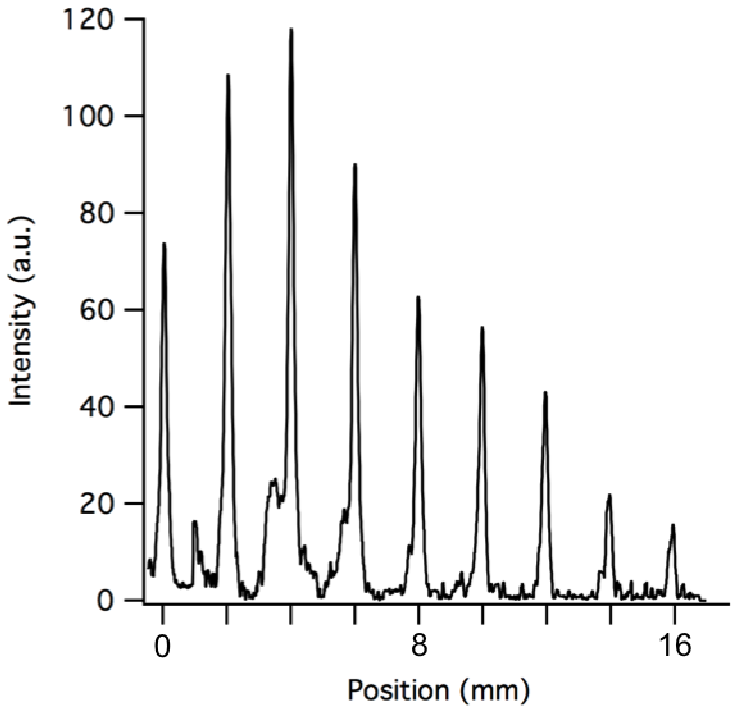

Figure 2S Cross sectional profile of first order diffraction intensity versus the spatial positions of the grating. The sectional intensity corresponds to the blue line shown in Figure S1.

6.6 Acknowledgement

This work was funded by the National Science Foundation (CHE 0809509 & 1213582).

6.7 References

1. Barnes, W.L., A. Dereux, and T.W. Ebbesen, *Surface plasmon subwavelength optics.* Nature, 2003. 424(6950): p. 824-830.

2. Ebbesen, T.W., et al., *Extraordinary optical transmission through sub-wavelength hole arrays.* Nature, 1998. 391(6668): p. 667-669.

3. Brolo, A.G., et al., *Surface Plasmon Sensor Based on the Enhanced Light Transmission through Arrays of Nanoholes in Gold Films.* Langmuir, 2004. 20(12): p. 4813-4815.

4. Jung, Y.S., Sun, Z., Wuenschell, J., Kim, H. K., Kaur, P., Wang, L., and Waldeck, D., App. Phys. Lett., 2006. 88.

5. Yeh, W.-H., J. Kleingartner, and A.C. Hillier, *Wavelength Tunable Surface Plasmon Resonance-Enhanced Optical Transmission Through a Chirped Diffraction Grating.* Analytical Chemistry, 2010. 82(12): p. 4988-4993.

6. Singh, B.K. and A.C. Hillier, *Surface plasmon resonance enhanced transmission of light through gold-coated diffraction gratings.* Analytical Chemistry, 2008. 80(10): p. 3803-3810.

7. Singh, B.K. and A.C. Hillier, *Surface plasmon resonance imaging of biomolecular interactions on a grating-based sensor array.* Analytical Chemistry, 2006. 78(6): p. 2009-2018.

8. Yeh, W.-H. and A.C. Hillier, *Use of Dispersion Imaging for Grating-Coupled Surface Plasmon Resonance Sensing of Multilayer Langmuir,ÄìBlodgett Films.* Analytical Chemistry, 2013. 85(8): p. 4080-4086.

9. Romanato, F., et al., *Interferential lithography of 1D thin metallic sinusoidal gratings: Accurate control of the profile for azimuthal angular dependent plasmonic effects and applications.* Microelectronic Engineering, 2009. 86(4,Äì6): p. 573-576.

10. Zacco, G., et al., *Sinusoidal plasmonic crystals for bio-detection sensors.* Microelectronic Engineering, 2011. 88(8): p. 1898-1901.

11. Lu, C. and R.H. Lipson, *Interference lithography: a powerful tool for fabricating periodic structures.* Laser & Photonics Reviews, 2010. 4(4): p. 568-580.

12. Xie, Q., et al., *Fabrication of nanostructures with laser interference lithography.* Journal of Alloys and Compounds, 2008. 449(1,Äì2): p. 261-264.

13. Chiang, H.K., et al., *Optical alignment and tilt-angle measurement technique based on Lloyd?s mirror arrangement.* Opt. Lett., 1992. 17(14): p. 1024-1025.

14. Palik, E.D., *Handbook of Optical Constants of Solids: Index*. Vol. 3. 1998: Access Online via Elsevier.

15. Kasarova, S.N., et al., *Analysis of the dispersion of optical plastic materials.* Optical Materials, 2007. 29(11): p. 1481-1490.

CHAPTER 7 CONCLUSIONS

This dissertation mainly focuses on surface plasmon resonance-enhanced optical transmission excited via diffraction grating couplers. First, the behavior of transmission, such as resonant wavelength and the magnitude of transmission, can be fine tuned by the topology (pitch or amplitude) of gratings. Second, a new spectroscopic technique is illustrated to monitor the thickness of thin films by utilizing grating couplers. Finally, complex optical responses from grating couplers are analyzed and indexed by utilizing dispersion images.

In Chapter 2, we built a chirped grating that has varying topology. An innovative yet simple method is illustrated to obtain the grating. Numerous transmission peaks are observed and are due to the varying topology of the grating and several diffraction orders. The advantage of the grating is that the grating is an information-rich SPR sensor. Multitude of wavelengths provides a data set which can be used to determine both the thickness and refractive index of the film. We anticipate that the sensor based on the chirped grating can be designed as array-type imaging system.

A new spectroscopic technique to monitor the thickness of thin films is presented in Chapter 3. A modified optical microscope with Bertrend lens attachment is used to image the optical responses of enhanced transmission peaks from first-order diffraction spots. The images recorded by a camera show capability to monitor the thickness of SiO_x films. The technique presented here also shows the ability to quantify the thickness of thin films down nanoscale.

Diffracting gratings are a platform for SPR and can be developed as a sensitive sensor. In chapter 3, we choose DVD gratings as SPR platform and, more importantly, we develop a new analytical technique to quantify and monitor the transmission from the first order of diffraction from gratings without a spectrophotometer. An optical microscope with a Bertrend lens that

focuses on the image plane of CCD camera is used. The camera readily acquires the information of the enhanced transmission peak from first order diffraction. We further demonstrate that the film thickness can be tracked by monitoring the change in the intensity profile captured by the camera. Thus, this technique and setup requires only a compact and portable microscope without using spectrophotometer.

In chapter 4, Kretschmann configuration is used to study the complex interaction between SPs and molecular resonance from a dye. A split of the dispersion curve is due to the quenching of SPs. Waveguide modes are observed as the thickness of ZnPC increases. Waveguide modes are also quenched in the absorption wavelength of ZnPC. The understanding of the interaction between SPR and MR allows the development of new optical sensor systems or optoelectronic devices.

In chapter 5, we use dispersion images consisting of a series of transmission spectra to interpret rich yet complicated SPR signals. All modes of SPR from both front side and back side can be indexed by the use of dispersion images. We further illustrate that only SPs from the front side are sensitive to change in refractive index after deposition of a thin dielectric film on the metal/air interface. The optical information from the back side of an asymmetric grating complicates the interpretation of SPR data. To overcome this problem, one can fabricate a symmetric grating. Symmetric gratings have identical interfaces in the front side and back side and, thus, the optical output of SPR is simpler compared to asymmetric gratings. Moreover, symmetric gratings provide interaction of SPs between front and back sides and long range SPR which has higher sensitivity compared to SPR can be achieved.

In Chapter 6, we fabricate a diffraction grating that has a constant pitch but varying amplitudes. We demonstrate how the amplitudes of a chirped amplitude grating can tune the

optical responses of enhanced transmissions. A transmission peak having maximum (or optimized) enhancement is observed at a critical amplitude. Increased enhancements are due to higher diffraction efficiency from first order diffraction. one can design a grating-based SPR sensor that higher signal-to-noise ratio by maximizing enhanced transmission peaks.

One of the suggesting future work is to fabricate a high performance diffraction-based SPR sensor. High signal-to-noise ratio and improved resolution can be achieved by optimized grating topology. The maximized magnitude of transmission can be achieved by tuning the amplitude of gratings and can improve the signal-to-noise ratio. Sharp transmission peaks which has higher resolutions can be obtained by tuning the profile of gratings. We anticipate that these types of nanostructured sensors will have increasing utility in sensing applications due to their sensitivity, flexibility, ability to be adapted into array-type imaging sysyems.